Young Researchers' Forum V - Innovation in Construction Materials

Klemm, Agnieszka J.; Rostami, Rohollah ; Almeida, Fernando C.R.

Publication date:
2021

Document Version
Publisher's PDF, also known as Version of record

2021

Young Researchers' Forum V

INNOVATION IN CONSTRUCTION MATERIALS

GLASGOW CALEDONIAN UNIVERSITY

22nd April 2021

Edited by Agnieszka J. Klemm, Rohollah Rostami & Fernando C.R. Almeida

Glasgow Caledonian University

School of Computing, Engineering and Built Environment

Sustainable Materials & Structures Research Group

Young Researchers' Forum V

22nd April 2021, online

The Institute of Materials, Minerals and Mining

The Institute of Concrete Technology

where science meets business

The Institution of Structural Engineers

ACCESS SOLUTIONS SCAFFOLDING

BASF We create chemistry

Glasgow Caledonian University

Preface

YRF V - Innovations in Construction Materials, is a research forum on for early-career scientists and engineers working in the field of construction materials, which was jointly organised by the Sustainable Materials and Structures Research Group of Glasgow Caledonian University and the Institute of Concrete Technology.

The forum builds on the success of the previous four events on this topic held by The Society of Chemical Industry (London 2012), University College London (London 2014), Imperial College (London 2016) and Northumbria University (Newcastle 2018). Due to the COVID-19 pandemic the YRF V, originally scheduled to be held in Glasgow in April 2020, had to be postponed and the 'face-to-face" presentations were replaced by the online presentations.

The Forum was opened by the Associate Dean Research Prof Ole Pahl and the Past President of the Institute of Concrete Technology Dr Raman Mangabhai.
The intention of organisers was to provide an opportunity for early-career researchers to showcase their work in the area of construction materials in an international context. The speakers from Brazil, Iraq, Iran, Switzerland and the UK contributed to the success of the event.
Innovations in Construction Materials is a very broad topic involving aspects starting from the material properties and behaviour, via structural performance to serviceability and durability. The themes covered this year included cement and concrete, aggregates, timber and steel.

Two prizes were awarded for the Best Presentations:

- The ICT prize to Dr Emmanuel Salifu (University of Strathclyde)
  for *"Recent Advances in Engineered Microbial Technologies for the Construction Industry"*
- The GCU/ IStruct prize to Ms Shima Jowhari Moghadam (Loughborough University)
  for "*Manufacturing free-form inflated thin-walled steel structural members"*

The organisers wish to thank all the authors for their hard work in preparing their contributions and meeting tight deadlines that have enabled the production of these Proceedings. We hope that the readers will find the papers topical and useful in their studies and work. In addition, it is anticipated that recent appointees in the construction materials industry would benefit from the opportunity to access state-of-the-art research knowledge in sustainable construction materials.

We would like to thank the Institution of Structural Engineers, Construction Materials Group of SCI, The Institute of Materials, Minerals and Mining, BASF and Access Solutions Ltd for supporting the event.

Finally, we would like to thank Mr Rohollah Rostami (GCU) and Dr Fernando C.R. Almeida (UFMG, Brazil) for their extensive assistance in organising this Forum.

Prof Agnieszka Klemm, FICT and the Chair of the YRF V
Dr Raman Mangabhai, Chairman of Events & Marketing and Past President of the ICT

April 2021

PROCEEDINGS CONTENTS

Young Researchers' Forum V

22nd April 2021, Glasgow Caledonian University

Programme

10:00 – 10:15		Welcome and introductory talks: Prof Agnieszka J. Klemm, Chair Prof Ole Pahl, Associate Dean - Research Dr Raman Mangabhai, Past President of ICT	
10:15 – 11:15		Session 1	
10:15	S.AL-Ameeri, A.	The effects of carbonation on the chloride resistance of concretes with supplementary cementitious materials (SCMs)	University of Brighton
10:25	Salifu, E.	Recent Advances in Engineered Microbial Technologies for the Construction Industry	University of Strathclyde
10:35	Tamilarasan, M.	Self-healing efficiency of steam cured Engineered Cementitious Composites at 28 days	Loughborough University
10:45	Briki, Y.	The limiting factors for metakaolin reaction in cement at late ages	LMC/EPFL - Hilderberg Cement
10:55 – 11:15		Discussion	
11:15 – 11:30		Coffee break	
11:30 – 12:30		Session 2	
11:30	Rostami, R.	Application of Superabsorbent Polymers in blended cement mortars reinforced by polymeric fibre	Glasgow Caledonian University
11:40	MacLennan, S.	The Effect of Alkali Activation on Absorption capacity of SAP in Ground Granulated Blast Furnace Slag (GGBS) and Copper Slag (CS) Solutions	Glasgow Caledonian University
11:50	Draper, S.	Optimising the embodied carbon efficiency of composite cements using thermodynamic modelling	Imperial College London
12:00	Campbell, A.	Exploration of a 3D Printed Geo-Polymer with Respect to Interlayer Bond Strength	Edinburgh Napier University
12:10 – 12:30		Discussion	
12:30 – 13:30		Lunch Break	
13:30 – 14:30		Session 3	
13:30	Orfeo, A.	Intelligent rubber bearings for bridge monitoring	University of Strathclyde
13:40	Moghadam, S. J.	Manufacturing free-form inflated thin-walled steel structural members	Loughborough University
13:50	Zhao, X.	Numerical simulations of disproportionate collapses of tall timber building under fire conditions	Glasgow Caledonian University
14:00	De Paula, B. J. G.	Pathological manifestations on concrete bridges in North-eastern Brazil	UFMG - Brazil
14:10 – 14:30		Discussion	
14:30 – 14:45		Coffee break	
14:45 – 15:45		Session 4	
14:45	Karimi, H.	Assessment of Surface Roughness of Ni and Ni-Si_3N_4 nanocomposite coatings fabricated by Pulse Electrodeposition	Shiraz University - Iran
14:55	Almeida, F. C.R.	Evaluation of chloride penetration in cementitious matrices with sugarcane bagasse ash sand	UFMG - Brazil
15:05	Alves, G.	Crushing Process Impact on the Characteristics of Fine Recycled Aggregates	UFMG - Brazil
15:15	Pesce, C.	Influence of Sucrose on the Morphology of Calcium Hydroxide Crystals	Northumbria University
15:25 – 15:45		Discussion	
15:45 – 16:00		Coffee break	
16:00 – 16:15		Prizes and acknowledgements	

Young Researchers' Forum V
Innovation in Construction Materials
22 April 2021

The effects of carbonation on the chloride resistance of concretes with supplementary cementitious materials (SCMs)

Abbas S.AL-Ameeri[1,2], Ali H. Nahhab[1] and Haider M.AL-Baghdadi[1]
[1] Department of Civil Engineering, University of Babylon- Iraq
[2] School of Environment and Technology, University of Brighton- UK

ABSTRACT

Concrete structures employed in de-icing and marine environment are commonly under the cyclic influence of carbon dioxide and chloride ion. Recently, the impact of chloride content on carbonation in concretes has been frequently considered; in comparison, the investigation of the influence of carbonation on the progress of chloride penetration is limited. This study is to investigate the potential influence of the carbonated concrete incorporating supplementary cementitious materials (SCMs) including GGBS and PFA on the chloride ingress in concretes. The experimental programme involves casting concrete cubes at three different water- cementitious ratios (w/cm) of 0.4, 0.5 and 0.6 with four crack widths of 0.1, 0.2, 0.3 and 0.4 mm. For concretes of 0.5% w/c ratio, the OPC was partially replaced by 30 % of GGBS and PFA. Concretes were exposed periodically to accelerated chloride- carbon dioxide (CO_2) - chloride environment. Chloride penetration and carbonation depth have been experimentally found for two types of concretes, uncracked and cracked concretes. The results have shown that the depth of carbonation (DoC) increased with the increase in the w/cm ratio and replacing OPC by GGBS and PFA. The penetration depth of chloride (d_{Cl}-) in concrete structures increased significantly owing to the influence of carbonation. The results also demonstrate a significant decrease in the penetration of chloride ions in carbonated concretes incorporating SCMs when compared to the reference concretes.

1. INTRODUCTION

The Durability of concrete structures is a common significant investigating issue, and it considerably impacts the service life of the concrete structures. Regarding all the concerns of the durability problems, chloride and carbonation diffusion are two factors that can be accelerated the corrosion of reinforcement. In some structures, such as those exposed to atmospheric zone in marine environment conditions (Castro et al., 2000) concretes suffer from both the chloride and carbonation ingress simultaneously or in series. The successional carbonation and chloride penetration process can also happen in concrete structures that built-in cold regions (Aveldano & Ortega, 2011), where de-icing rock salt is usually used in winter to melt ice and contains high concentration of chloride ions (Cl^-). Concerning the combined mechanisms of ingress of CO_3^{-2} and Cl^- ions in concrete, from one hand, it has been proved that carbonation affects the penetration of Cl^- noticeably. The process can be described as follows: at the first stage of carbonation, the formation of $CaCO_3$ leads to densify the concrete and slows down the penetration of Cl^- (Xu et al., 2011); on the other hand, the process of carbonation may reduce the chloride binding capacity of cement compounds that promotes the ingress of chloride in a certain degree (Wang et al.,2016). For the effect of replacement of supplementary cementitious materials (SCMs), the results of the depth of carbonation (DoC) for GGBS and PFA samples are higher DoC than DoC of mixes without these materials by using phenolphthalein indicator and XRD analysis. The results of DoC for the mixes incorporating SCMs (GGBS and PFA) have less $Ca(OH)_2$ than the OPC mixes at a different depth. Thus, relative intensities of $Ca(OH)_2$ remains low at a deep depth, while the concentration of $CaCO_3$ remains high at that depth (AL-Ameeri et al.,2018) On the other hand, the partial replacement of OPC with SCMs, GGBS, and PFA has a higher resistance to chloride penetration in concrete and the total concentration of chloride at a shallow depth remains high, and the reduction of concentration with depth at this zone was minor, while, the decrease of chloride content in the zone beyond the first one reduced sharply. To date, knowledge on the effect of Cl^- in concretes on the progress of carbonation is limited and the mechanism is still unclear. Therefore, the diffusivity of Cl^- and carbonation in concrete cover under the combined mechanism of exposure and the effect of carbonation penetration on the chloride resistance of concretes with (SCMs) needs to the .

2. Experimental work

2.1 Materials and Concrete Mix Design

Portland limestone cement (CEM II/A-LL 32,5R) with a specific gravity of 3.05 was used in this

study. Chemical and physical properties of the cement comply with BS EN 197- 1: 2011. Natural sand was used as fine aggregate (particle size < 5mm), and the coarse aggregate used was crushed gravel with the size ranging from 5-14 mm. The properties the aggregates comply with BS 882:1983. Three different w/cm ratios (0.4,0.5,0.6) were used to investigate their effects on the penetration of carbonation and chlorides. The Building Research Establishment method was used for concrete mix designs (see Table 1).

Table1 Concrete mixes designs used in this study

Mix symbol	Content per unit volume of concrete (kg / m^3)					
	w/c	Cement	GGBS or PFA	Water	Sand	Gravel
M 0.4	0.4	510	-	204	653	980
M 0.5	0.5	408	-	204	711	1023
M 0.6	0.6	340	-	204	711	1041
M 0.5+ GGBS	0.5	285	123	204	711	1023
M 0.5+ PFA	0.5	285	123	204	711	1023

2.2 Specimen Geometry

Three 100 mm cube specimens were used to establish the compressive strength of concrete and porosity measurements. Also, the concrete cubes samples were used to measure the depth of carbonation (DoC) and chloride penetration in both the cracked and un-cracked specimens. The artificial crack(notch tip) method was used to induce the cracks in concrete samples by using steel plates (see Figure 1). In addition to the control samples (no cracks), four different crack width, (0.1mm, 2mm, 0.3 mm and 4mm) were studied. The crack depth was fixed at 20 mm. Samples were cast in two layers and each layer was vibrated to achieve homogenous concrete. The specimens were demoulded and cured using tap water until the time of testing at the age of 28 days, or exposure to Cl^--CO_2 –Cl^- environment.

Figure 1. Method for cracking in the cubic sample

2.3 Specimens Conditioning

The main objective of this study was to investigate the effect of carbonation on the chloride penetration for different properties of concrete and crack width in concrete samples. In this study, one face of the specimens was exposed to accelerated environment conditions whereas the other faces were sealed using coats of water-based alkyl polysiloxane resin. The control samples were exposed to a chloride fog environment (with 5% NaCl) within a Cyclic Chloride Test (CCT) chamber for 17 weeks in total. The rest of the samples were taken out of the CCT chamber (see Figure 2) after 10 weeks of chloride exposure and they were exposed to CO_2 concentration of 5% within a CO_2 chamber (at a temperature of 25 ºC and relative humidity of 65%) for 5 weeks before returning them back in the CCT chamber (chloride exposure) for the remaining 7 weeks.

Figure 2. CCT Chamber for accelerating chloride penetration

2.4 Testing Methodologies

The compressive strength, porosity, depth of carbonation (DoC) and chloride penetration were carried out for this study. Porosity and compressive strength tests were conducted according to BS EN 12390-3:2000 respectively. The chloride penetration depth was measured by splitting the conditioned samples into two parts and spraying 0.1% silver nitride solution in accordance with (He et al.,2011). The silver nitrate solution reacts with chloride ions to form silver chloride, changing the colour of the concrete surface hence the depth of chloride penetration can be measured(He et al.,2011). In order to measure the depth of carbonation, CO_2 conditioned samples were split into two parts using a compression testing machine. The two parts were sprayed by a solution with one gram of phenolphthalein powder dissolved into a solution of 70 ml and 30 ml of ethanol and deionized water respectively complied with BS EN13295: 2004. The change of colour of the concrete surface was measured to find DoC.

3. Results and discussion

In this section, the results of the experimental work are presented and discussed. These are mainly focused on the impact of carbonation on d_{Cl}- for different w/cm ratio, SCMs and crack widths.

3.1 Carbonation Depth in Concrete

The depth of carbonation was established by measuring the depth of carbonation at different points along the sample width and computing the average of these measurements as shown in Figure 3. The DoC as a function of w/cm ratio for the mixes used in this study is shown in Table 2, where M 0.4, M 0.5 and M 0.6 refers to w/cm ratio of 0.4, 0.5 and 0.6 respectively. The results illustrated that the DoC increases slightly from the

exposed surface with the increase in w/cm ratio in concrete samples. On the other hand, the results showed that the DoC for un-cracked concretes with SCMs (M0.5+GGBS and M 0.5+PFA) were a higher than the DoC for control sample (M 0.5). While, the effect of crack on the DoC was limited because the duration of exposure to CO_2 environment was a few (5 weeks).

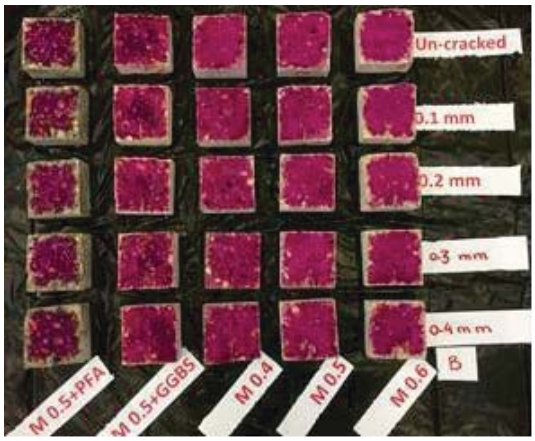

Figure 3. Carbonation depth of mixes used in the study (Series B)

Table 2 Carbonation depth of for mixes used in the study

Sample	Depth of carbonation (DoC) mm					Porosity %	Compressive strength (MPa)
	Un-cracked	Crack width 0.1 mm	Crack width 0.2 mm	Crack width 0.3 mm	Crack width 0.4 mm		
M 0.4	3	20	21	20	22	10	54
M 0.5	4	22	23	24	23	11	49
M 0.6	5	23	22	23	24	12	40
M 0.5+GGBS	5	23	22	23	24	10	48
M 0.5+ PFA	8	22	23	25	26	10	32

The increase of DoC in concrete mixes as a function of the w/cm ratio and type of cementitious materials is a result of two reason:first, the increase in porosity of concrete (see Table 2) and volume of permeable voids, i.e. the pore system of the hardened cement paste (Neville, 2011) and second, the decrease of quantity of $Ca(OH)_2$ due to the fact that there is a lesser quantity of Portland cement available to form $Ca(OH)_2$ in the blended cements as well as the pozzolanic reactions in blended cements converting calcium hydroxide to produce secondary C-S-H in the first days of hydration (Roy & Indorn, 1982), that helps CO_2 to penetrate and react with water to form $CO3^{2-}$, the latter then reacts with $Ca(OH)_2$ to form the $CaCO_3$.

3.2 Chloride penetration

Two sets of concrete samples were tested for chloride penetration; the first set (Series B) was exposed to a CO_2 environment in-between the exposure to the chloride fog environment, whilst the second set (Series A) was just exposed to the chloride fog (control specimen). The difference between the series is the first was exposed to an accelerated CO_2 environment, while the second was exposed to a normal CO_2 environment and exposure time to CO_2 for both was 5 weeks. The silver nitrate colorimetric method was used to measure the d_{cl}-. The $AgNO_3$ solution spray reacts with chloride ions to form a mixture of silver oxide and silver chloride that precipitates on the concrete surface and changes colour forming a boundary corresponding to the chloride penetration within the concrete specimen. Results for the two sets for different crack widths and w/cm ratio are presented in Figures 4 & 5 and Tables 3 & 4.

Table 3 Chloride penetration depth for samples used in (Series A)

Sample	Chloride Penetration depth (dcl^-) mm				
	Un-cracked	Crack width 0.1 mm	Crack width 0.2 mm	Crack width 0.3 mm	Crack width 0.4 mm
M 0.4	24	30	30	29	35
M 0.5	35	≥40	≥40	≥40	≥40
M 0.6	40	≥40	≥40	≥40	≥40
M 0.5+ GGBS	15	25	29	30	33
M 0.5+ PFA	14	23	22	25	27

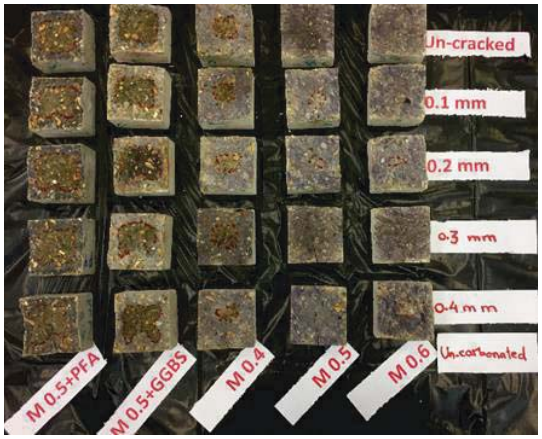

Figure 4. Penetration of chloride for uncarbonated sample with different crack width

Table 4 Chloride penetration depth for samples used in (Series B)

Sample	Chloride Penetration depth (dcl^-) mm				
	Un-cracked	Crack width 0.1 mm	Crack width 0.2 mm	Crack width 0.3 mm	Crack width 0.4 mm
M 0.4	27	33	31	34	39
M 0.5	40	≥40	≥40	≥40	≥40
M 0.6	≥40	≥40	≥40	≥40	≥40
M 0.5+ GGBS	15	29	31	31	31
M 0.5+ PFA	20	25	26	27	30

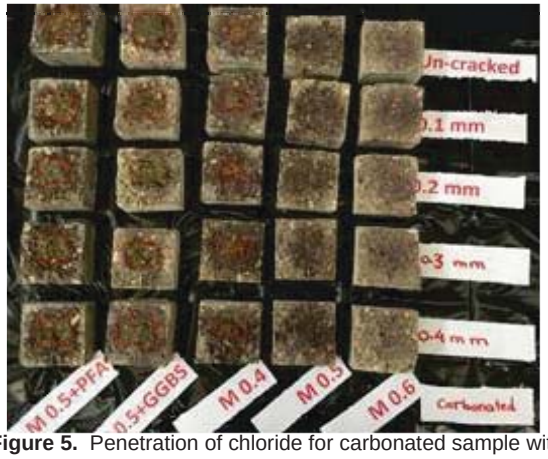

Figure 5. Penetration of chloride for carbonated sample with different crack width

Key observations from these results are:
(i) The results exhibit higher chloride penetration depths for samples exposed to CO_2 environment when compared with the control samples as shown in Figures 4 and 5 and Tables 3 and 4, particularly for the uncracked concrete samples. This can be attributed to the fact that the carbonation reduces the pH of the pore water in concrete which is a significant factor in liberation of bound chlorides (calcium chloroaluminate) in cement mortar (Wan et al., 2013) hence increases free chloride concentration and ultimately the penetration depth.
The results depict an increase in chloride penetration with the increase in w/cm ratio and decrease with using SCMs for both sets of concrete samples (i.e. with and without carbonation) particularly for the un-cracked samples.
(ii) This can be explained by the fact that the w/cm ratio affects the volume of internal voids or porosity in the concrete that in turn affects the chloride ions transport mechanisms in concrete, i.e. diffusion, permeation, sorption and permeability (Basheer et al.2001). The replacement of OPC by GGBS in concrete (M 0.5+GGBS and M 0.5+PFA) may refine pore networks and improve chloride binding capacities and subsequently decrease chloride transport through concrete compared to that of M 0.5 concretes (Thomas *et al*., 2012). Where, the pore structure of SCMs can be defined by, pore size distribution, pore specific surface area, total porosity as well as some characteristic pore sizes. The pore structure is the result of the observed hydration processes of cement and SCMs.
(iii) The chloride penetration depth increases with the crack widths for all mixes till a threshold crack width is reached, which is estimated from Figure 4and 5 to be around 0.1 mm. The crack width and depth affect the transport mechanism of chloride ion into the crack opening since wider cracks may allow the chloride solution to penetrate in the cracks. The cracks width less than 0.1 mm appear to have contributed only through an increase in the rate of transport of chloride ions (i.e. increase in permeability and diffusion rates of concrete). However, cracks of width greater than 0.1 mm appear to have provided additional surface area (along the crack walls) for the transport of chloride ions into the concrete. Hence, an increase in chloride penetration perpendicular to the crack walls can also be observed (Figure 4&5), which is similar to the chloride penetration profile from the surface of an uncracked concrete.

4. Conclusion

This study investigates the influence of carbonation on the chloride penetration and replacing OPC by GGBS and PFA in cracked concrete samples. The d_{cl}- and DoC were explored by using an accelerated environment test programme for (CO_2 and Cl^-). The DoC was found by phenolphthalein Indicator, whereas the d_{cl}- was measured by $AgNO_3$ spraying. The following conclusions can be drawn from the results;

1- The w/cm ratio, porosity, and compressive strength, quality and properties of concrete, affects the depth of carbonation and chloride penetration depths.
2- The chloride penetration increases significantly within the concrete samples exposed to CO_2 environment for all mixes used in the study.
3- There is a significant decrease in the penetration of chloride ions in uncarbonated and carbonated concretes incorporating SCMs when compared to the reference concretes.
4- For concrete specimens exposed to carbonation and chlorides, crack widths affect the penetration of chloride and therefore should be taken into consideration in service life prediction models.

References

AL-Ameeri, A., Rafiq, M., Tsioulou, O., 2018. Influence of cracks on the carbonation resistance of concrete structures', Sixth International Conference on the Durability of Concrete Structures, Leeds, July 2018(University of Leeds) 358-367.

Aveldano, R. R., & Ortega, N. F. ,2011. Characterization of concrete cracking due to corrosion of reinforcement in different environments. Construction and Building Materials, 25(2), 630–637.

Castro, P., Moreno, E. I., & Genesca, J. ,2000. Influence of marine micro-climates on carbonation of reinforced concrete building. Cem. and Con. Res.J, 30(10), 1565–1571.

He, F., Shi, C., Yuan, Q., An, X. and Tong, B., 2011. Calculation of chloride concentration at color change boundary of $AgNO_3$ colorimetric measurement. Cem. and Con. Res. J 41 :1095–1103.

Neville, A.M. Properties of concrete. (Five and Truly Final Edition) London:(2011) Pearson Education Limited.

Roy, D.M. , And Indorn , G.M. , 1982. Hydration, Structure and Properties of Blast Furnace Slag Cement , Mortar and Concrete, ACI Journal , Nov.- Dec. : 444-457.

Thomas, M., R. Hooton, A. Scott and H. Zibara ,2012. The effect of supplementary cementitious materials on chloride binding in hardened cement paste. Cem.and Con. Res.J 42(1): 1-7.

Wan, X., Wittmann, F., Zhao, T. and Fan, H., 2013. Chloride content and pH value in the pore solution of concrete under carbonation. Journal of Zhejiang University-Science A (Appl. Phy. & Eng.), 14(1), :71-78.

Wang, Y., P. Basheer, S. Nanukuttan and Y. Bai ,2016. "Progress of carbonation in chloride contaminated concretes."

Xu, C., Wang, C. K., & Jin, W. L., 2011. Interaction effect of chloride attack and carbonation in concrete. Journal of Building Materials, 14(3), 376–380.

Young Researchers' Forum V
Innovation in Construction Materials
22 April 2021

Recent Advances in Engineered Microbial Technologies for the Construction Industry

E. Salifu[1], F. Gutteridge[2], K. Witte[3]
[1]Department of Civil and Environmental Engineering, University of Strathclyde, Glasgow, UK
[2]Department of Design, Manufacturing and Engineering Management, University of Strathclyde, Glasgow UK
[3]Strathclyde Institute of Pharmacy and Biomedical Sciences, University of Strathclyde, Glasgow, UK

ABSTRACT

Microbial biotechnologies have received attention in the construction industry in recent times. This is partly driven by the climate change motivated transition towards the adoption of low carbon and environmentally friendly cementitious technologies in varied sectors of the construction industry. The multidisciplinary approach by researchers in the emerging area of Construction Biotechnology has led to the development of innovative low costs and low carbon microbial-based products like bio-bricks, bio concrete or self-healing concrete/bricks mediated by bacteria, fungi, and biofilms. Similar advancements are recorded in the development of microbial biocements and biogrouts, as well as the recent concepts of engineered growth of microbial living systems (e.g., using bacteria, fungal mycelia, microbial communities such as biofilms, lichens) towards applications in ground improvement, as living building materials, or as resource for production of construction materials. This paper presents a brief scoping review of the research advancements in the development of microbial-based materials/products/processes for applications in the construction industry. A description of recent breakthroughs in engineered microbial technologies which may be imminently deployed in practice are also presented. Besides providing a snapshot of the state-of-art, this paper also reveals unique insights and concepts that expose existing research gaps and propose areas of future research directions in engineered microbial biotechnologies for the construction industry.

1. INTRODUCTION

The construction industry has come under pressures to adopt innovative processes and materials to meet societal challenges and demands (Latham, 1994), and more importantly, for environmental sustainability. Traditional processes and methods of production of construction materials are energy-intensive and often associated with adverse environmental impacts. Research has shown that the adoption of novel bioprocesses and biomaterials could result in less environmental pollution and ~10% reduction in energy demand compared to conventional approaches (Ivanov and Stabnikov, 2017). With exponential growth and development in industrial biotechnologies (e.g., medicine and pharmaceuticals, food and agriculture, environmental sectors) it has been predicted that by 2030, one-third of materials will be derived from biological sources (Padinjakkara, 2018). To maintain its competitiveness, the construction industry has been challenged to transition towards the adoption of low carbon and environmentally friendly technologies derived from biological sources. Construction microbial biotechnology, a new subdiscipline concerned with the use of microbial systems, microorganisms, or their derivatives to develop new materials and processes or modify existing ones for use in the construction industry, has been evolving over the last decade (Ivanov, Chu and Stabnikov, 2015; Stabnikov, Ivanov and Chu, 2015). Conventionally, microorganisms such as bacteria, fungi, and algae are considered hazardous to structures and building materials, known to cause staining or discolouration, corrosion, disaggregation, weakening and dissolution of structural materials (Gaylarde *et al*., 2003; Bertron, 2015). But microorganisms are ubiquitous in natural environments and highly 'pervasive' inbuilt infrastructure. Researchers in construction microbial biotechnology have been exploring techniques for taking advantage of these abundant natural biological systems to provide beneficial effects for structural elements, components, materials, and processes in the construction industry. Table 1 presents a summary of developments in research activities and innovations involving microbial-based products and processes for application in the construction industry.

More recently, there has been a growing body of research in the aspect of engineered growth/ modification of microorganisms for targeted applications in the construction industry. This is focused on the potential deployment of microorganisms, *insitu,* as living functional systems

to enhance restoration, strengthening, and beautification of structural components or construction materials. Additionally, this comes with the potential of lowering carbon emissions and construction maintenance costs as well as enhancing the properties and functions of construction materials. This paper provides an overview of research developments in the aspects of engineered bacteria, fungi, and microbial communities (biofilms, lichens) in soil or ground improvement and in the production and optimisation of building/structural materials. A brief scoping review, that is, a descriptive style systematic literature review (SLR), showing advances in research publications in engineered microbial technologies for the construction industry is provided, followed by a description of findings from the latest relevant studies on each aspect of this technology, and a discussion of research gaps and future directions of this novel subdiscipline.

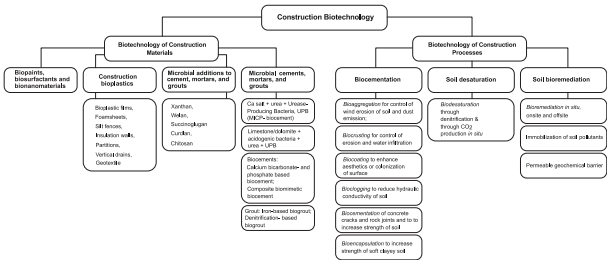

Figure 1. Research & developments in construction biotechnology (Based on Ivanov, Chu and Stabnikov, 2015; Stabnikov, Ivanov and Chu, 2015)

2. Overview of Construction Microbial Biotechnologies and Engineered Microbial Technologies for the Construction Industry

A scoping review was performed to ascertain the status of research advancements in engineered microbial technologies within the subdiscipline of construction biotechnology. Keywords used in the literature search include the terms in Table 1 as well as multiple variations of construction biotechnology, microbes, soil, and concrete, among others. The review was conducted following the procedures described by Arksey & O'Malley (2005) for identification of relevant studies, study selection, data collation, summarising and reporting. Publications were obtained from a search in the Scopus database. (Details of the search strings and dataset are available at the link provided in the data statement at the end of this paper).

As shown in Fig. 1, the total number of research publications, n, in the Construction Microbial Biotechnology applied to ground improvement or construction materials/processes within the period 1990 – 2019 was 123. The research outputs obtained, including those in engineered bacteria (n = 86) and engineered fungi (n = 6) were published as journal articles, review papers, book chapters and in conference proceedings (Fig. 1, *inset*). No record was found for research in engineered lichens. Other studies did not fit into the criteria for any of the three broad classes of engineered microbial technologies within the scope of this paper.

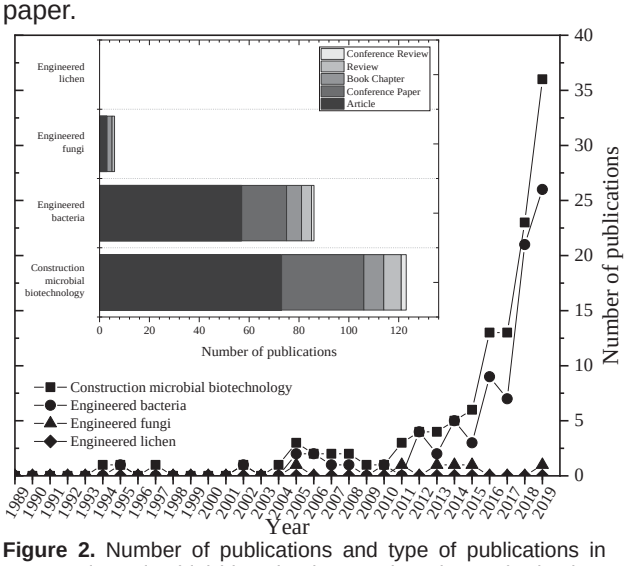

Figure 2. Number of publications and type of publications in construction microbial biotechnology and engineered microbes (bacteria, fungi, lichens) from 1989-2019.

Table 1. Journals with >6 publications in construction microbial biotechnology based on the total eligible documents used in the scoping review

Journals (number of publications)
Construction and Building Materials (21)
Journal of Materials in Civil Engineering (9)
Advanced Materials Research (8)
Ecological Engineering (8)
Water Resources Research (8)
Scientific Reports (7)

Research activities in this area started gradually about two decades ago and have increased exponentially since 2010 to date. This increase may be due to the developments in a rapidly emerging area of geotechnical engineering called biogeotechnics, which embraced research into the application of microbial induced calcite precipitation (MICP), a biomineralisation technique for ground improvement (DeJong *et al.*, 2010). Active researchers are drawn from multidisciplinary subject areas encompassing civil engineering, material sciences, and environmental sciences, as reflected in the journal titles in Table 2.

As shown in Table 1, microbial mediated technologies for the construction industry are in the broad areas of (i) soil modification via biomineralization involving biocementation or bioclogging of soil resulting in soil particle aggregation, biocrusting, surface biocoating, biodesaturation, bioencapsulation and bioremediation (Ivanov and Stabnikov, 2017); and (ii) production or modification of construction materials such as the manufacture of durable bio cement or mortar bio bricks or bio concrete - concrete self-repair via bacteria-mediated sealing of aperture cracks (Jonkers & Schlangen, 2008).

The typical approach involves the preparation of microbial culture of a suitable strain and inoculation of sand/soil, organic material, aperture cracks, or concrete mix (encapsulated inoculant), along with or without some nutrients and chemicals, depending on the desired outcome. Often, the microbial cells might lose viability during or after the process, leaving behind microbial biomass as part of the end products. In other processes of engineered microbial technologies, the microbe is engineered to remain viable and retain its activity, converting the material media or construction component into a functional living biosystem. Three forms of this latter process of construction microbial biotechnology are described in the following subsections.

Engineered Bacteria for Ground Improvement and Concrete Repair

Dade-Robertson *et al.* (2018) reported the development of a novel pressure-responsive biocementation system using engineered bacteria as biosensors whereby the bacteria initiate synthesis of cementitious materials upon detection of mechanical changes. By integrating synthetic biology, computational modelling, and gene expression data from in vivo experiments, with geotechnical engineering modification of soil consolidation behaviour, the authors demonstrated that this technique could be applied to the construction of building foundations by engineering pressure-sensitive soil bacteria to grow within soil matrix and automatically cement the soil in response to pressure changes. This is similar to the use of engineered bacteria to create bio concrete or self-healing concrete presented in Jonkers & Schlangen (2008). Encapsulated bacteria spores together with nutrients are added to concrete during mixing, such that when cracks later occur and water is transmitted into the aperture, bacterial activity resumes and biomineralization takes place, forming calcium carbonate which fills, seals and heals the cracks *in situ*. The bacteria may become inactive as moisture depletes but can be reactivated if conditions become favourable or if amended with additional bacteria and nutrient solutions injected into the system. To overcome this limitation, Heveran *et al.* (2020) developed an engineered living building material (LBM) by inoculating a photosynthetic cyanobacterium (*Synechococcus sp.)* into a structural scaffold composed of sand and gelatin (hydrogel). Gelatin scaffolds reportedly improve in strength when dehydration occurs; thus, environmental switches in temperature and humidity have a minimal adverse effect on the LBM, instead, the changes tend to regulate metabolic activity of the bacteria and promote successive regenerations of viable LBMs conferring biological-structural multifunctionality on the construction material.

Engineered Fungal Growth for Ground Improvement

It has been demonstrated that suitable fungal species are also capable of biomineralization via MICP to achieve similar outcomes as with bacteria-mediated calcite precipitation (*e.g.,* Martuscelli *et al.*, 2020). However, researchers have recently started exploring the potential for the utilisation of fungal mycelia networks for ground improvement via engineered fungal growth. Salifu (2019) presented a systematic experimental campaign investigating the influence of the engineered growth of the mycelia networks of *Pleurotus ostreatus* (oyster mushroom) on the hydromechanical behaviour of sands. Engineered fungal growth resulted in significant modification of the hydraulic behaviour of sand, inducing extreme water repellency, decrease in infiltration and field-saturated hydraulic conductivity, increase in the uniaxial compressive strength of sand (Lim *et al.,* 2020), and reduction in erodibility of sand.

Engineered Microbial Communities for Soil Bioclogging and Biocoating of Surfaces

Engineered bacteria biofilms in soil.
Naturally occurring microbial communities like biofilms such as biological soil crusts (comprising of bacteria, fungi, and algae), can exert strong influences on colonised surfaces. Biofilms are formed when microbial cells adhere to solid surfaces, replicate, and bind themselves firmly to the surface using the extracellular polymeric substance (EPS) which they excrete, thereby resulting in a complex 3-dimensional structure. In soils, engineered biofilms result in a reduction in permeability via bioclogging. Lin *et al*., (2018) engineered biofilm formation for *Staphylococcus epidermidis* in a soil matrix, to investigate the effect of the biofilm and EPS on soil mechanical behaviour. They found that biofilm-treated soil had less strength compared to untreated controls.

Engineered lichens for the protection of concrete facades.
Published research works in the utilisation of engineered lichens in construction biotechnology are scarce. In the last year, researchers at the University of Strathclyde began an explorative study of the potential of creating universally adaptable bio-interfaces for enhancing engineered growth of lichens as living, waterproof, carbon-efficient, metal capturing, bio-coating for deployment to already existing structural facades.

3. Prospects, Challenges and Potentials of Engineered Microbial Technologies in the Construction Industry

Figure 3 summarises the prospects and potentials of engineered microbial technologies in the

construction industry. It is envisaged that more research will develop in the areas of engineered fungi and engineered microbial communities (such as biofilms and lichens) to build on the pioneering studies which began very recently. A key challenge of this technology is in the ability to control the growth of the engineered microbes, to avoid debilitating/deleterious effects on adjacent materials or structural components. Poor understanding and slow acceptance of genetic engineering may also slow down research progress in construction microbial biotechnologies. A useful long-term strategy for creating self-sustainable systems may be through the modification of environmental factors around structural components to enhance colonisation by desired microbial species could be.

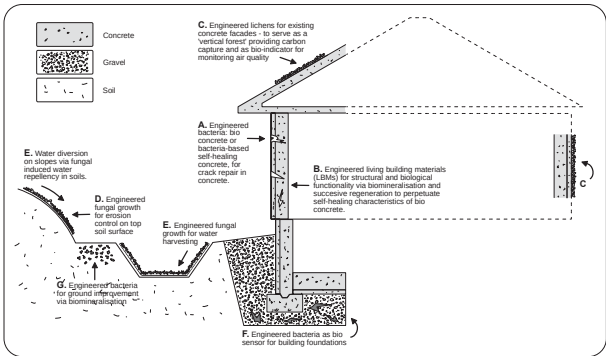

Figure 3. Prospects and potential areas of application of engineered microbial technologies in the construction industry.

4. CONCLUSION

This paper presented an overview of research advancements in engineered microbial biotechnologies within the emerging subdiscipline of construction biotechnology. A scoping review showed an exponential increase in research within this area from 2010 to date. Future research exploits are expected in the areas of engineered fungi and microbial communities (biofilms, lichens) to develop more sustainable, durable, and cost-effective applications for relevant components of the construction industry.

All data underpinning this publication are openly available from the University of Strathclyde KnowledgeBase at https://doi.org/10.15129/62be4b55-1fc4-42a1-84e7-c893a1197449

The authors wish to acknowledge the support of the University of Strathclyde's internally funded project: 20/21 Strathwide-Project 6.

References

Arksey, H. and O'Malley, L. (2005) 'Scoping studies: towards a methodological framework', *International Journal of Social Research Methodology*. Routledge, 8(1), pp. 19–32. doi: 10.1080/1364557032000119616.

Bertron, A. (2015) 'Erratum to: Understanding interactions between cementitious materials and microorganisms: a key to sustainable and safe concrete structures in various contexts (Materials and Structures (2014) 47, (1787-1806), 10.1617/s11527-014-0433-1)', *Materials and Structures/Materiaux et Constructions*, 48(1–2), p. 513. doi: 10.1617/s11527-014-0462-9.

Dade-Robertson, M. *et al.* (2018) 'Design and modelling of an engineered bacteria-based, pressure-sensitive soil', *Bioinspiration and Biomimetics*, 13(4). doi: 10.1088/1748-3190/aabe15.

DeJong, J. T. *et al.* (2010) 'Bio-mediated soil improvement', *Ecological Engineering*, 36(2), pp. 197–210. doi: 10.1016/j.ecoleng.2008.12.029.

Gaylarde, C., Ribas Silva, M. and Warscheid, T. (2003) 'Microbial impact on building materials: An overview', *Materials and Structures/Materiaux et Constructions*, 36(259), pp. 342–352. doi: 10.1617/13867.

Heveran, C. M. *et al.* (2020) 'Biomineralization and Successive Regeneration of Engineered Living Building Materials', *Matter*. Elsevier Inc., 2(2), pp. 481–494. doi: 10.1016/j.matt.2019.11.016.

Ivanov, V., Chu, J. and Stabnikov, V. (2015) 'Basics of construction microbial biotechnology', in *Biotechnologies and Biomimetics for Civil Engineering*, pp. 21–56. doi: 10.1007/978-3-319-09287-4_2.

Ivanov, V. and Stabnikov, V. (2017) *Construction Biotechnology: Biogeochemistry, Microbiology and Biotechnology of Construction Materials and Processes*. doi: 10.1201/b19683-28.

Jonkers, H. M. and Schlangen, E. (2008) 'Development of a bacteria-based self healing concrete', in *Proceedings of the International FIB Symposium 2008 - Tailor Made Concrete Structures: New Solutions for our Society*, p. 109. doi: 10.1201/9781439828410.ch72.

Lim, A., Atmaja, P. C. and Rustiani, S. (2020) 'Bio-mediated soil improvement of loose sand with fungus', *Journal of Rock Mechanics and Geotechnical Engineering*, pp. 180–187. doi: 10.1016/j.jrmge.2019.09.004.

Lin, H., Suleiman, M. T. and Brown, D. G. (2018) 'Behavior of Biofilm-Treated Sand', (September), pp. 1–11. doi: 10.1061/9780784481592.001.

Martuscelli, C. *et al.* (2020) 'Potential of Fungi for Concrete Repair', *Procedia Manufacturing*, 46, pp. 180–185. doi: https://doi.org/10.1016/j.promfg.2020.03.027.

Padinjakkara, A. (2018) *Biopolymers and Biomaterials*, *Biopolymers and Biomaterials*. doi: 10.1201/9781315161983.

Salifu, E. (2019) *Engineering Fungal-Mycelia for Soil Improvement*. PhD Thesis, University of Strathclyde, Glasgow, United Kingdom.

Stabnikov, V., Ivanov, V. and Chu, J. (2015) 'Construction Biotechnology: a new area of biotechnological research and applications', *World Journal of Microbiology and Biotechnology*, 31(9), pp. 1303–1314. doi: 10.1007/s11274-015-1881-7.

Young Researchers' Forum V
Innovation in Construction Materials
22 April 2021

Self-healing efficiency of steam cured Engineered Cementitious Composites at 28 days

Meenakshi Tamilarasan, Ana Blanco, Chris Goodier, Sergio Cavalaro,
School of Architecture, Building and Civil Engineering, Loughborough University

ABSTRACT

Self-healing Engineered Cementitious Composites (ECC) have the potential to offer an improved solution for concrete repair with enhanced durability. The literature on self-healing ECC commonly reports results using traditional curing methods. However, for certain applications where early age strength is needed or production must be increased through rapid turnover of moulds (i.e., in the precast industry), steam curing is required. Nevertheless, the influence of steam curing in the self-healing process has not been investigated. Hence, this paper evaluates the self-healing of steam cured ECC samples with either crystalline admixture or magnesium oxide as self-healing agents. The recovery of flexural strength, water permeability, surface and internal cracks were examined on steam cured specimens. The dosages of the healing agent used significantly affected the strength and durability parameter. The rate of healing was monitored by the Ultra Pulse Velocity (UPV) test and water permeability test on pre-cracked samples. The results show higher self-healing in the first 14 days with a subsequent decrease in the rate of self-healing at the 28 days.

1. INTRODUCTION

Concrete structures suffer from ageing, damage, deterioration, and worsening of their performance during their remaining service period (Rana *et al.*, 2016). In the UK, the Institution of Civil Engineers recently highlighted the lack of high-performance infrastructure, the ageing of assets and the growing needs for maintenance (ICE, 2018). Currently, repair and maintenance costs correspond to almost 45 % of the UK spending in construction and building (around £9 billion/year) (Pattnaik, 2006; Martin, 2018). ECC is one of the efficient solutions for repairing the concrete structure due to high delamination resistance, energy absorption capacity, and tensile hardening behaviour in the hardened state (Li, 2008). Also, self-healing mixes represent an interesting solution for concrete repair in the long terms due to their enhanced durability, which in turn can lead to reduced maintenance costs.

Self-healing material is defined as the Cementitious composites that can heal themselves by sealing the cracks because of the reaction generated by the activation of the healing agents (e.g., chemical admixtures, bacterial deposition), fully or partially recovering of their initial properties (mechanical and durability) after certain healing periods. The self-healing performance of concrete or ECC with chemical admixtures subjected to different environmental exposure conditions (e.g. expose to the local climate or air in a climate room with a control relative humidity and temperature, submersion in water at a different temperature, wet/dry and freeze and thaw cycles) has been well researched (Sánchez *et al.*, 2018). However, the influence of the steam curing on the self-healing efficiency of ECC subjected to water submersion has not yet been investigated. Steam cured samples develop early strength and reduce the permeability in a shorter time as compared with conventional curing which is essential for pre-cast concrete samples. The present study investigates the self-healing performance of steam cured ECC mixes with either crystalline admixture (CA) or magnesium oxide (MgO).

2. EXPERIMENTAL PROGRAM

2.1 Materials specification

Ordinary Portland cement CEM I 52.5N, fly ash (FA), sand, Polyvinyl alcohol (PVA) fibres, high range water reducing agents or superplasticising concrete admixture (SP), commercially available crystalline admixture (Sika ® WT-200 P) in powder form and Magnesium Oxide in the powder were used.

2.2 Mix proportion

The quantity of PVA fibre was used 1.8% by volume based on the literature and trial experiments. Five different mixtures were designed using a w/c of 0.46. Fly ash, FA was used as filler material. The content of CA and MgO were defined according to the literature and trial experiments. Three different dosages were adopted for the CA (0.5, 1 and 2% by the weight of cement), whereas a single optimum dosage of MgO (5% by the weight of cement). The proposed ECC mixes for the study are presented in Table 1.

Table 1. ECC mix design (Kg/m^3)

Mix Design	Cement	Water	Sand	FA	SP	Fibre	CA	MgO
CA2	800	368	640	240	8	23.4	16	-
CA1	800	368	640	240	8	23.4	8	-
CA0.5	800	368	640	240	8	23.4	4	-
MgO5	800	368	640	240	8	23.4	-	40
C	800	368	640	240	8	23.4	-	-

Notations; CA2, CA1 and CA0.5: Mix with 2%, 1% and 0.5 of crystalline admixture by the weight of cement respectively, MgO5: mix with 5% of magnesium Oxide and C: control mix.

2.3 Tests and specimens

In the present study 4-point bending test, Non-destructive test (UPV) and water permeability were performed to assess self-healing. An overview of the specimen configuration for each test is summarised in Table 2.

Table 2. Specimen configuration

Test methods	British standards	Standard/practice size (mm)	Sample size used in the study (mm)
Slump Cone	BS EN 12350-2:2009	base diameter: (200±2) mm; top diameter (100 ± 2) mm; height: (300 ± 2) mm.	-
Compressive strength test	BS EN 12390-3:2009	100, 150, 200, 250, 300 mm	100x100 x100
4-point bending test	-	100x100x500mm	30x100x500
Water permeability	-	ø100x200 and ø150x302	ø100x200

2.4 Pre-cracking, curing method, and healing period of the specimens

Four-point bending test was performed to induce controlled cracks in the beams and to identify the recovery of flexural strength after the healing period. A splitting tensile test was used to pre-crack in the cylinders for the water permeability test. All the specimens were pre-cracked at 28 days with an average crack width range of 0.10 to 0.30 mm (based on the previous studies the reasonable healing could be achieved with an average crack width range of 0.1 to 0.4 mm for mix with either CA or MgO (Sisomphon *et al.*, 2012; Roig-Flores *et al.*, 2015, 2016; Qureshi *et al.*, 2018))

All specimens were steam cured and submerged in the water bath for 28 days after being pre-cracked.

3. RESULTS AND DISCUSSIONS

3.1 Slump values

The mixes confirm slumps of between 190 and 210 mm. The slumps height and average slump diameter of different mixes as seen in Table 3. The concrete slump should be maintained between 80 and 200 mm to produce better fresh and hardened concrete qualities (EFNARC, 1999).

Table 3. Slump height and average slump diameter

Mix	Slump height (mm)	Average slump diameter (mm)
CA2_S	200	337.5
CA1_S	200	355
CA0.5_S	205	320
MgO5_S	190	345
CA2_W	205	302.5
C_S	210	335

Notations; S: steam curing and W: water curing

3.2 Compressive strength

The mean compressive strength of the mixes is shown in Table 4 and Figure 1 and are in line with the literature (Li, 2008). The results indicate that the incorporation of CA influences the compressive strength of ECC mixes. CA2_W shows 18% higher strength than the control mix.

MgO5_S shows no significant effect in compressive strength at 28 days. Similar results found with a 5% addition of MgO in the cement paste (Qureshi *et al.*, 2018).

Table 4. Compressive strength at 28 days

Specimen	CA2_W	CA2_S	CA1_S	CA0.5_S	MgO5_S	C_S
Mean (MPa)	74.34	56.66	63.14	67.10	64.04	62.92
CV (%)	1.59	0.58	5.25	1.11	2.44	2.07

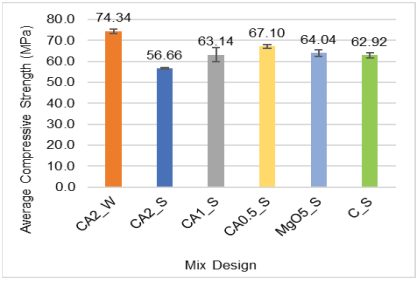

Figure 1. Average compressive strength at 28 days.

3.3 Crack healing

3.3.1 Internal crack healing

The internal crack healing and the healing rate were evaluated by the UPV test. Working on the hypothesis that discontinuities, such as cracks would reduce the velocity due to longer travelling time, the magnitude of crack healing can be directly evaluated through comparison of the change in time. The mean UPV values of different mixes before and after healing at 14 and 28 days are shown in Figure 2.

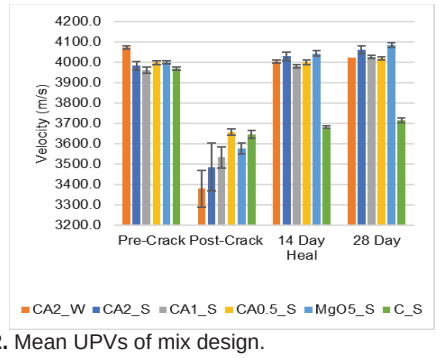

Figure 2. Mean UPVs of mix design.

The mixes with CA and MgO show an increase in velocity in comparison to the control mix after 14 and 28 days, which indicates the internal crack healing.

3.3.2 Surface crack healing

Surface crack widths were measured before and after self-healing by a digital microscope with a resolution of 1.3 megapixels (1280x1024 pixels). Figure 3 shows the visual healing of the specimen. Additionally, through investigations under a microscope, the crack widths have been documented.

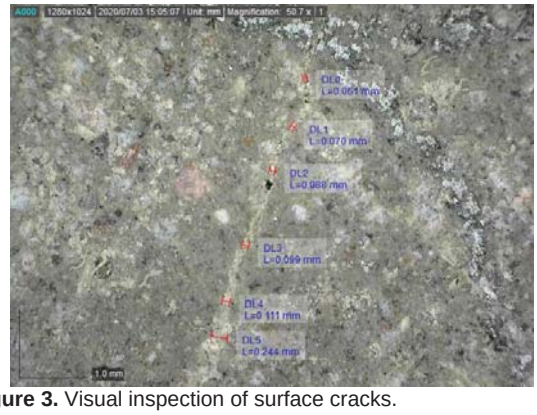

Figure 3. Visual inspection of surface cracks.

The percentage of average healed cracks of beam specimens at 28 days are shown in Figure 4. The beam specimens with a higher dosage of CA experience more healing than other samples.

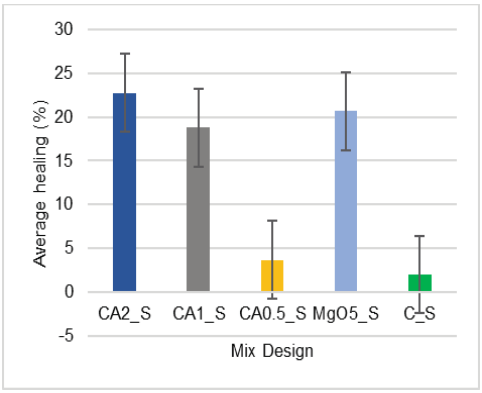

Figure 4. Average healed cracks at 28 days.

3.4 Mechanical recovery of strength

The self-healing efficiency of internal cracks could be indirectly interpreted with regain of mechanical strength. Figure 5 shows the strength recovery of the pre-cracked sample. CA2_S show a higher recovery of strength suggesting the internal healing of the cracks. CA2_S indicates a 37% regain in strength as compared with the pre-cracked sample. Similarly, 28.5% and 12.5% of regain in strength with CA1_S and CA0.5_S, respectively. SMgO5 did not report any form of regain in stiffness. However, existing literature suggests the regain of strength with 4% of MgO (Qureshi *et al.*, 2018).

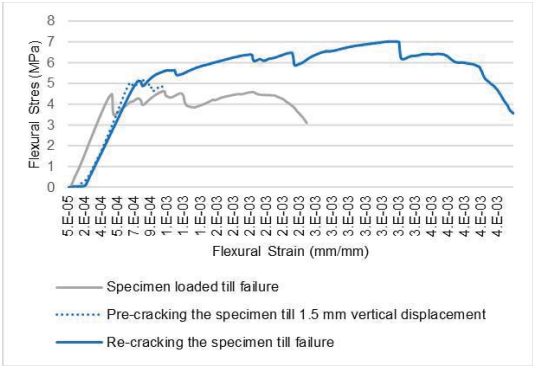

Figure 5. Flexural strength recovery of pre-cracked specimen at 28 days.

Control specimens show a 20% regain in strength possibly due to the further hydration of cement and Fly ash. However lower than the mix with CA. Therefore, it can be concluded that CA was the variable that possesses the potential to regain the mechanical properties of a cracked cementitious material.

3.5 Water Permeability

Self-healing efficiency can be interpreted by the amount of water flow in the healed specimen after the healing exposure condition. Water permeability at different healing periods is shown in Figure 6. The samples with healing agents show a reduction in permeability compares with the control specimens. Self-healing efficiency is higher in the initial days (first 14 days), reduction in permeability indicates the self-healing of internal cracks. Similarly, UPV results on beam specimens show more healing in the early days.

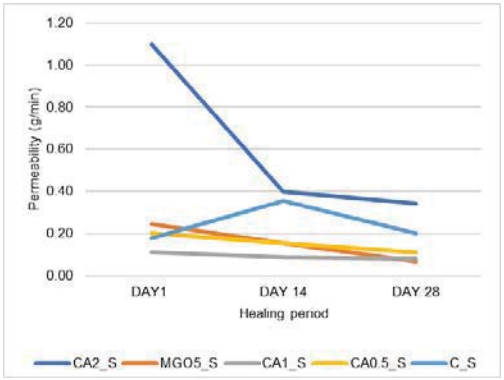

Figure 6. Permeability of mixes.

MgO5_S indicates a 73% reduction in permeability after 28 days (Figure 7). Similarly, specimens with CA shows a decrease in permeability. However, the increment in the dosages of CA is not following any trend with the reduction in permeability. There is no decrease in permeability demonstrated in the control specimen instead permeability increased after 28 days it might further increase in cracks or experimental error.

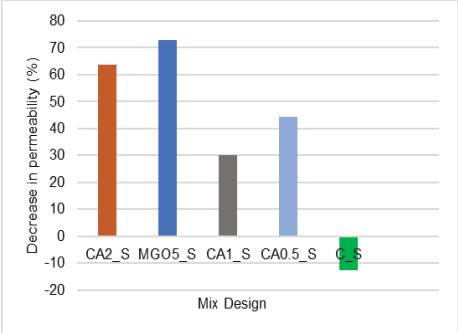

Figure 7. Decrease in permeability of mixes at 28 days.

4. CONCLUSIONS

This paper presents the experimental investigation of the self-healing performance of steam cured ECC mixes, and the following findings and conclusions are:

Mechanical strength and Crack width analysis:

- The mechanical recovery of flexural strength and stiffness was noticed in the samples with CA, but there is no regain in strength with the samples contains MgO. The hypothesis of not obtaining the regain was steam curing of the specimens. Therefore, the conclusion could be considered after the completion of the experimental program, which involves water curing.
- The increased quantity of CA achieved significant healing ability than that of its lowered CA content. Dosages of both 1% and 2% CA demonstrated sufficient healing capabilities both crack closure and under regain in flexural strength. Through visual inspection of 2% and 1%, average visible crack closure was found to be 23% and 19% respectively. It was further validated using UPV were healing after 28 days performed increased velocities of 16% at 2% CA dosage and 14% with a concentration of 1%.
- UPV analysis indicated the rate of healing was most significant within the initial 14 days of environmental conditioning. CA2_S specimens show 15.57% average healing within the initial 14 days, while only an additional 0.90% was documented within the final 14 days.

Permeability analysis:

- The experimental results were evidence the permeability of specimens decreases with time, especially with mixes contains healing agents which indicates the internal healing of the cracks.
- The specimen with 5% of MgO indicates a 73% reduction in permeability on the 28th day. Similarly, 69%, 30% and 44% reduction in permeability observed in the 2%, 1% and 0.5% of CA specimens. There is no reduction in permeability noticed in the control specimens.

REFERENCES

EFNARC (1999) *Guidelines for specifiers and contractors*, *Concrete*.

ICE (2018) 'State of the Nation 2018: Infrastructure Investment'. Available at: https://www.ice.org.uk/ICEDevelopmentWebPortal/media/Documents/Media/Policy/ICE-SoN-Investment-2018.pdf.

Li, V. (2008) 'Engineered Cementitious Composite (ECC): Material, Structural, and Durability Performance', in *Concrete Construction Engineering Handbook*, pp. 1–47.

Martin, J. (2018) 'Developing new statistics of infrastructure : August 2018', (August), pp. 1–19. Available at: https://www.ons.gov.uk/economy/economicoutputandproductivity/productivitymeasures/articles/developingnewmeasuresofinfrastructureinvestment/augusy2018.

Pattnaik, R. (Clemson U. (2006) 'Investigation into compatibility between repair material and substrate concrete using experimental and finite element methods', p. 168. Available at: http://tigerprints.clemson.edu/all_dissertations.

Qureshi, T., Kanellopoulos, A. and Al-Tabbaa, A. (2018) 'Autogenous self-healing of cement with expansive minerals-I: Impact in early age crack healing', *Construction and Building Materials*. Elsevier Ltd, 192, pp. 768–784. doi: 10.1016/j.conbuildmat.2018.10.143.

Rana, S., P, S., Fangueiro, R. and Gomes Correia, A. (2016) 'A review on smart self-sensing composite materials for civil engineering applications', *AIMS Materials Science*, 3(2), pp. 357–379. doi: 10.3934/matersci.2016.2.357.

Roig-Flores, M., Moscato, S., Serna, P. and Ferrara, L. (2015) 'Self-healing capability of concrete with crystalline admixtures in different environments', *Construction and Building Materials*, 86. doi: 10.1016/j.conbuildmat.2015.03.091.

Roig-Flores, M., Pirritano, F., Serna, P. and Ferrara, L. (2016) 'Effect of crystalline admixtures on the self-healing capability of early-age concrete studied by means of permeability and crack closing tests', *Construction and Building Materials*. Elsevier Ltd, 114, pp. 447–457. doi: 10.1016/j.conbuildmat.2016.03.196.

Sánchez, M., Faria, P., Ferrara, L., Horszczaruk, E., Jonkers, H. M., Kwiecień, A., Mosa, J., Peled, A., Pereira, A. S., Snoeck, D., Stefanidou, M., Stryszewska, T. and Zając, B. (2018) 'External treatments for the preventive repair of existing constructions: A review', *Construction and Building Materials*, 193, pp. 435–452. doi: 10.1016/j.conbuildmat.2018.10.173.

Sisomphon, K., Copuroglu, O. and Koenders, E. A. B. (2012) 'Cement & Concrete Composites Self-healing of surface cracks in mortars with expansive additive and crystalline additive', *Cement and Concrete Composites*. Elsevier Ltd, 34, pp. 566–574. doi: 10.1016/j.cemconcomp.2012.01.005.

Young Researchers' Forum V
Innovation in Construction Materials
22 April 2021

The limiting factors for metakaolin reaction in cement at late ages

Yosra Briki and Karen Scrivener
Department of materials science, EPFL, Switzerland

Mohsen Ben Haha
Heidelbergcement, Germany

ABSTRACT

The objective of this study is to understand the factors slowing down the reaction of metakaolin in LC3 cement paste at late ages. The availability of portlandite and aluminum ions in the pore solution were showed to be not the reason for the slowing down of metakaolin reaction. At late ages, the growth of hydrates is limited in fine pores due to the insufficiency of saturation indexes to balance the increase of the surface energy related with the pore curvature. On the other hand, when samples are pore solution cured, a full reaction was obtained at 90 days of hydration with a complete portlandite depletion. This result was explained by the extend reaction in water-filled capillary pores

1. INTRODUCTION

Replacement with different SCMs in cements is one of the potential alternatives to reduce CO_2 emissions related to cement production. However, blended cements present some limitations. First, and depending on clinker replacement levels, blended cements show lower early age strength development compared to PC resulting from the lower reactivity of SCMs, in particular slag and fly ash. Secondly, at later age, SCMs slow down their own reaction (Avet and Scrivener, 2018) (Durdziński, Ben Haha, Zajac, and Scrivener, 2017) and (Berodier, 2015). Since there is a lack of data to explain the factors that could limit or inhibit SCMs reaction, this study investigates several hypotheses that could explain the slowing down at late ages.

2. MATERILAS AND MIX DESIGNS

Besides PC, clinker was blended with calcined clay (30%) and limestone (20%) for a replacement level of 50% to have the cement LC3. Calcined clay contains 48% of metakaolin in the composition and the rest are impurities. The water to cement ratio used in this study is 0.4. To investigate the lack of portlandite availability, 5% of portlandite was added to LC3 system. To investigate the impact of aluminum ions on metakaolin reactivity, metakaolin was replaced by silica fume. The samples were sealed cured. LC3 cement was also cured under pore solution to fill the capillary pores.

3. RESULTS

Lack of portlandite

Since calcined clay is pozzolanic and depends on portlandite presence, the hypothesis was that at later age, portlandite is not accessible anymore for calcined clay reaction. For this reason, 5% more of portlandite was added to LC3 and portlandite content in all system is plotted in **Error! Reference source not found.**. It is clear that at early age, higher reaction of calcined clay with more portlandite. At later age, the addition of portlandite did not improve the reaction of calcined clay although the presence of portlandite. Thus, the availability of portlandite is not the reason for the slowing down of metakaolin reaction at late ages.

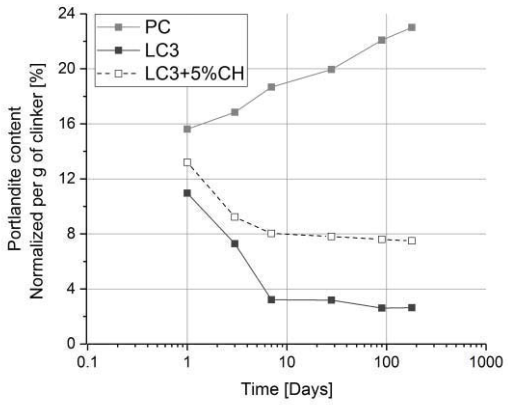

Figure 1. Portlandite content in LC3 with and without addition of portlandite

Impact of aluminum ions in the pore solution

Aluminum ions released in the pore solution could inhibit silicate phases dissolution (Begarin et al, 2013) and (Snellings, 2013). For this reason, metakaolin was replaced by silica fume which does not contain aluminum in its composition. The degree of hydration of clinker even when using Al-free SCM, slowed down at late ages (**Error! Reference source not found.**). The reaction of silica fume is similar to that of the metakaolin in calcined clay at late ages (**Error! Reference source not found.**). The outcome of this experiment shows that the aluminum present in the pore solution is not responsible for the slowing down of metakaolin reaction.

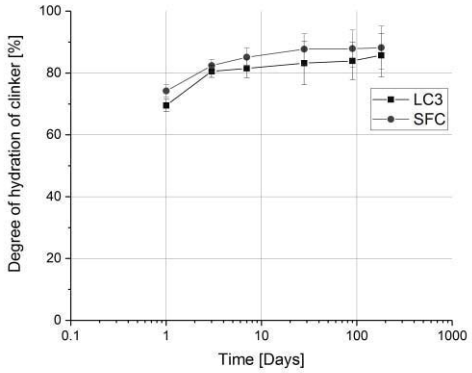

Figure 2. Degree of hydration of clinker in LC3 and silica fume cement

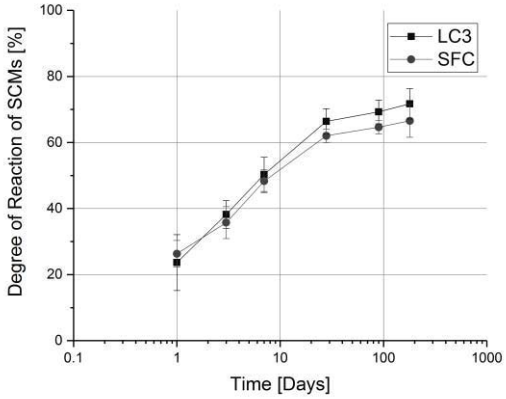

Figure 3. Degree of reaction of metakaolin and silica fume

Growth of hydrates below and above a critical pore size

The study showed that the growth of hydrates is limited in fine pores due to the insufficiency of saturation indexes. The lower the pore radius, the higher is the saturation index required to balance the increase of the surface energy related with the pore curvature as showed in **Error! Reference source not found.**.

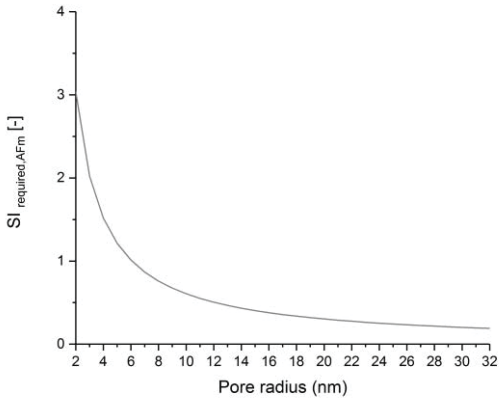

Figure 4. Saturation index of AFm phases vs pore radius (nm)

On the other hand, capillary pores at late ages are emptied of water. When samples are pore solution cured, a full reaction was obtained at 90 days of hydration (**Error! Reference source not found.**) with a complete portlandite depletion (**Error! Reference source not found.**). However, the capillary pores in sealed cured system remain unfilled due to the lack of water.

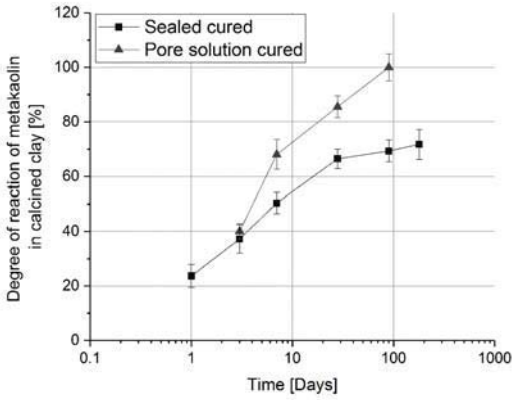

Figure 5. Degree of reaction of metakaolin in LC3 in sealed and pore solution cured systems

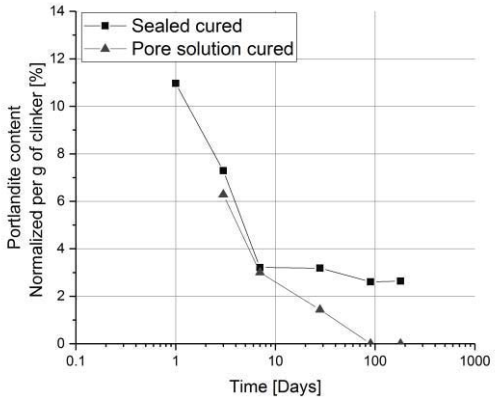

Figure 6. Portlandite content in LC3 in sealed and pore solution cured systems

4. Conclusions

The present paper showed that the lack of portlandite and the presence of aluminum ions in the pore solution are not responsible for the slowing down of metakaolin reaction at late ages. However, this study showed that the growth of hydrates in fine pores is limited due to the low saturation index required to balance the increase of the surface energy related with the pore curvature. On the other hand, when filling the capillary pores when samples are under pore solution cured, metakaolin achieve a full reaction at late ages explained by the depletion of portlandite.

References

F. Avet and K. Scrivener, “Investigation of the calcined kaolinite content on the hydration of Limestone Calcined Clay Cement (LC3),” *Cem. Concr. Res.*, vol. 107, no. February, pp. 124–135, 2018.

P. T. Durdziński, M. Ben Haha, M. Zajac, and K. L. Scrivener, “Phase assemblage of composite cements,” *Cem. Concr. Res.*, vol. 99, no. May, pp. 172–182, 2017.

E.M.J.Berodier, “Impact of the Supplementary Cementitious Materials on the kinetics and microstructural development of cement hydration,” vol. 6417, p. 154, 2015.

F. Begarin *et al.*, “Hydration of alite containing aluminium,” vol. 6753, 2013.

R. Snellings, “Solution-Controlled Dissolution of Supplementary Cementitious Dissolution Rates,” vol. 2475, 2013.

Young Researchers' Forum V
Innovation in Construction Materials
22 April 2021

Application of Superabsorbent Polymers in blended cement mortars reinforced by polymeric fibre

Rohollah Rostami *[1a], Agnieszka J Klemm[1] and Fernando C. R. Almeida[2]

Glasgow Caledonian University, School of Computing, Engineering and Built Environment
Federal University of Minas Gerais, Department of Materials Engineering and Construction

ABSTRACT

Superabsorbent polymers (SAP) have been proved to be an effective internal curing agent which facilitate hydration process and control water supply of cement-based materials in the fresh, hardening, and hardened states. Although the use of SAP in concrete has been previously documented, however, its effect on prolonged hydration, microstructure alteration and mechanical characteristics of fibre reinforced mortars with supplementary cementitious materials (FRM-SCM) still remains unclear and deficient. This paper provides an overview of the effect of Superabsorbent polymers (SAPs) on short- and long-term performance of FRM-SCM. The experimental results confirmed that the addition of SAP to FRM leads to notable reduction of workability and it has a dominant influence on mitigation of shrinkage of FRM-SCM. SAPs facilitate SCM hydration by a prolonged supply of water, adhered to smaller pores and by provision of space for deposition of secondary hydration products. Finer SAP is more effective and more efficiently facilitate improvement of compressive strength.

1. INTRODUCTION

The wide popularity of blended cement is mainly justified by their improved performance when compared to plain Portland cement and by the lower environmental impact (Scrivener et al., 2015). In early ages, the contribution of SCMs to strength development is generally negligible due to slower reactions. Furthermore, concrete with SCMs can be more susceptible to early age cracking, induced by self-desiccation and shrinkage processes (Wyrzykowski and Lura 2016). Nevertheless, SCMs have the major effect on hydration kinetics and enhancement of the reaction of clinker components due to their physical presence, this is known as "filler effect". First, partial replacement of PC clinker by FA or GGBS, at the same w/b ratio, implies a dilution effect. The higher replacement the larger space is available for the formation of clinker hydrates at early ages. Therefore, the degree of reaction of clinker component in blends containing FA or GGBS is significantly higher than in PC cements. One the other hand, SCM surfaces may act as nucleation sites for the hydrates (Scrivener, Juilland and Monteiro 2015, Scrivener et al. 2015). However, this effect is fast for the species in the pore solution and the distribution of C-S-H is quite homogeneous. Moreover, it is relatively minor due to particle size of SCMs (FA and GGBS), which have similar sizes to PC (Berodier and Scrivener 2014). Polymeric fibres (PF) are commonly used in concrete as a strengthening material in order to enhance mechanical capacity. However, their efficiency is often limited, particularly in blended cements (Rostami et al. 2021a), and some form of internal curing may be required to decrease self-desiccation and promote cement hydration. As it has been previously reported SAP ability to provide water during hydration process, which can be used to further reduce these phenomena (Snoeck et al. 2015; Almeida, and Klemm, 2018; Rostami, and Klemm, 2019; Almeida, Rostami, and Klemm, 2019; Rostami, and Klemm, 2020). However, their effectiveness depends on a number of parameters, including their chemical composition, particle grading and ionic concentration in surrounding pore solution.

The main body of the paper is to present the current state-of-the-art and to provide an overview of SAP as a new admixture, highlighting its effects in FRM-SCM matrices.

2. SUPERABSORBENT POLYMERS

There has been significant interest on use of Superabsorbent Polymers (SAPs) in cement-based materials in the recent years. SAP is a natural or synthetic water-insoluble three-dimensional network of polymeric chains, with the ability to absorb aqueous fluids from the environment (Mechtcherine and Reinhardt, 2012; Mechtcherine et al., 2014; Rostami et al. 2021b). When the dry

three-dimensional network with chemical cross-links of SAP get in contact with fluid, the water molecules diffuse into the void space inside the polymer network to hydrate polymer chains and swollen polymer gel is formed (Mechtcherine and Reinhardt, 2012). This process is reversible due to dilution of surface charges, reduction of osmotic pressure and removal of water, resulting in collapsing of SAP (Mechtcherine and Reinhardt, 2012). Figure 1 presents schematic diagram of absorbency and swelling of SAP.

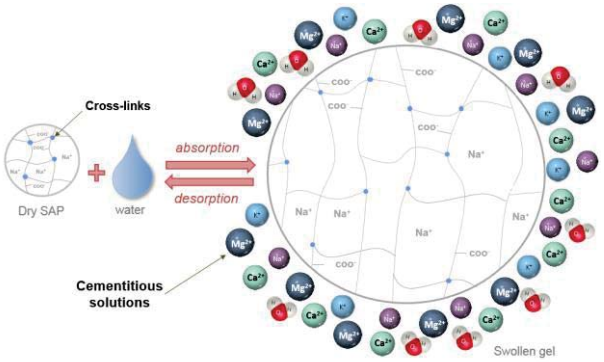

Figure 1. Schematic diagram of absorbency of SAP.

To demonstration the effect of SAPs on FRM-SCM systems, two different types of SAP were analysed (Table 1).

Table 1. Characterization of SAPs.

Properties	SAP A	SAP E
Type of polymer	copolymer of acrylamide and acrylic acid	modified polyacrylamide
Particles size (μm)	30-140	20-130
Modes values (μm)	102.51 ± 0.43	76.74 ± 0.22
WAC[1] $_{\text{deionized water}}$ (by tea-bag test)	340 g/g	340 g/g
WAC $_{\text{CEM II/B-V Solutions}}$ (by tea-bag test)	33 g/g	46 g/g
WAC $_{\text{CEM III/A Solutions}}$ (by tea-bag test)	25 g/g	40 g/g

[1] WAC: water absorption capacity

Two series of mortars (CEM II/B-V 32.5R and CEM III/A 42.5N) with micro polypropylene fibres (6 mm length) have been designed for the experimental tests (Table 2).

Table 1. Mortars samples composition

Cement	Sample Name	PF Content	SAP Content	$(w/b)_{eff}$ ratio	$(w/b)_{total}$ ratio
CEM II	II	-	-	0.47	0.45
	IIF	0.50%	-	0.47	0.50
	IIF-A	0.50%	0.25%	0.47	0.56
	IIF-E	0.50%	0.25%	0.47	0.57
CEM III	III	-	-	0.47	0.48
	IIIF	0.50%	-	0.47	0.52
	IIIF-A	0.50%	0.25%	0.47	0.58
	IIIF-E	0.50%	0.25%	0.47	0.58

Tests of workability, plastic shrinkage (at 24 h), autogenous shrinkage (up to 90 days) and mechanical properties were performed.

3. Effect of SAPs on workability

Figure 2 illustrates results of consistency measurements of mortars modified by SAPs. Due to the absorption of part of mixing water by SAPs all two sets of samples demonstrated a loss of workability.

A similar trend was observed with respect to the effect of SAP addition. The lowest flow values were obtained for mortars with SAP E due to the highest WAC. This could be attributed to smaller particle sizes of this SAP and consequently the higher relative access to mixing water. On the contrary, SAP A had the least effect on the consistence (more fluid) among all SAP samples. The lower slump flow values of SAP A mortars in comparison to those with SAP E results from different kinetics of absorption. With regard to the better workability of SAP E, additional explanations can be given.

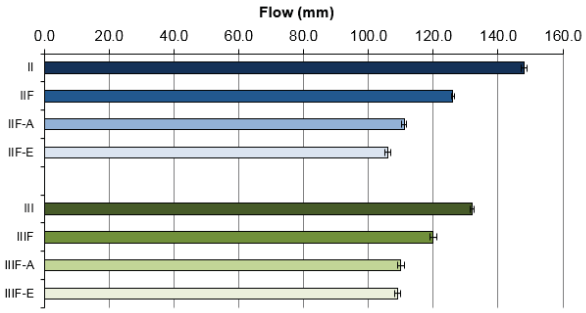

Figure 2. Schematic diagram of absorbency of SAP.

Furthermore, better workability of samples with SAP E is also related to a dilution effect of blended cements ions by the presence of solid particles (sand) in the mix. This may restrict the swelling behaviour of SAP. Other factors influencing workability of SAP include smaller particle sizes of SAP E; absorption of SAPs in blended cements solutions was not comparable to SAP absorption in mortars.

4. Effect of SAPs on mitigation of shrinkage

SAP leads to a significant additional reduction in plastic, and autogenous shrinkage (compared to a conventional fibre reinforced mortar with SCM). However, the level of efficiency depends on either particle sizes and/or water absorption capacity (WAC).

The greatest effect on crack propagation in plastic shrinkage, can be achieved by the application of fine SAP (Table 1) with high WAC (Figure 2).

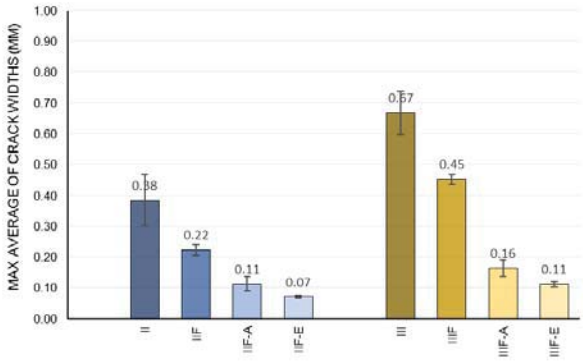

Figure 3. Maximum averages of crack widths (mm).

Overall, CEM II/B-V mortars had the narrowest cracks and CEM III/A mortars the widest cracks. This can be attributed to a decrease of total bleeding water and bleeding rate of fly ash cement.
Furthermore, it is related to the lower w/b of CEM II/B-V samples, and lower susceptibility to plastic shrinkage cracking. On the contrary, in CEM III/A samples, GGBS leads to prolonged setting times, resulting in higher bleeding rate. This, in turn, results in advanced tensile capillary pressure and the higher probability of plastic shrinkage cracking. Moreover, the addition of polymeric fibres reduces PS by providing bridging forces across the cracks.
Figure 4 shows development of autogenous shrinkage (AS) in the mortars during the first 90 days.

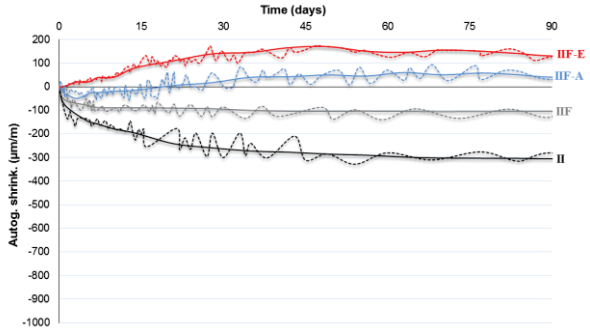

(a)

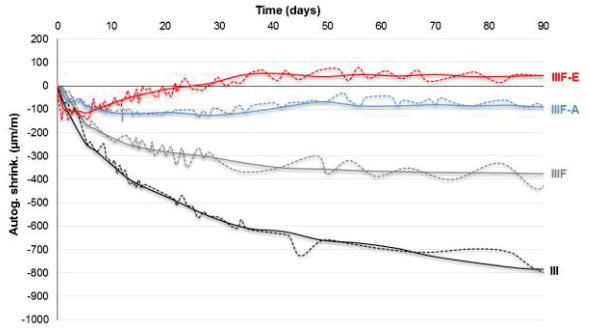

(b)

Figure 4. The autogenous shrinkage (AS) (a) CEM II and (b) CEM III.

All SAP samples experienced a noticeable volume expansion during the first 45 days, in particular mortars with SAP E. SAP E experienced higher expansion due to SAP fineness and faster absorption kinetics (Table 1).

SAPs promote precipitation of further C-S-H phases (later reactions of FA and GGBS) leading to an overall bulk expansion of hardened matrix.
This effect is more prominent for SAP E due to its very fine particles and greater water absorption capacity for all cementitious solutions (Table 2).

5. Effect of SAPs on microstructure alterations

Microstructural development in cementitious composites is strongly dependent on type of binder used and a lifespan exposure to environmental conditions. In particular, the use of SCM such as FA or GGBS, has an important impact on hydration kinetics and subsequent strength development (Vanderley et al. 2019; Almeida, and Klemm, 2018).
The presence of SCM and SAP has a significant influence on microstructure development of fibre reinforced mortars, in particular on their overall porosities and pore size distributions (Rostami and Klemm 2020). The presence of SAPs can alter microstructural features of concrete, due to formation of macro pores as a result of collapsing of polymer. In spite of the presence of these voids (i.e., less physical filling effect), the strength loss can be mitigated by the later intensified hydration by SAP, especially in blended cements with the longer lasting reactions.

6. Effect of SAPs on mechanical properties

Figure 5 show the results of compressive strength development for all samples. As anticipated all SAPs had a negative effect on strength development at early age because of the formation of “extra” pores after collapsing of SAP. Reduction of compressive strength during the first 14 days depends predominantly on particle sizes; the larger

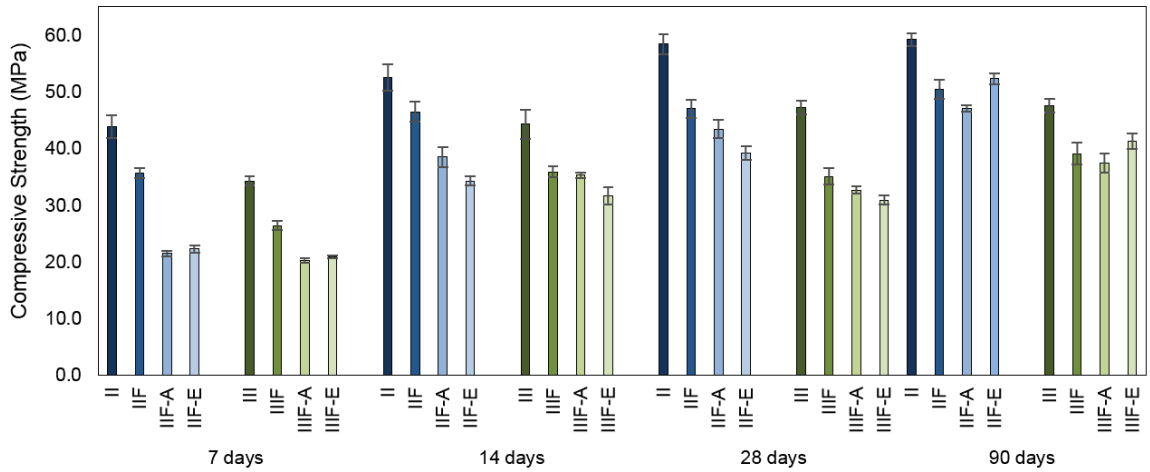

Figure 5. Compressive strength results of all mortars.

pores and hence the larger reduction of strength. Although all SAPs lowered the strength at early ages, this negative effect was significantly minimised at later age. SAP E with smaller particle sizes was more effective and by the age of 90 days its improved strength by nearly 45% (Figure 5).

4. CONCLUSION

The application of SAP has major influence on the fresh state properties of fibre reinforced mortars containing SCMs. The addition of SAP to FRM leads to notable reduction of workability and is closely related to total absorption capacity of SAP.
The highest reduction of workability was recorded for samples with SAP E due to the highest water absorption capacity (WAC) of this SAP.
SAP facilitate substantial additional reduction in plastic, and autogenous shrinkage in FRM-SCM. However, the level of efficiency depends on either particle sizes and/or water absorption capacity (WAC).
Particle sizes of SAPs have a very strong effect on microstructure development of fibre reinforced mortars, in particular on their overall porosities and pore size distributions.
SAPs had a negative effect on compressive strength development at early age because of the formation of “extra” pores after collapsing of SAP. Initial reduction of the compressive strength of SAP modified mortars can be later recovered. Finer SAP is more effective and more efficiently facilitate improvement of compressive strength.

References

Almeida, F. C. R., and Klemm, A. J. (2018). “Efficiency of internal curing by superabsorbent polymers (SAP) in PC-GGBS mortars.” Cement and Concrete Composites, 88, 41–51.

Almeida, F.C.R., Rostami. R., Klemm, A.J. Characterization of Polyacrylamide based Superabsorbent Polymers for potential use in PC Matrices with Supplementary Cementitious Materials. MATEC Web of Conferences, 2018, 199, 02023.

Almeida, F.C., Rostami, R. and Klemm, A.J., 2019, November. The Effect of SAP on Volumetric Changes and Microstructural Alterations in PC-GGBS Matrices. In International Conference on Application of Superabsorbent Polymers & Other New Admixtures Towards Smart Concrete (pp. 97-105). Springer, Cham.

Berodier, E.S.K.S.G. and Scrivener, K., 2014. Understanding the Filler Effect on the Nucleation and Growth of C-S-H. Journal of the American Ceramic Society, 97(12), pp.3764-3773.

John, V.M., Quattrone, M., Abrão, P.C. and Cardoso, F.A., 2019. Rethinking cement standards: Opportunities for a better future. Cement and Concrete Research, 124, p.105832.

Mechtcherine, V. and Reinhardt, H.W. eds., 2012. Application of super absorbent polymers (SAP) in concrete construction: state-of-the-art report prepared by Technical Committee 225-SAP (Vol. 2). Springer Science & Business Media.

Mechtcherine, V., et al. Testing superabsorbent polymer (SAP) sorption properties prior to implementation in concrete: results of a RILEM Round-Robin Test. Materials and Structures, 2018, 51:28.

Snoeck, D., Schaubroeck, D., Dubruel, P. and De Belie, N. Effect of high amounts of superabsorbent polymers and additional water on the workability, microstructure and strength of mortars with a water-to-cement ratio of 0.50. Construction and Building Materials, 2014, 72, pp.148–157.

Scrivener, K. L., Lothenbach, B., De Belie, N., Gruyaert, E., Skibsted, J., Snellings, R., & Vollpracht, A. (2015). TC 238-SCM: hydration and microstructure of concrete with SCMs. Materials and Structures, 48(4), 835–862.

Scrivener, K.L., Juilland, P. and Monteiro, P.J., 2015. Advances in understanding hydration of Portland cement. Cement and Concrete Research, 78, pp.38-56.

Snoeck, D., Jensen, O.M. & De Belie, N. The influence of superabsorbent polymers on the autogenous shrinkage properties of cement pastes with supplementary cementitious materials. Cement and Concrete Research, 2015, 74, pp.59–67.

Rostami, R., Klemm, A.J. and Almeida, F.C., 2021a. Reduction of shrinkage by Superabsorbent polymers (SAP) in fibre reinforced mortars. Construction and Building Materials, 288, p.123109.

Rostami, R., Klemm, A.J. and Almeida, F.C., 2021b. The Effect of SCMs in Blended Cements on Sorption Characteristics of Superabsorbent Polymers. *Materials*, *14*(7), p.1609.

Rostami, R. and Klemm, A.J., 2020. Influence of uperabsorbent polymers on properties of fiber reinforced mortars containing fly ashes. Roads and Bridges, 19, pp.149-163.

Rostami, R. and Klemm, A.J., 2019, March. Effect of superabsorbent polymers on plastic shrinkage cracking and properties of fresh state mortars reinforced by polymeric fibres. In Proceedings of the international conference on sustainable materials, systems and structures (SMSS2019): new generation of construction materials. RILEM (pp. 614-621).

Wyrzykowski, M. Lura, P. Effect of relative humidity decrease due to self-desiccation on the hydration kinetics of cement. Cem Concr Res (2016) 85: 75-81.

Young Researchers' Forum V
Innovation in Construction Materials
22 April 2021

The Effect of Alkali Activation on Absorption capacity of SAP in Ground Granulated Blast Furnace Slag (GGBS) and Copper Slag (CS) Solutions

S. MacLennan and A.J. Klemm
School of Computing, Engineering and the Built Environment, Glasgow Caledonian University, UK

ABSTRACT

This paper discusses the effect of ground granulated blast furnace slag (GGBS) and copper slag (CS) precursor replacement on the sorption characteristics of different superabsorbent (SAP) polymers in alkali activated cement (AAC) solutions. The precursor combinations which have been tested are 100:0, 75:25, 50:50, 25/75 and 0:100 of GGBS and CS respectively.
The tea bag test method has been utilised in this study to evaluate the mass of fluid absorbed. This method can give comparison to the volume of fluid absorbed by the SAP in different pore water solution environments. Sodium Silicate M_s = 2.05 @ 6.5% Na_2O by mass of precursor was maintained and compared with the same precursor combination in de-ionised water. Two SAPs with different chemical compositions and particles size distributions have been used. Quantitative data has been collected chronologically in order to assess the effect of activator on the rate and mass of fluid absorbed. Additionally, pH and temperature measurements have been monitored throughout the test.
The fundamental outcome of the study is that the addition of activator and inclusion of copper slag can reduce the absorption capacity of SAP. Particle size of SAP has less of an impact on the rate of absorption than initially expected.

1. INTRODUCTION

It is well-known fact that production of widely used Portland cement is one of the major contributors to greenhouse gases emissions. In an attempt to increase sustainability of concrete, supplementary cementitious materials, such as, ground granulated blast-furnace slag (GGBS) and less popular, copper slag can be used replace PC (Singh & Singh, 2019 Lan, Wu & Yu, 2020 Feng *et al.*, 2019 Wang *et al.*, 2019). Both slags possess some hydraulic properties but require alkali activation to match the pace of strength development of PC, particularly during the first 14 days. This in turn makes the composite more susceptible to cracking, triggered by self-desiccation processes and subsequent autogenous shrinkage. The addition of Superabsorbent Polymers (SAP) has proven to be effective in enabling internal curing (IC) of concrete (Dang, Zhao & Du., 2017 Lyu *et al.*, 2019 Hasholt & Jensen, 2015). SAP provides additional water for a greater period of time during cement hydration, this supplemental water at later stages results in densification of the paste matrix and shrinkage reduction.
Generally, SAPs are crosslinked polyelectrolytes with high swelling capacity in aqueous media. SAPs have the ability to absorb up to 500 times their own weight in aqueous solutions due to osmotic pressure. When in contact with water they form a hydrogel (Snoeck et al., 2014, Al-Nasra., 2019). Their long-term storage capacity and swelling kinetics may vary due to their molecular structure (cross linking), temperature, pressure and ionic concentration of solution.

This aim of this paper is to present the results of study of absorption capacities of SAPs in alkali and non-alkali activated solutions containing GGBS and CS. SAPs with the same chemical compositions (modified polyacrylamide) and different particle size distributions (here called SAP C and SAP E) have been used to assess their effect on the sorption mass. SAP E has smaller particle sizes (between 20 and 130 μm) than SAP C (between 30 – 140 μm). Samples of SAPs were provided by BASF and they are proprietary materials.

2. Methodology

Sorption characteristics were evaluated by gravimetric tea-bag method (Mechtcherine et al., 2018). The method has been chosen because of its simplicity. Water absorption by SAPs in different solutions containing GGBS and CS has been measured. Five solutions were prepared for this test with different proportion of GGBS and CS. The following combinations of precursor have been tested: 100:0, 75:25, 50:50, 25/75 and 0:100 of GGBS and CS respectively. Two sets of solutions

were prepared - one with sodium silicate as an activator, and the other set without activator. Sodium Silicate M_s = 2.05 @ 6.5% Na_2O by mass of precursor was maintained and compared with the same precursor combination in de-ionised water. The prepared solutions in bottles (Fig 1), were placed on stirrers for 24 hours with a magnet at the bottom to stir the mix.

Figure 1. Solutions prepared and ready for filtering

After 24 hours, the solutions were filtered in order to remove the suspended particles in the fluid and to reduce the possibility of GGBS and CS particles interfering with the water absorption of SAPs. According to the RILEM recommendation (Mechtcherine et al., 2018), the characteristic size of pores was 50 µm for the filters and 200-400 µm for the teabags. After filtration, each solution was poured in two laboratory glass jars (one with SAP and one with no SAP) and the rest was kept in the bottle for pH measurement purposes. A pre-wetted tea-bag was filled with a predetermined and specific mass of dry SAP particles. The mass of SAP used in all experiments was limited to 0.2 grams, in order to avoid exceeding the volume capacity of the teabag.
The water absorption of SAP was measured at time increments up to 3 hours by weighing the teabags with a highly sensitive laboratory scale and calculating the mass of fluid absorbed by the SAPs. The readings were taken at 1, 5, 10, 30, 60, 180 min. After weighing, the tea-bag/hydrogel was returned to the test solution until the next weighing step. In the meantime, the pH of the solutions was measured. Measurements have been carried out using the Fisher Scientific accumet AP110 pH Meter (Fig. 2)

Figure 2. Testing of SAP absorption and pH of solution (photo: Almeida., 2018)

SAP's water absorption capacity (WAC), expressed in grams of absorbed water per gram of dry SAP (g/g), were calculated by Equation (1).

$$WAC = \frac{m_2 - m_1}{m_1} \quad (1)$$

where,
m_1 = mass of dry SAP (g)
m_2 = mass of water-swollen SAP (g)

A potential drawback of this method is the residual interparticle (capillary) liquid that may remain within the samples during wiping and weighing processes (Fořt, Migas & Černý, 2020). Despite the concerns, the tea-bag gravimetric method is the most common and widely accepted quantification technique for SAPs sorptivity assessment (Mechtcherine at al., 2018 Almeida, 2018)

3. Results and Analysis

All tests were carried out in laboratory conditions: temperature of 21°C +/-2°C and RH 55% +/- 5%. As shown on Fig 3 the effect of temperature variations on absorption characteristics of SAP C, effect of activation and GGBS/CS contents are negligible. Similar tendencies are observed for SAP E.

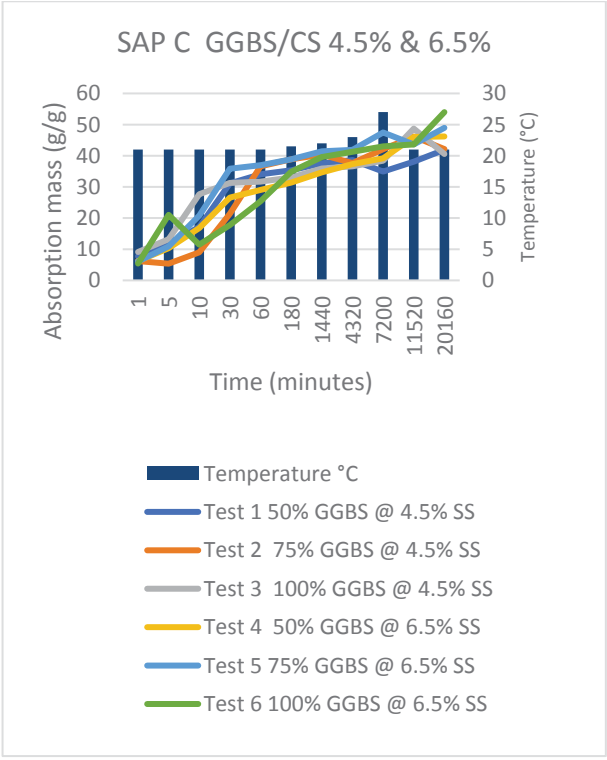

Figure 3. Absorption by SAP C

As widely documented and in concurrence with RILEM recommendations, absorption characteristics of SAP depend very much on the ionic concentration in solution (Snoeck et al., 2017). Hence, absorption of DI water for both SAPs was

substantially higher (up to 5 times), as illustrated in Fig 4 and 5.

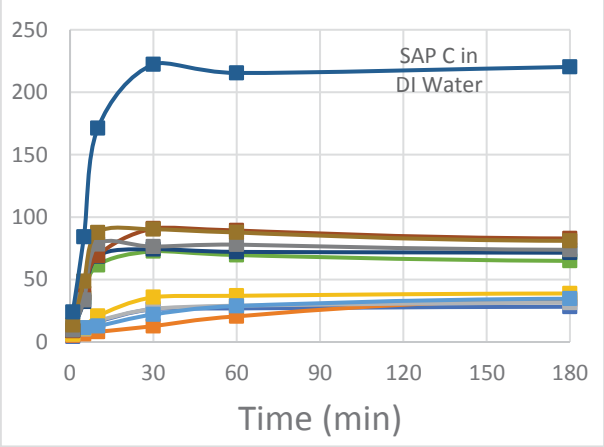

Figure 4. Absorption of SAP C with/without activator

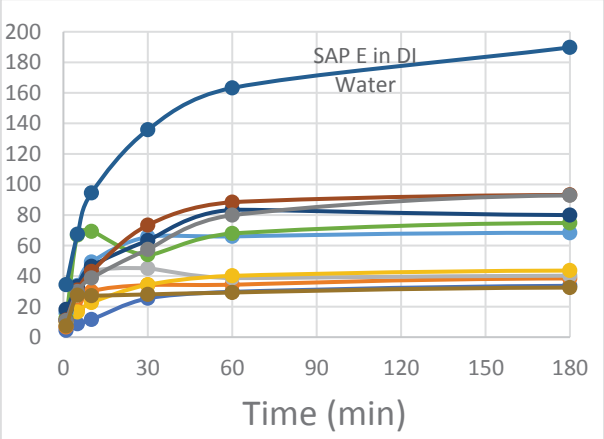

Figure 5. Absorption of SAP E with/without activator

Detailed data of absorption testing is shown on Figures 6 and 7 for SAP C and SAP E respectively. It is evident that the addition of alkali activator (sodium silicate) in the solution significantly reduces absorption capacities of SAPs. When comparing the data for different solutions and no activator it is possible to distinguish two groups of curves – one corresponding to the solutions with activator and the other without activator. The similar patterns occur for SAP C and E. Since both SAPs have the same chemical composition but different particle sizes (SAP C with larger particles) it could be concluded that the grading of SAP is of the secondary importance.

Inclusion of copper slag steadily reduces the absorption capacity and in line with the percentage substitution of GGBS for CS. The greatest absorption takes place in the alkali activated 100% GGBS solution. The lowest final absorptions occur for 100% CS solution with both activator and no activator. The similar patters can be observed for both SAPs.

There is no clear difference in absorption characteristics between for SAP C and E in different solutions. The particle size of the SAP has less of an impact on the rate of absorption than initially expected.

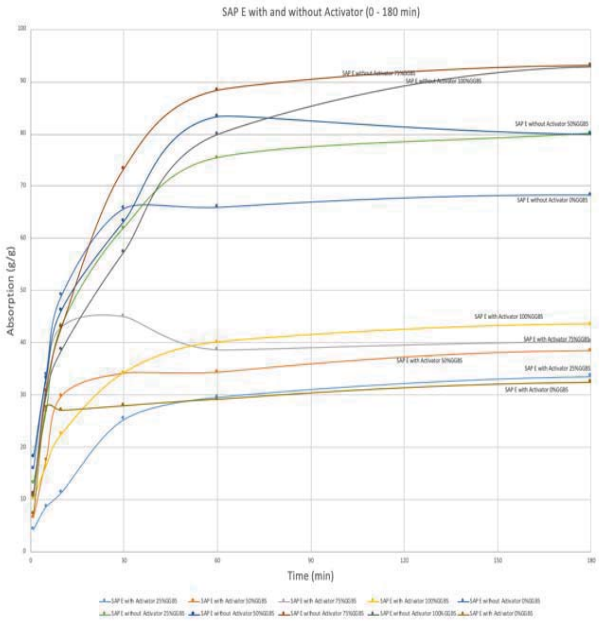

Figure 6. Absorption capacity of SAP E up to 180 minutes in solutions

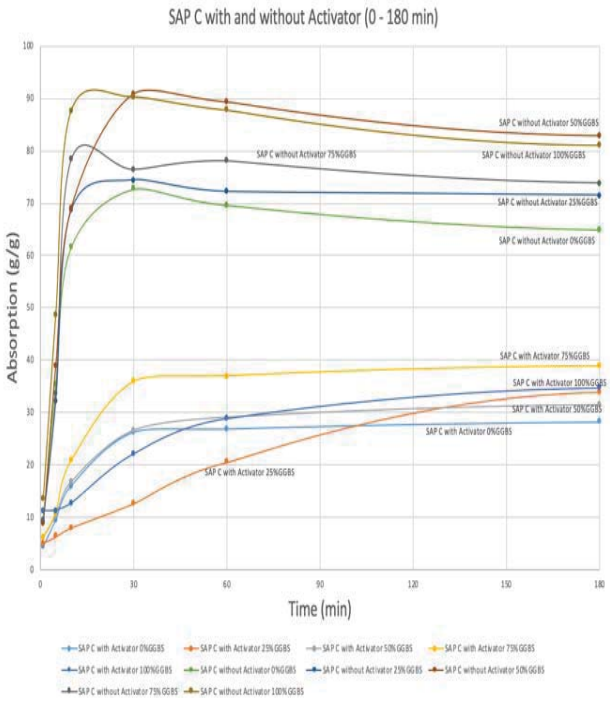

Figure 7. Absorption capacity of SAP C up to 180 minutes in solutions

Table 1 shows pH values for mixes with 50% GGBS with and without activator. Despite some minor initial variation during 30 mins no changes were recorded later. Similar tendencies were recorded for other solutions. The measurement were carried out to establish any potential effect of carbonation.

Since the test was performed during relatively short period of time - 3 hous, no such an effect was noted.

Table 1. pH values for mixes with 50% GGBS with and without activator

	50% GGBS with Activator			50% GGBS without Activator		
	SAP E	no SAP E	Ref	SAP E	no SAP E	Ref
0	12.39	12.39	12.32	9.67	9.67	10.01
5	12.43	12.4	12.45	9.53	9.76	9.62
10	12.29	12.24	12.41	9.57	10.03	9.62
15	12.23	12.19	12.34	9.54	10.04	9.58
30	12.38	12.37	12.38	9.58	10.1	9.68
60	12.42	12.41	12.4	9.59	10.1	9.64
180	12.44	12.43	12.47	9.46	10.1	9.64

4. Conclusions

- Effect of temperature in normal laboratory conditions is negligible.
- Water absorption capacities of SAP in alkali activated GGBS/CS solutions depends mainly on the presence of activation. Reduction of absorption due to alkali activator may be as high as 50%.
- Inclusion of copper slag steadily reduces the absorption capacity
- The greatest absorption takes place in the alkali activated 100% GGBS solution.
- Effect of particle size distribution of SAP is visible (larger particles absorb less water) but it is not dominant.

References

Al-Nasra, M., (2019) Investigating the effect of the ultra-high absorbent polymer on the sealing property of concrete*. Cogent Engineering.* **6**(1), pp.1599550.

Dang, J., Zhao, J. & Du, Z., (2017) Effect of Superabsorbent Polymer on the Properties of Concrete*. Polymers; Polymers (Basel).* **9**(12), pp.672.

Lyu, Z., Guo, Y., Chen, Z., Shen, A., Qin, X., Yang, J., Zhao, M. & Wang, Z., (2019) Research on shrinkage development and fracture properties of internal curing pavement concrete based on humidity compensation*. Construction & Building Materials.* **203**, pp.417-431.

Snoeck, D., Schaubroeck, D., Dubruel, P. and De Belie, N. (2014). Effect of high amounts of superabsorbent polymers and additional water on the workability, microstructure and strength of mortars with a water-to-cement ratio of 0.50. Construction and Building Materials, 72, pp.148–157.

Mechtcherine, V., Snoeck, D., Schröfl, C., De Belie, N., Klemm, A.J., Ichimiya, K., Moon, J., Wyrzykowski, M., Lura, P., Toropovs, N. and Assmann, A., (2018). Testing superabsorbent polymer (SAP) sorption properties prior to implementation in concrete: results of a RILEM Round-Robin Test. Materials and Structures, 51(1), p.28.

Almeida, F.C.R., Klemm, A.J., (2018). Efficiency of internal curing by superabsorbent polymers (SAP) PC-GGBS mortars. Cement and Concrete Composites, 88, pp. 41-51

Snoeck, D., Pel, L. & De Belie, N., (2017). The water kinetics of superabsorbent polymers during cement hydration and internal curing visualized and studied by NMR*. Scientific Reports; Sci Rep.* **7**(1), pp.9514-14.

Singh, J. & Singh, S.P., (2019). Development of Alkali-activated Cementitious Material using Copper Slag*. Construction & Building Materials.* **211**, pp.73-79.

Fort, J., Migas, P. & Černy, R., (2020). Effect of Absorptivity of Superabsorbent Polymers on Design of Cement Mortars*. Materials.* **13**(23), pp.5503.

Lan, W., Wu, A. & Yu, P., (2020). Development of a new controlled low strength filling material from the activation of copper slag: Influencing factors and mechanism analysis*. Journal of Cleaner Production.* 246, pp.119060.

Feng, Y., Kero, J., Yang, Q., Chen, Q., Engstrom, F., Samuelsson, C. & Qi, C., (2019). Mechanical Activation of Granulated Copper Slag and Its Influence on Hydration Heat and Compressive Strength of Blended Cement*. Materials; Materials (Basel).* 12(5), pp.772.

Wang, L., Wei, Y., Lv, G., Liao, L. & ZhangH, D., (2019). Experimental Studies on Chemical Activation of Cementitious Materials from Smelting Slag of Copper and Nickel Mine*. Materials; Materials (Basel).* **12**(2), pp.303.

Hasholt, M.T. & Jensen, O.M., (2015). Chloride migration in concrete with superabsorbent polymers*. Cement & Concrete Composites.* **55**, pp.290-297.

Young Researchers' Forum V
Innovation in Construction Materials
22 April 2021

Optimising the embodied carbon efficiency of composite cements using thermodynamic modelling

S. J. Draper, H. S. Wong and C. R. Cheeseman
Department of Civil and Environmental Engineering, Imperial College London

M. Zajac and M. Ben Haha
HeidelbergCement Technology Center GmbH

ABSTRACT

Composite cements, where Portland cement clinker is partially replaced with supplementary cementitious materials (SCMs), are a key route to addressing the environmental impact of the cement industry. SCMs are typically by-products from other industries or naturally abundant materials with significantly less embodied carbon than Portland cement clinker. Most reactive pozzolanically with the calcium hydroxide formed during the hydration of clinker. At moderate levels of clinker replacement, SCMs can improve the strength and durability of concretes. However, as the SCM content increases, reduced calcium hydroxide availability limits its reactivity, negatively impacting the properties of the cement paste. This work seeks to optimise the SCM blend in clinker-slag-limestone (C-S-L) ternary systems to give the least embodied carbon per unit compressive strength. A relationship was established between porosity calculated from thermodynamic modelling data and measured compressive strength. This relationship was used to estimate the compressive strengths of a broader range of composite cements with clinker replacement levels of up to 90%.

1. INTRODUCTION

The cement industry accounts for 5-8% of anthropogenic CO_2 emissions globally (Baumert, Herzog and Pershing, 2005). About 60% of this is chemically bound in the raw materials and released during the calcination process (The Cement Sustainability Initiative, 2009).

Existing guidelines for designers on the specification of low carbon cements are limited. Whilst designers are encouraged to consider specifying strength requirement at later ages, there is little in the way of translating this into an efficient cement composition. Instead, they are led to choose from a few "typical" mixes, such as 50% GGBFS or 30% fly ash (The Concrete Centre, 2014).

This paper uses experimental data and thermodynamic modelling to explore the relationship between embodied carbon (eCO_2) and compressive strength of systems incorporating ground granulated blastfurnace slag (GGBFS) and powdered limestone at a wide range of replacement levels. From this, appropriate binders can be selected for a required application to minimise the embodied carbon.

2. MATERIALS AND METHODS

2.1. Materials

Composite cements were prepared from a commercial CEM I 52.5R, GGBFS and powdered limestone. Anhydrite was used to control the sulfate content. The materials were supplied by HeidelbergCement. Nine ternary binders were prepared, as given in Table 1, covering a range of 20-60% GGBFS and 10-30% limestone contents. Composite cements were homogenised in a high-shear mixer for 10 minutes at 2000 rpm. All samples were prepared at a w/b ratio of 0.5 and cured at 100% RH until testing at 28 days. 50 mm mortar cubes, with a 3:1 aggregate to binder ratio were prepared for compressive strength testing.

Table 1. Composition of C-S-L ternary binders

Binder	Clinker %wt	GGBFS %wt	Limestone %wt	SO_3 %wt
7C-2S-1L	70	20	10	3.6
6C-2S-2L	60	20	20	3.6
5C-2S-3L	50	20	30	3.6
5C-4S-1L	50	40	10	3.6
4C-4S-2L	40	40	20	3.6
3C-4S-3L	30	40	30	3.6
3C-6S-1L	30	60	10	3.6
2C-6S-2L	20	60	20	3.6
1C-6S-3L	10	60	30	3.6

2.2. Modelling of compressive strength

Geochemical modelling was carried out using GEMS (Wagner *et al.*, 2012; Kulik *et al.*, 2013). Thermodynamic data was taken from the PSI-Nagra database (Thoenen and Kulik, 2003; Thoenen *et al.*, 2014) and supplemented by CEMDATA18 (Lothenbach *et al.*, 2019). The degree of hydration of the individual clinker phases and GGBFS were determined by QXRD and SEM/EDS point counting for the binders in Table 1. Intermediate values were

interpolated. The minor cement constituents, sulfates and limestone were assumed to react freely. The phase assemblage was modelled and porosity calculated at 1% intervals of GGBFS and limestone content. For the binders in Table 1, a power law relationship was fitted between GEMS porosity and the measured compressive strength. This model was used to estimate the compressive strength of intermediate mixes.

2.3. Calculating embodied CO_2

The embodied CO_2 of each binder component (in kg eCO_2 / t) was taken from Bolte *et al.* (2019) and is displayed in Table 2. The total embodied carbon of each composite cement was calculated as the weighted sum of its components:

$$E = \sum X_i e_i \quad \textbf{(1)}$$

where E is the embodied carbon per ton of composite binder, and X_i and e_i are the mass fraction and embodied carbon per ton respectively of each binder component, i (clinker, GGBFS, limestone). Contributions from sulfate additions are omitted.

Table 2. Embodied carbon of binder components from Bolte *et al.* (2019)

Component	kg eCO_2 / t
Clinker	799
GGBFS	85
Limestone	8

3. RESULTS AND DISCUSSION

3.1. Modelling of compressive strength

The degree of hydration of the clinker phases and GGBFS, shown in Table 3 were used in the thermodynamic modelling to compute a phase assemblage at 28 days. These were obtained as part of a larger study and the full details are presented elsewhere (Draper *et al.*, 2021).

Table 3. Degree of hydration of clinker phases and GGBFS at 28 days

Binder	C_3S	C_2S	C_3A	C_4AF	GGBFS
7C-2S-1L	0.970	0.494	0.962	0.883	0.670
6C-2S-2L	0.969	0.460	0.970	0.718	0.599
5C-2S-3L	1.000	0.505	1.000	1.000	0.610
5C-4S-1L	0.986	0.447	1.000	1.000	0.536
4C-4S-2L	1.000	0.162	1.000	1.000	0.556
3C-4S-3L	1.000	0.410	1.000	1.000	0.446
3C-6S-1L	1.000	0.426	1.000	1.000	0.506
2C-6S-2L	1.000	0.215	1.000	1.000	0.546
1C-6S-3L	1.000	0.244	1.000	1.000	0.401

The GEMS porosity, p, was calculated as:

$$p = \left(1 - \frac{\Sigma V_j}{V_m}\right) \times 100\% \quad \textbf{(2)}$$

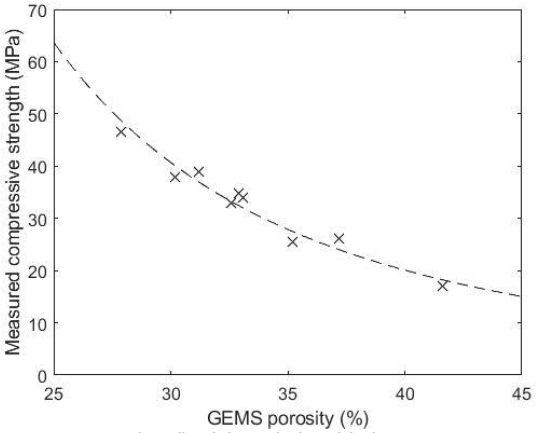

Figure 1. Power-law fit of the relationship between GEMS porosity and compressive strength for the nine initial binders at 28 days

where V_j is the volume of the individual hydrate phases and remaining anhydrous constituents, j, and V_m is the volume of the paste at mixing (assumed to be volume of water plus volume of binder).

The power law fit between the GEMS porosity and measured compressive strength of these binders is shown in Figure 1 and calculated as:

$$\sigma_c = 1.716\, p^{-2.454} \times 10^5 \quad \textbf{(3)}$$

where σ_c is the modelled compressive strength in MPa. Figure 2 shows the modelled compressive strength of mortars at 28 days as a function of binder composition.

The strongest mixes contain a small percentage of both GGBFS and limestone, benefitting from the clinker dilution effect to accelerate the hydration of the clinker, and the formation of hemi- and monocarboaluminate phases that stabilise ettringite and reduce porosity (Lothenbach *et al.*, 2008; Adu-Amankwah *et al.*, 2017). At higher levels of replacement, these effects are outweighed by a reduction in the volume of hydration products from the GGBFS and limestone, resulting in increased porosity and decreased compressive strength. This decline in strength is more severe with increasing limestone content than GGBFS. The slowdown of the late hydration could be attributed to the slow transport of elements dissolved from the reactive surfaces to the precipitation related to the low water content or high tortuosity of well hydrated slag containing cementitious matrixes (Zajac *et al.*, 2020). The role of excess GGBFS is identical to that of the limestone - a filler. At this point, the strength contours become parallel to the (dotted) lines of constant clinker replacement.

3.2. Optimising embodied carbon per unit strength

Figure 3 plots the embodied carbon efficiency of C-S-L binders expressed in terms of kg eCO_2 per MPa

of compressive strength at 28 days. This may be of use for the design of structures where the geometry can be altered and a structural element could be resized to use a more efficient binder and reduce the total embodied carbon.

From this model, CEM I has an efficiency of 12.9 kg/MPa and the C-S-L binders range from 6.3 - 16.7 kg/MPa. Limestone additions of more than 2% appear to have a little effect on the embodied carbon efficiency when replacing clinker or a deleterious one when used instead of GGBFS.

The data in Figure 4 suggests that reducing clinker content increases the relative compressive strength gain between three and seven days. This increase is greatest in mixes with a high limestone content. As such, these mixes may offer better eCO_2 efficiencies at seven days.

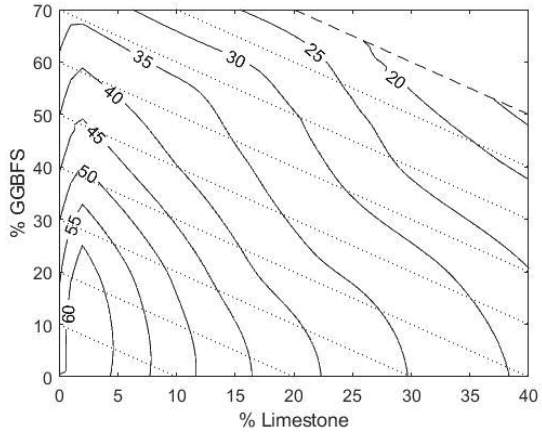

Figure 2. 28-day compressive strength (in MPa) of C-S-L mortars as a function of binder composition

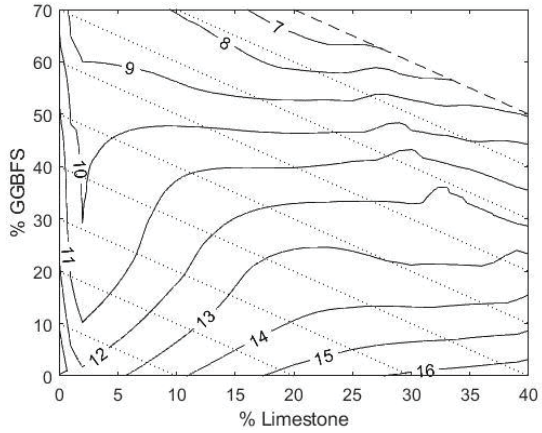

Figure 3. eCO_2 efficiency (in kg eCO_2 / MPa) of C-S-L binders as a function of binder composition at 28 days

Table 4. Effect of 28-day strength requirement on the minimum eCO_2 of cements conforming to EN197-1 class CEM II/B-M (S-L)

28d strength requirement MPa	Clinker %wt	GGBFS %wt	Limestone %wt	kg eCO_2 / t
20	65	0	35	522
30	65	0	35	522
40	66	16	18	542
50	66	27	7	551
60	75	22	3	618

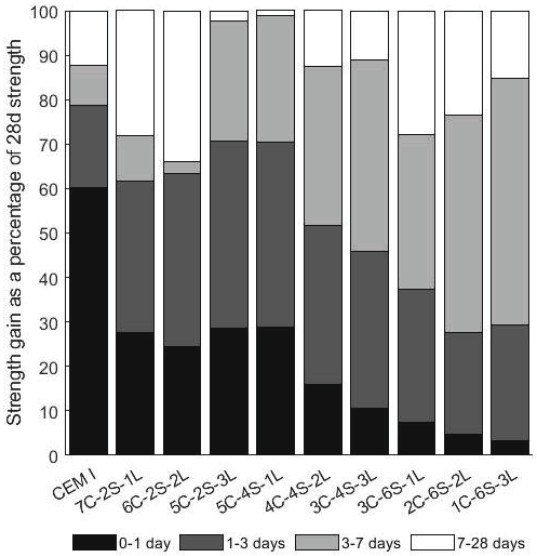

Figure 4. Experimentally determined strength development of CEM I and C-S-L binders up to 28 days

3.3. Minimising embodied carbon for a given application

For the majority of applications, the strength requirements are fixed and the limits on clinker replacement levels are governed by standards, such as EN 197-1 (British Standards Institution, 2019).

An example of eCO_2 minimisation is shown in Figure 5. Show as hatched lines, the constraints are: max. 35% GGBFS, max. 35% limestone, max. 35% total replacement, min. 40 MPa compressive strength at 28 days. for a Portland-composite cement of class CEM II/B-M (S-L). The dotted lines represent contours of kg eCO_2/t binder. The filled circle indicates the most efficient binder composition: 66% CEM I, 16% GGBFS and 18% limestone, with a total eCO_2 of 542 kg/t. This represents a saving of 257 kg/t versus CEM I – approximately 30%.

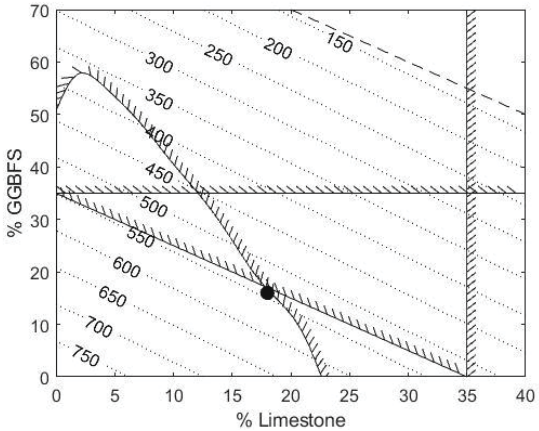

Figure 5. An example of eCO_2 optimisation for a CEM II/B-M (S-L), with a required strength of 40 MPa at 28 days

This result also indicates the restrictiveness of current standards. Currently, GGBFS and limestone can only be used together in a CEM II/B-M class binder at total clinker replacement levels of up to 35%. Individually, GGBFS and limestone can be

used in blastfurnace cements (CEM III/C) or Portland-limestone cements (CEM II/B-L) with replacement levels of up to 95% and 35% respectively. Whilst CEM III (in this case 49% CEM I, 51% GGBFS, 435 kg eCO_2/t) typically offers a more efficient binder, GGBFS availability is likely to be pose a significant problem. In the long term. GGBFS production is forecast to be less than 8% of the global demand for cement (Scrivener, John and Gartner, 2018). As such, spreading it further by incorporating high levels of other, more abundant, SCMs, such as limestone, is a priority.

Table 4 further explores this issue. The weakest binder fulfilling the 35% maximum replacement level is 65% CEM I and 35% limestone, with a compressive strength of 32 MPa. For any application with a lower strength requirement than this, the replacement level governs. For a requirement of 20 MPa, a mix of 10% CEM I, 65% GGBFS and 25% limestone could be used, with an eCO_2 of just 137 kg/t – a saving of 74%.

4. CONCLUSIONS AND FUTURE WORK

The use of supplementary cementitious materials has the potential to significantly reduce the emissions associated with the cement industry, however, optimisation of binder composition is key to maximising these savings. Whilst increasing GGBFS content is often the best way of improving the eCO_2 efficiency, material availability and economic factors make high limestone contents an attractive prospect. This is especially the case for low and medium strength applications, where standards, rather than strength requirements, often govern the maximum levels of clinker replacement.

The next stage of this work is to incorporate compressive strengths at other ages to allow the optimisation of binders for applications with both early- and late age strength requirements. By understanding which of these governs the embodied carbon, efforts can be made to alter construction schedules or undertake other steps to minimise extra unnecessary emissions.

It is only by extending this work to concretes that the true potential of C-S-L binders can be understood. Variables such as w/b ratio and aggregate content have a huge impact on the embodied carbon of concrete. It may be that binders calculated to be less efficient here could be used in smaller quantities to produces concretes with similar structural properties. The existing BRE method for the design of normal concrete mixes (Teychenné, Franklin and Erntroy, 1997) provides a way of estimating the structural behaviour of concretes from a reference mix. However, this method does not cover systems containing GGBFS or limestone, so experimental data will be gathered to make appropriate modifications.

REFERENCES

Adu-Amankwah, S. *et al.* (2017) 'Influence of limestone on the hydration of ternary slag cements', *Cement and Concrete Research*, 100, pp. 96–109.

Baumert, K. A., Herzog, T. and Pershing, J. (2005) 'Navigating the numbers: Greenhouse Gas Data and International Climate Policy'.

Bolte, G. *et al.* (2019) 'Development of composite cements characterized by low environmental footprint', *Journal of Cleaner Production*, 226, pp. 503–514.

British Standards Institution (2019) 'BS EN 197-1:2011'.

Draper, S. J. *et al.* (2021) 'Hydration of composite cements with low clinker contents', *Manuscript in preparation*.

Kulik, D. A. *et al.* (2013) 'GEM-Selektor geochemical modeling package: Revised algorithm and GEMS3K numerical kernel for coupled simulation codes', *Computational Geosciences*, 17(1), pp. 1–24.

Lothenbach, B. *et al.* (2008) 'Influence of limestone on the hydration of Portland cements', *Cement and Concrete Research*, 38, pp. 848–860.

Lothenbach, B. *et al.* (2019) 'Cemdata18: A chemical thermodynamic database for hydrated Portland cements and alkali-activated materials', *Cement and Concrete Research*, 115, pp. 472–506.

Scrivener, K. L., John, V. M. and Gartner, E. M. (2018) 'Eco-efficient cements: Potential economically viable solutions for a low-CO2 cement-based materials industry', *Cement and Concrete Research*.

Teychenné, D. C., Franklin, R. E. and Erntroy, H. C. (1997) 'Design of normal concrete mixes', *Building Research Establishment Ltd*, 331, p. 46.

The Cement Sustainability Initiative (2009) 'Cement industry energy and CO2 performance: getting the numbers right', *The Cement Sustainability Initiative*.

The Concrete Centre (2014) 'Specifying Sustainable Concrete', *Concrete Quarterly*, (248), pp. 26–31.

Thoenen, T. *et al.* (2014) 'The PSI/Nagra Chemical Thermodynamic Database 12/07 Nuclear Energy and Safety Research Department Laboratory for Waste Management (LES)', (14).

Thoenen, T. and Kulik, D. (2003) 'Nagra/PSI Chemical Thermodynamic Data Base 01/01 for the GEM-Selektor (V.2-PSI) Geochemical Modeling Code: Release 28-02-03', *Internal Report TM-44-03-04*, pp. 1–43.

Wagner, T. *et al.* (2012) 'Gem-selektor geochemical modeling package: TSolMod library and data interface for multicomponent phase models', *Canadian Mineralogist*, 50(5), pp. 1173–1195.

Zajac, M. *et al.* (2020) 'Late hydration kinetics: Indications from thermodynamic analysis of pore solution data', *Cement and Concrete Research*, 129.

Young Researchers' Forum V
Innovation in Construction Materials
22 April 2021

Exploration of a 3D Printed Geo-Polymer with Respect to Interlayer Bond Strength

A.W.Campbell
School of Engineering and the Built Environment, Edinburgh Napier University, Edinburgh, UK

ABSTRACT: 3D Printed Concrete (3DPC) is an advancing technology that utilises extrusion-based mortar in conjunction with a robotic gantry system to ascertain complex geometric structures without formwork. Due to the nature of the print, the structure is fabricated layer by layer with a substantial interval before the deposit of the new material. Therefore, the bond between interfaces becomes a matter of importance where, if not sufficiently bonded, the material will display anisotropic properties which subsequently weakens the tensile behavior of the print. Through rheological and tensile strength testing, it is possible to attain the materials' mechanical properties with respect to layer deposition intervals. This paper focuses on investigating the effect of time delay on direct tensile bond strength of a five layered print. The results verified the tensile strength of the specimen correlated with the delay in deposited layers.

1. INTRODUCTION

Current research papers offer alternative enhancement techniques such as: predefined keys within each layer to improve shear strength [1], an external paste deposited between interfaces for advanced adhesion [2] and in-situ mesh reinforcement to provide overall enhanced structural capacity [3]. However, with the positive increase in bonding strength, the process becomes more complex and expensive. Therefore, an internal investigation of the materials properties was undertaken.

1.1 *Background*

Al-Qutaifi et al. [4] classified the bond formation of the mortar into two sub-categories: chemical attraction that refers to the bonding and hydration with respect to the interfaces; mechanical bonding which is dependent on the physical characteristics of the printed material. Both must work coherently in order to achieve an optimal design mix, however, the process of achieving a functional system is complex. It must be noted that this information is regarded as intellectual property, resulting in little correlation from one design to another.

Tay et al. [5], who first explored the effect of interlayer time gap, understood that a non- linear decrease in bond strength is permitted due to the Calcium Silicate Hydrate (C-S-H) bond, resulting in porous interfaces. The study investigated the adhesion behavior between two layers with respect to time which was adequate in providing an appropriate understanding of the initial bond. However, in terms of an in-situ application, development of the mechanical and chemical interaction is required.

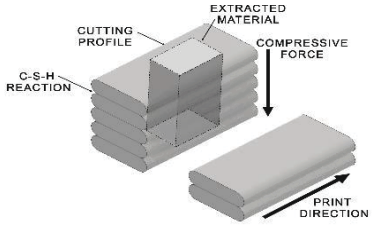

Figure 1- Stress increase through increased layers As the C-S-H nucleation increases, inducing hydration, a subsequent increase in stiffness is displayed within the initially deposited layer. The increase in material will incur stresses to the initial layer, ensuing an increase of stiffness which results in a modification within the overall bond strength of the printed material.

1.2 *Aims and Objectives*

This paper aims to provide a fully comprehensible methodology to test and analyse 3D printed structures through generating a testing regime that can be replicated for future researchers. The area of interest revolves around the printed layers interface bond strength in conjunction with supporting tests to fulfil a desirable material that achieves a high mechanical tolerance. A systematic approach of the build and complexity of the printing process will be evaluated through the objectives listed below.

1. Investigate layer time-gap of an extruded mortar and comment on its limitations. Interlayer bond strength is the chosen characteristic to define the testing of the varying specimens.
2. Refine a standardised printing and testing methodology for 3D printed material. Indorse parameter changes to enhance both buildability and workability properties.

2. METHODOLOGY AND MATERIALS

2.1 *Printing Application*

A mortar pump which operates by Archimedes screw principle was adopted with a double braided nylon hose to deliver the mortar to the print path. The extrusion nozzle was deigned on Autodesk Inventor, accounting for additional pressure from the low-viscosity material, and then printed using Polylactic Acid. Increasing nozzle stand-off distance had been considered to account for discrepancies within the mix, however, this is perceived as detrimental to the interlayer adhesion and therefore, the stand-off distance was set to zero [6].

Figure 2 – Customised 3D Printing System

Consideration was given towards the quantity of material within the pump hopper with respect to the mass required to ensure an adequate flow of material (0.2 m^2) and hose length (1 m). Additionally, to mimic a cartesian robot, a pulley system was designed which incorporated a Schenk 5500J universal testing machine to permit accurate travel speed in one direction. The mortar was deposited with five layers at a height of (150 mm), width (60 mm) and length (600 mm) on a non-adhesive surface and then left to cure for seven days. Furthermore, a thread and screw system were utilised to manually adjust the height of the nozzle head to permit favorable printing conditions.

2.2 *Tensile testing procedure*

A total of three printed specimens were analysed with respect to direct tensile strength and in line with the principles of BS EN 14488-4 [7]. (150 x 50 x 50) mm testing samples were extracted from each print and epoxy bonded to steel dollies with a surface area of 1963.5 m^2. Once tested within the Instron 3367 universal testing machine, visual inspections for failure location respective to layer interfaces was undertaken.

2.3 *Material Genetics*

The mix is required to fulfil a broad spectrum of criterium from workability for enabling efficient extrusion to adequate shape retention to permit optimal buildability. Conscious of this limitation, chemical admixtures were utilised:

Table 1- Geo-Polymer Design Mix

Cement	Sand/Binder Ratio	Water/Binder Ratio	Additives
CEM I 52.5 N	1.5	0.4	SP, VMA, R, PPF

SP- Superplasticiser, R - Retarder, VM - Viscosity Modifying Agent, PPF – Polypropylene Fibres

The design mix (Table 1) was analysed with respect to workability and setting time through adopting supporting testing. The chosen material permitted a slump value of 20mm and setting time equivalent to 110 minutes. In terms of buildability, a printed section with dimensions (50 x 30 x 12) mm could withstand 14.2 kg without visual deformation.

2.4 *Limitations*

The limitations within this study are predominantly associated with the physical printing apparatus regarding the extrusion rate and print speed. The PS2000 pump is responsible due to the inconsistency of the Archimedes screw with the following by- products affecting the overall printing process:

1. Archimedes principle demonstrated infrequent pumping behaviour which resulted in a manual increase in pressure to counter the possibility of breaks in the material.
2. As the system operated was governed by the intron machine, the print speed was limited to 5.83mm/s which created strain on supporting parameters.

The overall applicability of the system is adequate for creating a printed specimen that conforms to small lab testing, but scalability is foreseen to be an issue.

3. RESULTS AND DISCUSSION

3.1 *Direct Tensile Strength and Failure Modes*

From the experimental testing, it can be deduced that specimen 1A failed due to the lack of interface bonding strength between the first and second layer whilst 2B and 3A failed within the virgin material. Although the exact value of interlayer bond strength between layers was not determined within 2B and 3A, the value can be taken as superior and the overall specimen can be classified as homogenous.

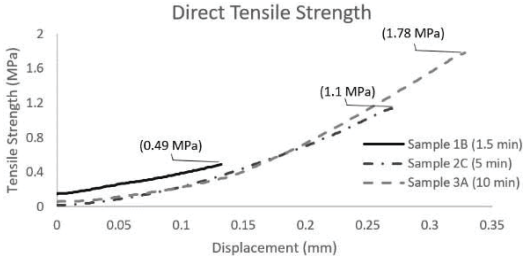

Figure 4. Direct Tensile Test of Specimen (1B, 2C, 3A)

Contrary to the results found by Tay et al. [5], where the bonding strength depreciated over time, experimental testing revealed that tensile strength increased with time gap.

Further examination reveals the stability of specimen 1 (5 min) with respect to failure location. All three samples split at the centre of the middle layer, reinforcing the homogenous properties of the print. However, each test exhibited irregular bonding strengths (0.81, 1.14, and 1.81 MPa) which is coherent with specimen 1. Specimen 3(10 min) displayed more concise results, agreeing with Panda et al. [6], where the increase in time-gap realised more definitive bonding characteristics.

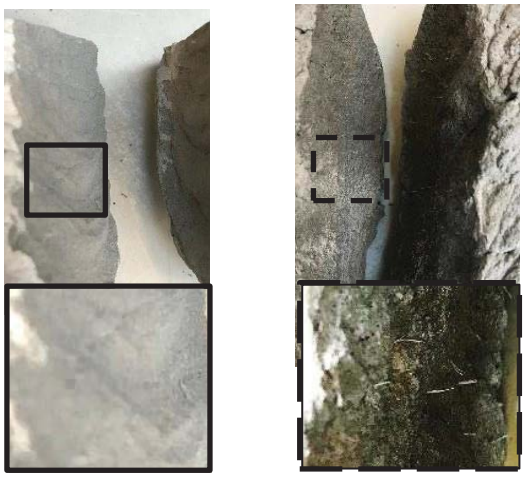

Figure 3. Fibre Content Within Layer Interfaces

From Figure 4 it is evident that specimen 2, on the right, has an increased number of Polypropylene Fibres (PPF) when compared to specimen 1. The orientation is of particular interest due to their ability to align vertically and interlock the interfaces. With the linear increase in compressive forces, due to the layering process, the fibres can flow outwards to a certain width of the lower layer and reduce the gravity effect [8]. However, the compressive forces fail to fully justify the difference in results. Additional research in this field is required to better understand the affecting parameters.

3.2 *Printing Limitations and Endorsement*

It is crucial to obtain a material that strikes the balance between adequate flowability and shape retention once extruded. In order to achieve this, a selection of parameters require analysis. Fundamental printing factors have been assessed with respect to controllability (Table 2). Five being the highest-ranking score in this case.

Table 2- Controllability Assessment

Printing Parameter	Controllability
Extrusion Rate	2
Stand-Off Distance	4
Print Path Speed	3
Material Dimensions	2
Material Properties	5
Print Time Intervals	4

As 'extrusion rate' and 'material properties' obtained the lowest and highest score respectively, a developed discussion will be undertaken within this section.

3.2.1 *Extrusion Rate (Rating-2)*
Although the pulley system was adequate in extruding a conclusive material, the print speed was restricted to 5.83 mm/s, which was considerably slower than aligning papers [1-3]. The restricted print path speed permitted, to an extent, strain on the extrusion rate which was subsequently reduced to compensate the former. With this in mind, an increase in pumping pressure was devised to counter the resistance from the internal hose surface which resulted in an alteration within the overall material dimensions. By reducing the head height from the pump output to the nozzle and decreasing the length of hose, the pressure could be adapted. The modification was successful in achieving lower pressures and a more succinct flow. However, due to the inconsistencies of the Archimedes screw, the originally hypothesized material dimensions were reconsidered.

3.2.2 *Material Properties (Rating-5)* Analysing the printing application highlighted the intricacy of balancing each parameter to attain a desired mix. Supporting testing, discussed within chapter 2.3, realised a fundamental understanding of the process at hand but complications arise once extruded. The hydrostatic pressure within the hose encouraged increased yield strength/stiffness of the mix which reduced the workability. Therefore, an increase in superplasticiser from 1-1.5% was adopted to reduce the attraction between particles, known as Van Der Waals forces, which repulses the water from adhering to the cement. With respect to the extrusion parameters, altering the material mix was much more comprehendible with little limitation noted

4. SUMMARY

Fundamental experiments were undertaken to examine the mechanical properties of a multi-layered mortar with the following findings were concluded:

1. The primary material in question exhibited homogenous properties with an increase in bond strength respective to delay in layer depositing time.
2. The contradictory nature of the tensile strength when compared to current papers is the by-product of vertically aligned PPF.
3. In order to ascertain a more succinct printing process, consideration must be given to an alternative pump (piston) and pulley system for increased print speed. This will ultimately improve buildability respective of time delay.

5. REFERENCES

[1] B. Zareiyan and B. Khoshnevis, "Effects of interlocking on interlayer adhesion and strength of structures in 3D printing of concrete," *Autom. Constr.*, vol. 83, no. November 2016, pp. 212–221, 2017.

[2] T. Marchment, J. Sanjayan, and M. Xia, "Method of enhancing interlayer bond strength in construction scale 3D printing with mortar by effective bond area amplification," *Mater. Des.*, vol. 169, p. 107684, 2019.

[3] T. Marchment and J. Sanjayan, "Mesh reinforcing method for 3D Concrete Printing," *Autom. Constr.*, vol. 109, no. August 2019, p. 102992, 2020.

[4] S. Al-Qutaifi, A. Nazari, and A. Bagheri, "Mechanical properties of layered geopolymer structures applicable in concrete 3D-printing," *Constr. Build. Mater.*, vol. 176, pp. 690–699, 2018.

[5] Y. W. D. Tay, G. H. A. Ting, Y. Qian, B. Panda, L. He, and M. J. Tan, "Time gap effect on bond strength of 3D-printed concrete," *Virtual Phys. Prototyp.*, vol. 14, no. 1, pp. 104–113, 2019.

[6] B. Panda, N. A. N. Mohamed, S. C. Paul, G. V. P. B. Singh, M. J. Tan, and B. Šavija, "The effect of material fresh properties and process parameters on buildability and interlayer adhesion of 3D printed concrete," *Materials (Basel).*, vol. 12, no. 13, 2019.

[7] Testing sprayed concrete —Part 4: Bond strength of cores by direct tension. BS EN 14488-4:2005+A1:2008

[8] F. Y. Li, L. Y. Li, Y. Dang, and P. F. Wu, "Study of the effect of fibre orientation on artificially directed steel fibre-reinforced concrete," *Adv. Mater. Sci. Eng.*, vol. 2018, 2018.

Young Researchers' Forum V
Innovation in Construction Materials
22 April 2021

Intelligent rubber bearings for bridge monitoring

A. Orfeo[1], E. Tubaldi[1], E. Koursari[2], Stuart Wallace[2], Transport Scotland[3]
[1]Department of Civil and Environmental Engineering, University of Strathclyde
[2]Amey Consulting
[3]Transport Scotland's Innovation Fund

ABSTRACT

Elastomeric bearings are widely used in bridges to support the superstructure and play an important role in the health and safety of bridges. The response of the bridge to permanent and variable loadings (e.g. traffic) is influenced by the bearing mechanical properties, and the state of deformation and stress of the bridge bearings reflects the performance of the bridge structure. The aim of this work is to illustrate the preliminary investigations carried out towards the development of smart elastomeric bearings that can be used as a low-cost sensing technology. An experimental campaign was performed on different testpieces made of a natural rubber compound filled with Printex in order to characterize the piezoresistive properties under different deformation conditions that are also found in real bearings. It is observed that relatively simple models can be used to describe the relationship between the change of the resistivity and the change in the state of deformation of the rubber testpieces. Some experimental tests are also carried out to show that the developed model can be used to predict the state of deformation under random loadings of different amplitudes that are characteristic of the passage of traffic over a bridge.

1. INTRODUCTION

Bridge bearings are the main connecting components between bridge superstructures and bridge substructures, accommodating the displacements associated with this movement. The response of the bridge to permanent and variable loadings (e.g. traffic) is influenced by the bearing mechanical properties, and the state of deformation and stress of the bridge bearings reflects the performance of the bridge structure. Therefore, bearing monitoring can play an important role in bridge safety assessment (Ko et al. 2005). Bridge bearing monitoring has been explored by several researchers (Liu et al. 2016) (Li, Ning, and Chen 2012). Such bridge bearing integrated with real time measurement instrumentation are also called Smart Bearings. The development of smart bearing by integrating it with innovative sensor has been object of several works (Schulz et al. 1998) (Seim et al. 1999).

The aim of this work is to illustrate the preliminary experimental investigations carried out towards the development of smart elastomeric bearings that can be used as a low-cost sensing technology. The idea behind the smart bearing development is that the piezo-resistive properties inherent to the filled natural rubber used in the laminated bearings commonly employed for supporting bridge decks can be exploited to turn them into low-cost sensors and weight-in-motion systems (i.e. to measure traffic loading and detect the passage of overweight vehicles).

The piezoresistivity of filled rubber has already been investigated in the past through numerous experimental studies (Busfield, Thomas, and Yamaguchi 2004) (Jha et al. 2010), demonstrating the significant change of electrical resistivity under the strains typically induced by external loads. It was shown that some compounds such as those using Printex X2 as filler exhibit superior properties compared to those using carbon black, but only for the case of tensile loadings. In this study, testpieces made of a rubber compound filled with Printex X2 are used to investigate the piezo-resistive properties under loadings that bridge bearings are more typically subject to, i.e., shear and compression loadings.

2. Experimental Setup

This section describes the filled rubber compound that was considered to develop the test-pieces and the electrical-mechanical testing apparatus used to assess the piezo-resistive behaviour of the filled rubber. Table 1 shows the formulation of the compound. Printex XE2 compound has been used to enhance the piezo-resistive properties of rubber and achieve a more reversible behaviour (i.e. similar electrical response upon mechanical loading and unloading) than the traditional compound used for elastomeric bearings such as carbon black.

Two different types of mechanical tests were performed, corresponding to different test-pieces and loading conditions, namely compressive and

shear. During each test, the changes of electrical resistance were measured.

Table 1. Formulation of the Printex rubber compound in weight (parts per hundred rubber)

Ingredients	Parts per hundred of rubber (PHR)
	Printex 12
NR (SMR CV60)	100
Printex XE2	12
Stearic acid	2
Zinc oxide	7
6PPD	1.5
Antilux 654	1.5
Manobond 740 C	0.75
TBBS	1.5
Sulphur	1.5

Double shear (DBS) specimens were used for the double shear tests. They consist of two cylindrical rubber discs moulded between three brass pieces. The thickness of the disc is 6mm and its diameter is 25mm (Figure 1: left). The compressive specimen consists of one cylindrical rubber layer 5 mm thick moulded between two brass pieces and its diameter is 50 mm (Figure 1: right).
The electrical resistivity of the testpieces was measured with a two-point contact method and the experimental set up is shown in Figure 2.

Figure 1. Left: DBS testpiece; Right: Compressive tespiece

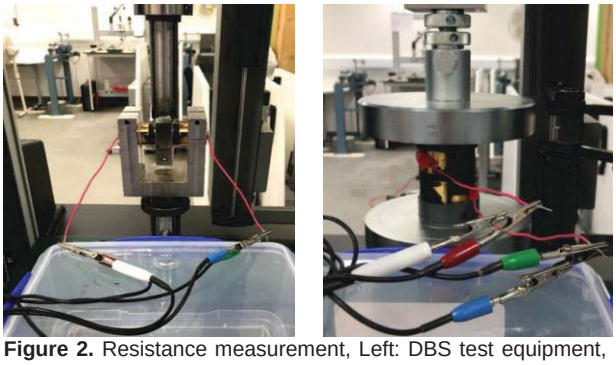

Figure 2. Resistance measurement, Left: DBS test equipment, Right: Compressive test equipment

Double shear and compression tests consisted in a minimum of two up to five identical cycles imposed to the virgin rubber piece. The first cycle was performed to consider the “stress- softening” effect. This effect takes place within the ‘virgin’ rubber during the first deformation paths, which are generally characterized by a higher stiffness and dissipative capacity (Tubaldi et al. 2017). This effect usually vanishes after two-three full cycles.

3. Resistivity measurement

Direct Current (DC) was imposed during mechanical testing to interrogate the system and the variation of the electrical resistance *R* was measured during the test by applying with Ohm’s law, i.e.,

$$R = \frac{V}{I} \tag{1}$$

where *V* and *I* denote respectively the potential difference and the current measured between the contact points. The electrical resistivity of the rubber is a property of the material not affected by the dimensions of the testpiece and can be calculated as follows:

$$\rho = RA/l_0 \tag{2}$$

where l_0 is the initial length of the sample. The evaluation of *A* depends on the loading state involved into the specimen. In fact, for compression tests *A* is the actual (i.e. deformed) cross-sectional area:

$$A = A_0 / \lambda \tag{3}$$

In Eqn. (3), A_0 is the initial cross-sectional area and λ is the axial shortening:

$$\lambda = \frac{l}{l_0} \tag{4}$$

where *l* is the compressed length.
In the case of double shear tests $A = A_0$.

4. Double shear tests

The double shear tests consisted in six cycles at six shear strain amplitudes γ_{max}, 5, 10, 20, 50, 70 amd 100%. A dwell time of 3 minutes was considered between each further application of strain to allow the rubber to fully relax. The electrical resistivity of the rubber is calculated with Eq. (2), where l_0 is the total thickness of the two rubber layers of the DBS test pieces. Figure 3 shows the electrical resistivity as a function of the strain during the loading and unloading part of the six cycles at each strain level. In general, the resistance increases with the shear deformation and exhibits an almost reversible behaviour, in agreement with the tests carried out by Jha et al. (2010) on tensile testpieces. However, the changes of resistivity are very low for low strain amplitudes, which indicates a low sensitivity of the devices.

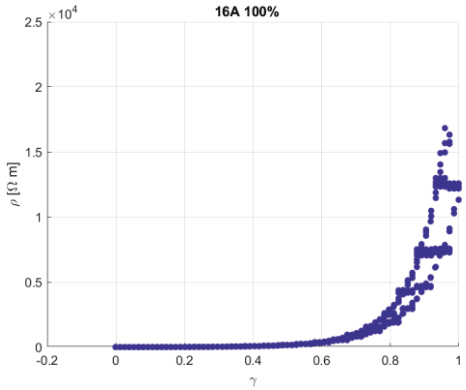

Figure 3. Resistivity as a function of strain during six cycles

Figure 4 shows the variation of the resistance normalized by the resistance at zero strain R_0, i.e. $\Delta R/R_0$, versus the strain γ. The observed data between 0 % and 60 % and between 60% and 100% of shear strain are interpolated using two quadratic functions with the aim of finding a model for relating the changes of resistivity to the changes of shear strain.

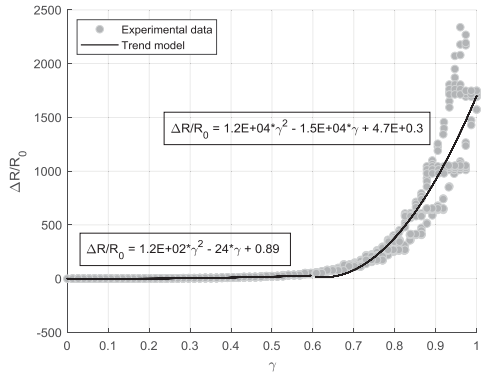

Figure 4. Variation of resistance versus shear strain

The regression model developed is used to infer the changes of strain based on the readings of the resistivity obtained in a subsequent test. This test was performed on the same sample by using a random input that can be assumed to be representative of the effect of the traffic passing over a bridge. Various amplitudes of deformation were considered for the various cycles, simulating the effect of the passage of vehicles of different weight. The purpose of this test is to understand whether by measuring the changes in electrical resistivity of the device it is possible to have an estimate of the strain history it is subjected to, or at least to infer the maximum strain amplitudes of the imposed cycles.

Figure 5 shows the time history of the experimental and predicted shear strains, which are in reasonable accord with each other. It is noteworthy that the proposed model cannot predict with good accuracy cycles with low deformation amplitudes due to the low sensitivity of $\Delta R/R_0$, versus the γ at small shear strains.

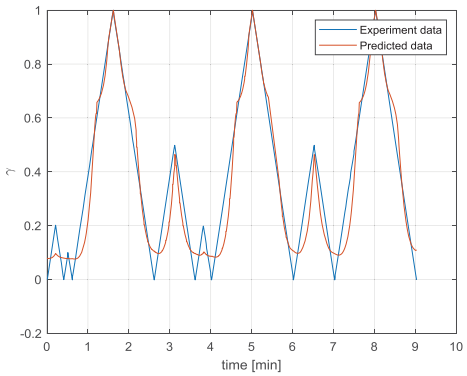

Figure 5. Comparison between experiment and predicted data: a) Variation of resistance versus strain, b) Strain versus time

5. Compression tests

Three cyclic uniaxial compressive tests were conducted on the cylindrical testpiece. The sample was compressed by 0.5mm steps up to the desired compression ratio λ = 0.6. A dwell time of 60s was considered between each further application of compression.

Taking the value of the resistance from λ = 0.9 to 1, it is possible to find a trend of $\Delta R/R_0$ versus the compression strain $\varepsilon = \lambda - 1$. Using a bilinear interpolation, the relations are shown in Figure 6:

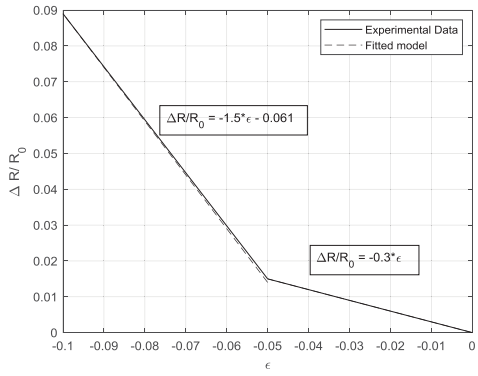

Figure 6 Variation of resistance ratio versus strain

A second test was performed on the same sample by imposing a input with various triangular waves, superimposed to a compression of 0.15 mm. Figure 7a shows the stress and electrical resistance behaviour due to the applied displacement pattern. It can be observed that the resistivity increases when the compression increases, and decreases when the compression decreases, showing again the reversible behaviour due to the Printex rubber compound. The relationship obtained from the previous tests for relating changes of resistivity to changes of compression can be used to check whether it is possible to infer the changes of strain in the compressed devices by measuring only the changes of electrical resistivity.

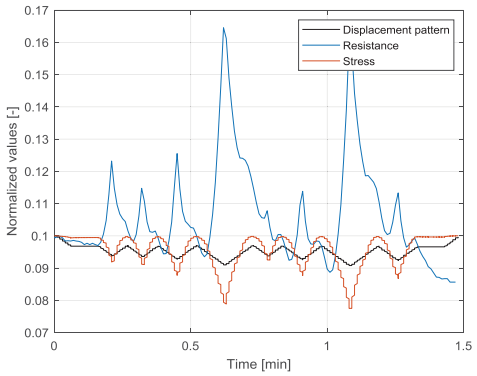

a)

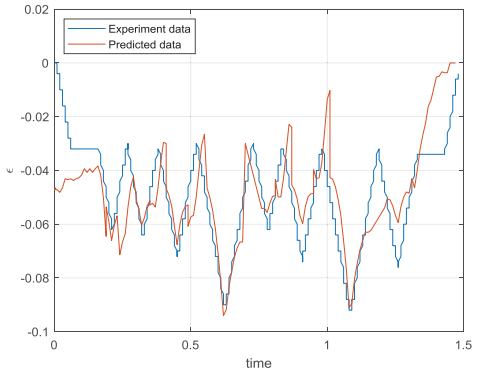

b)

Figure 7 a) Resistance response b) Strain versus time: comparison between experiment and predicted data

Figure 7b shows that the predicted data are in reasonable accord with the measured ones, thus confirming that the Printex-based rubber compound has a good potential to be used to develop intelligent rubber bearings that can be used for structural health monitoring purposes or as weight in motion system.

6. Conclusion

The experimental electro-mechanical tests carried out at University of Strathclyde have shown the potential of natural rubbers filled with Printex for the development of smart rubber bearings, thanks to their reversible piezo-resistive behaviour. It was shown that it is possible to develop simplified expressions for relating the change of resistivity to the changes of strain in the material and these expressions can be used to infer the state of strain in a rubber device based on simple electrical resistivity measurement. This is an essential requisite for the development of intelligent rubber bearings that can provide information about their state or can act as weight-in-motion system.

Smart rubber bearings could become an advantageous solution for bridge monitoring thanks to the low cost of the compounds and resistivity interrogation systems. Future studies will further investigate the development of smart bearings by carrying out more experimental tests to investigate the effect of environmental factors such as temperature and type of loading on the resistivity changes, as well as the use of alternative compounds or volume fractions of Printex.

Acknowledgment

This work was supported by Amey, through Transport Scotland's Innovation Fund 2019/20.

References

Busfield, J. J.C., A. G. Thomas, and K. Yamaguchi. 2004. "Electrical and Mechanical Behavior of Filled Elastomers 1: The Effect of Strain." *Journal of Polymer Science, Part B: Polymer Physics* 42(11 SPEC. ISS.): 2161–67.

Jha, V, A. G. Thomas, M Bennet, and J. J.C. Busfield. 2010. "Reversible Electrical Behavior with Strain for a Carbon Black-Filled Rubber." *Journal of Applied Polymer Science* 116(5): 2658–67.

Ko, J. M., and Y. Q. Ni. 2005. "Technology Developments in Structural Health Monitoring of Large-Scale Bridges." *Engineering Structures* 27(12 SPEC. ISS.): 1715–25.

Li, Sheng, Qiang Ning, and Hui Chen. 2012. "Rail Elevated Bridge Bearing Displacement Monitoring Based on FBG Sensor." *Applied Mechanics and Materials* 178–181: 2034–37.

Liu, Qiang et al. 2016. "An Intelligent Monitoring Method and Its Experiment for Bridge Bearing." (Iccte): 633–38.

Schulz, Whitten L., Eric Udd, John M. Seim, and Galen E. McGill. 1998. "Advanced Fiber Grating Strain Sensor Systems for Bridges, Structures, and Highways." *Smart Structures and Materials 1998: Smart Systems for Bridges, Structures, and Highways* 3325(March 2014): 212–21.

Seim, John M., Eric Udd, Whitten L. Schulz, and Harold M. Laylor. 1999. "Health Monitoring of an Oregon Historical Bridge with Fiber Grating Strain Sensors." *Smart Structures and Materials 1999: Smart Systems for Bridges, Structures, and Highways* 3671(May 1999): 128–34.

Tubaldi, Enrico et al. 2017. "Stress Softening Behaviour of HDNR Bearings: Modelling and Influence on the Seismic Response of Isolated Structures Enrico." *Earthquake Engineering & Structural Dynamics* 41(11): 1549–68. http://onlinelibrary.wiley.com/doi/10.1002/eqe.2230/full.

Young Researchers' Forum V
Innovation in Construction Materials
22 April 2021

Manufacturing free-form inflated thin-walled steel structural members

S. Jowhari Moghadam, S. Cavalaro and R.B. Cruise
Department of Architecture, Building and Civil Engineering, Loughborough University

ABSTRACT

Free-Form Inflation (FFI) is a novel cold-forming process that uses low-pressure compressed air (0.2-0.5 MPa) to create three-dimensional objects. An application of this forming process can be to produce thin-walled steel structural members. Thin-walled steel members are conventionally manufactured through cold roll-forming which is an energy-intensive process that uses expensive and high-maintenance rollers. The tool-free Free-Form Inflation process offers potential reduction in energy and material consumption. Producing structural members through inflation poses limitations on the generated shapes while offering the freedom of customizing geometries without having to change the entire process. The application of the FFI process in construction has not been fully explored due to the inherent complexity of predicting the resulting geometry of the members and thus their structural behaviour. This paper will present the first developed numerical model that simulates the inflation stage of the FFI process to achieve predictability of the inflated member shape.

1. INTRODUCTION

With the rapid urbanisation and the growing need for buildings and infrastructure, carbon emissions must be dramatically reduced to mitigate climate change. According to the World Steel Association, steel production is estimated to be responsible for 7-9% of global warming emissions. The construction industry accounts for more than 50% of the world steel demand (World Steel Association, 2020). The current major route for producing thin-walled steel members in large quantities is roll-forming. This process requires considerable energy to force cold sheet metal through expensive and high-maintenance rollers, which need replacing approximately every 10 years. Roll-forming allows for accurate control of the production of standardised shapes which aligns with the rationalisation of the structural steel industry and is accounted for in structural design guidelines. As a result, the cross-sections are limited in shape and typically unvarying along the member's length. Fabricating customised members as a way of minimising material usage (Sustainability, 2021) may be more costly and may consume more energy than standard rolled sections.

In search for alternative routes for producing thin-walled steel structural members with less energy demanding resources in terms of facilities, one option is a novel manufacturing process that uses low pressure compressed air to form three-dimensional (3D) objects. The process is termed Free-Form Inflation, since the resulting form of the inflated component is not directly constrained by any kind of forming tool, unlike conventional section forming. The lightweight FFI members use low forming pressure (0.2-0.5 MPa) and can be transported uninflated and be inflated on site. Despite the limits posed by the inflation method on the geometric variations that can be generated, the FFI process, unlike roll-forming, offers the freedom to customize shapes without the need to change the production process. A major challenge associated with the application of the FFI process in construction is the inherent complexity of predicting the resulting inflated geometry of the members and thus their structural behaviour. This study focuses on the use of numerical simulation to accurately predict the deformed geometry of the FFI members.

2. LITERATURE REVIEW

The earliest found reference to a process similar to FFI was in 1967. In 1967, Rawlings (Rawlings, 1967) proposed a new metal forming method, the so-called metal inflation technique, which uses air instead of liquid to inflate sealed flat sheets up to a desired pressure or up to a required volume. The inflation process transforms the metal sheets into a three-dimensional (3D) object. Rawlings' pioneer work on metal inflation only involved models created out of tin plates that were soldered together and was intended for structures (farm storage and vessels) or structural components (double-walled roof structure) which are not produced in quantity.

Where ductile metals were formed with liquid, the process was termed Die-Less Hydroforming (DHF)

method or hydraulic expansion, which forms metals by pressurised liquid without the use of dies. In the basic DHF process, the sheets are first cut into an initial geometry which is defined by the desired final shape. Two or more profiles are then welded around their periphery in a fluid-tight manner. One or several holes are created on one of the sheets through which the fluid will be inserted, allowing the workpiece to form freely (Hummel and Ngaile, 2014).

Except for reducing the tooling cost required for a hydroforming setup, DLH also offers an unprecedented ability to produce custom, complex geometries that are not possible to create through other forming methods (Hummel and Ngaile, 2014). Several studies have reported the application of Die-Less Hydroforming in fabricating large pressure vessels (Zhang and Wang, 2015), joining materials (e.g. camshafts and light-weight frame-structures) (Salamati, Soltanpour, Fazli and Zajkani, 2018), car safety system (Mercedes Benz, 2021); and the use of metal inflation in the realm of architecture and design (ZIETA, 2021; Franz Bahr, 2021; fullblOwn, 2021).

The potential of the metal inflation process for producing structural members was first manifested in the set of loadbearing construction elements that made up a 6-metre-long steel footbridge, as shown in Figure 1 (Terstiege, 2012). The bridge was built using the DLH process variant, known as the FiDU (Freie Innen Druck Umformung) or free internal pressure deformation, developed by Oskar Zieta (Terstiege, 2012). In the FiDU bridge that exhibited a weight-to-loadbearing ratio of 1:10, the uninflated geometries were fabricated from 1 mm-thick steel sheets that were laser cut and laser welded.

Figure 1. FiDU bridge by Oskar Zieta (ZIETA, 2021).

Metzger et al. (Metzger and Ummenhofer, 2018) aim to use DLH to create customised and loadbearing tubular members for applications in architecture and civil engineering. To produce tubular members, the researchers first release the internal pressure of the Die-Less Hydroformed object and cut off both ends of the member. Figure 2 shows the 'Hybridstutze PERFECTO' column where Metzger et al.'s DLH member forms the outer shell of the cigar-shaped column (Metzger and Ummenhofer, 2019).

Figure 2. Hybridstutze PERFECTO by Metzger et al (Metzger and Ummenhofer, 2019).

Free-Form Inflation process was developed for a focused application of FiDU technology to manufacture thin-walled steel structural members. The major challenge in harnessing the potentials of this process is that the only controls on the section shapes created by Free-Form Inflation are indirect and necessitate a technique for gaining predictability of the resulting geometry, internal stresses and material properties, all of which can be altered during inflation.

3. NUMERICAL SIMULATION OF THE INFLATION PROCESS

A 3D numerical model was developed to achieve predictability of the resulting geometry and structural performance of the FFI members. Numerical simulations help avoid additional prototyping which is both time intensive and costly. To solve the nonlinear inflation problem, Abaqus software (Dassault System, Simulia Corp, USA) was used.

3.1. Finite Element model of the inflation process

The parameters that determine the inflated shape of the FFI member are: the choice of initial uninflated geometry, steel sheet thickness, the material properties of the steel sheet and the applied air pressure. The Finite Element (FE) model that is presented in this paper was developed based on one of the FFI section prototypes to allow validation of the model. The prediction of the post-inflation material behaviour requires detailed consideration of the stress distribution across the entire FFI member. A 3D analysis approach was adopted, to obtain a realistic representation of the overall deformation of the FFI member, as shown in Figure 3. Linear 4-sided shell element (S4R in Abaqus) were used to model the member.

Figure 3. 3D Finite Element model of the FFI section prototype.

The elasto-plastic stress-strain curve of mild steel considering an isotropic hardening was obtained from tensile coupon test data. To simulate the welded interface between the two sheet profiles, a tie constraint was used which prevents any relative motion between the two profiles. Manual welding of the metal resulted in an uneven penetration depth of the weld around the FFI section prototype. To best represent this variation, the tie constraint was initially applied at different distances within the mentioned range until the best match for the experimental deformed geometry was obtained. The air pressure was modelled as a uniform surface load. In Free-Form Inflation, compressed air is applied sufficiently slow for the inertial effects to be neglected and can thus be considered as a quasi-static loading. For analysing this problem, an implicit analysis was selected as it offers unconditionally stable solutions and facilitates large time steps.

3.2. Prototype and geometric data acquisition

Figure 4 shows the FFI section prototype used in this investigation that was fabricated using a 0.8 mm-thick mild steel sheet. Two similar profiles were cut from the metal sheets and a circular through hole (2 mm diameter) was created onto one of the profiles, as a gas entry point. The paired profiles were subsequently manually welded together in an airtight manner and a nozzle was soldered onto the hole. By connecting the nozzle to an air regulator, pressurised air was gradually introduced between the two sheet profiles up to the desired pressure (p = 0.517 MPa). Once the members attained their resulting shape, the air was released, and the nozzle was detached.

Figure 4 Free-Form Inflated section prototype, before and after inflation.

The inflated shape of the FFI member was captured by a 3D laser scanner. Because of the shiny, uneven surface of the FFI test sample, particularly at the weld, some homogeneous reflections were likely suppressed, leading to possible measurement errors. Figure 5 shows the resulting point cloud.

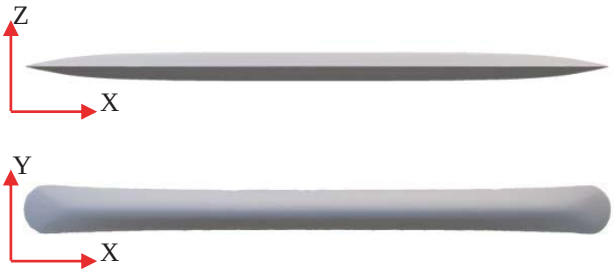

Figure 5. 3D scan data of the numerically simulated Free-Form Inflated section prototype, post-inflation.

A comparison between the laser scan data and the FE model results showed that the developed numerical model can predict the inflated shape of the FFI member with a mean absolute error of 0.01%. The low value is indicative of the 3D model's high accuracy.

4. CONCLUSIONS AND FUTURE WORK

In this paper, a novel process, the Free-Form Inflation, for manufacturing thin-walled steel structural members is introduced whose main obstacle is the difficulty in predicting the member's inflated shape and resulting structural behaviour. A 3D Finite Element model of the inflation process is presented which can estimate the resulting geometry of the member within 0.01% accuracy. The model provides valuable insight into the behaviour of the FFI members under inflation. Future studies seek to validate the occurring stresses and to explore how the deformations give the FFI members their permanent shape. The following FE models will consider the variations in the material and geometric properties that are introduced in the material throughout the production process; and a parametric study will be performed to analyse the significance of the process parameters that control the shape.

References

Worldsteel.org. 2020. worldsteel | World Steel Asoctiation. [online] Available at: <https://www.worldsteel.org/>.

www.steelconstruction.info. 2021. Sustainability. [online] Available at: <https://www.steelconstruction.info/Sustainability>.

Rawlings, B., 1967. Inflated Ductile Metal Structures. Architectural Science Review, 10(2), pp.44-48.

Hummel, S. and Ngaile, G., 2014. Die-less hydroforming of multi-lobe tubular structures. Proceedings of the Institution of

Mechanical Engineers, Part B: Journal of Engineering Manufacture, 229(3), pp.435-452.

Zhang, Q. and Wang, Z., 2015. Shape improvement of a dieless hydro-bulged sphere made of hexagonal and pentagonal shaped panels. Journal of Materials Processing Technology, 220, pp.87-95.

Salamati, M., Soltanpour, M., Fazli, A. and Zajkani, A., 2018. Processing and tooling considerations in joining by forming technologies; part A—mechanical joining. The International Journal of Advanced Manufacturing Technology, 101(1-4), pp.261-315.

Mercedes-Benz Passion Blog / Mercedes Benz, smart, Maybach, AMG & EQ. 2021. Das Sicherheitsexperimentalfahrzeug ESF 2009 - Mercedes-Benz Passion Blog / Mercedes Benz, smart, Maybach, AMG & EQ. [online] Available at: <https://blog.mercedes-benz-passion.com/2009/06/das-sicherheitsexperimentalfahrzeug-esf-2009/>.

ZIETA. 2021. Zieta Studio | Art & Furniture by Oskar Zieta | ZIETA. [online] Available at: <https://www.zieta.pl>.

Franz Bahr. 2021. Franz Bahr pneumatic sculptures Metallbildhauer Künstler. [online] Available at: <https://www.franz-bahr.com/>.

fullblOwn. 2021. fullblOwn. [online] Available at: <https://fullblown.co.uk/>.

Terstiege, G., 2012. The making of design. Basel: Birkhäuser.

Metzger, A. and Ummenhofer, T., 2018. Explicit and Implicit Simulations for Die-Less-Hydroforming- Structures including Welding , Forming and Load Capacity. Available at: <https://www.dynalook.com/conferences/15th-international-ls-dyna-conference/metal-forming/explicit-and-implicit-simulations-for-die-less-hydroforming-structures-including-welding-forming-and-load-capacity-using-ls-dyna-r-and-dynaweld-r/@@download/file/23-C>.

Metzger, A. and Ummenhofer, T., 2019. The use of LS-DYNA for the development of a topology-optimized thin-walled shell structure manufactured by Die-Less-Hydroforming. Available at: <https://www.dynalook.com/conferences/12th-european-ls-dyna-conference-2019/forming/metzger_kit.pdf/@@download/file/Metzger_KIT.pdf>.

Young Researchers' Forum V
Innovation in Construction Materials
22 April 2021

NUMERICAL SIMULATIONS OF DISPROPORTIONATE COLLAPSES OF TALL CLT BUILDING UNDER FIRE CONDITIONS

Xuan Zhao, Binsheng Zhang, Tony Kilpatrick and Iain Sanderson
Department of Civil Engineering and Environmental Management, School of Computing, Engineering and Built Environment, Glasgow Caledonian University, Glasgow G4 0BA, Scotland, UK

ABSTRACT

As one of the oldest known materials which are used in construction, timber is widely used all over the world. Timber can decrease CO_2 and help release more O_2. Timber material is more environmentally friendly when compared with the concrete, steel and masonry materials. More and more modern tall timber buildings have been designed and built in the world. Although there are no specific design codes or guides for tall timer buildings under fire conditions, they could still be designed and constructed based on the current Eurocodes and other design guides, together with the performance-based design approach, innovative construction technology and engineered timber products. This research is to explore the feasibility of designing a 30-storey tall timber building using CLT only through commercial finite element software SAP2000 combined with the reduced cross-section method under fire conditions. For numerically exploring structural performances of a 30-storey tall timber building under fire conditions, one case of disproportionate collapses of the tall CLT building subjected to a standard fire for up to 120 min is simulated by removing a CLT floor slab in Storey 17.

1. INTRODUCTION

Cross-laminated timber (CLT) is an engineered timber and consists of layers of wood panels with each layer laid at the right angle to the adjacent layer and glued together on their face with a structural adhesive. Therefore, the cross-section of a CLT element must have at least three layers placed in orthogonally alternating orientation to the neighbouring layers (Mestek and Winter, 2008). Laguarda Mallo and Espinoza (2014) specified that the environmental benefits of CLT had been widely documented by several researchers. Espinoza et al. (2016) also published status and research needs about CLT in Europe. They mentioned that compared with steel, brick, glass, plastic and concrete, CLT performs well under environmental conditions.

With the development of construction technology for timber buildings, the height of timber buildings also increases. The second tallest timber building in the world is the 24-storey HoHo Tower in Vienna, Austria, with a total height of 84 meters. Right now, the tallest timber building is the 18-storey Mjøsa Tower in Brumunddal, Norway, with a total height of 85.4 meters.

Recently published technical reports confirm that well-designed timber buildings are safe enough to withstand at normal temperature and under fire conditions. However, the researches on the vertical fire spread, collapse prevention under fire and burnout design for tall timber buildings are all limited though they are desperately needed. Also, mechanical analyses and numerical simulations on the structural performance of various types of engineered timber elements and complete tall timber building systems at different fire stages have been rarely reported. The detailed information about disproportionate failures of tall timber buildings at room temperature and under fire conditions is still limited. In this research, comprehensive numerical simulations are to be conducted on disproportionate collapses of a tall CLT building subjected to a standard fire for up to 120 min and one case is presented here by removing a CLT floor slab after the fire damage.

2. PLAN OF THE TALL CLT BUILDING

In this research, one mock tall CLT building is to be modelled and analysed. It is designed as a 30-storey office building. The plan dimension of the floor is 39 m × 34 m. Total height of the building is 105 m with the storey height of 3.5 m. The loadings on the floor in design are 0.92 kN/m^2 for dead load and 3.3 kN/m^2 for imposed load. The other loadings applied onto the buildings are in accordance to BS EN 1991-1-1 (BSI, 2002a) and the corresponding UK NA (BSI, 2002b). The strength grade of the timber material used is C24 accordance with BS EN 338 (BSI, 2016). This tall CLT building is assumed to be located in Glasgow, Scotland, UK. Cross-laminated timber members is

to be numerically simplified as thin shell elements based on the estimated method (Yasumura et al., 2016; Mato et al., 2016) and CLT Handbook (Gagnon and Pirvu, 2011). Commercial finite element software SAP2000 (CSI, 2016) is used for numerical simulations.

The tall CLT building contains a CLT core, CLT walls and CLT floors. The detailed floor planning is shown in Figure 1. The red rectangular box indicates Wall 1 which is the 360 mm thick 9-layer CLT inner core for lifts and stairs. The blue line on the red box indicates that there are no huge openings on the core wall. The grey lines indicate the CLT walls for the building, with Walls 2 as those 360 mm thick 9-layer walls for Storeys 1 to 15 and Walls 3 as those 280 mm thick 7-layer walls further above. All floor slabs for this tall CLT building are constructed from the 245 mm thick 7-player CLT panels. Most wall elements have minimum openings of 1.0 m × 2.5 m for doors or windows except part of the core indicated by the blue lines. If the wall widths are 5 m, 4.5 m and 4.0 m, the sizes of the wall openings will be 2.0 m × 2.5 m, 1.5 m × 2.5 m and 1.0 m × 2.5 m, respectively.

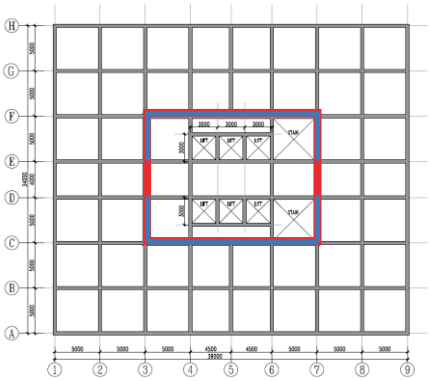

Figure 1. Plan view of the 30-storey mock tall CLT building.

3. DISPROPORTIONATE COLLAPSES OF THE TALL CLT BUILDING

For numerically exploring the structural behaviour of the tall CLT building after the disproportionate failure subjected to a 120-min standard fire, one case for disproportionate collapses of the building is simulated by removing a CLT floor slab. The selected slab is assumed to sustain a two-side fire which happens in the rooms above and below the indicated slab in Storeys 16 and 17, as shown in Figure 2. Points 1, 2, 3 and 4 are the node points at the four corners of the selected slab. The left part of the figure is the original building model before removing the selected CLT floor Slab BC23 after a 120-min standard fire. In contrast, the right part of the figure is the building model after removing the selected CLT floor Slab BC23 after the 120-min standard fire. The compared differences include the horizontal displacements at the selected node points, the principal stresses on the CLT floor slab below the removed slab, the principal stresses on the CLT walls for the selected room in Storey 15, etc.

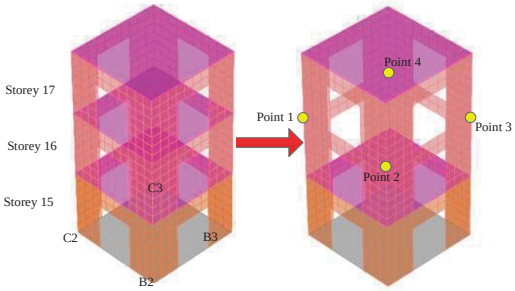

Figure 2. Removing CLT floor Slab BC23 at the top of Storey 16 in the tall CLT building after the 120-min standard fire

All the horizontal displacements in x- and y-directions at the four selected node points are listed in Table 1, together with the corresponding differences. The larger displacements in y-direction are purely due to the applied wind load in that direction. It can be seen that the removal of CLT Floor Slab BC23 at the top of Storey 16 after a 120-min standard fire will not cause changes in the horizontal displacements for the tall CLT building. In the following tables, “before” is short for “before removing a CLT floor flab” and “after” is short for “after removing a CLT floor slab”, and “difference” indicates the “difference (after vs before)”.

Table 1. Displacements at the selected corner node points at the top of Storey 16 before and after removing CLT Floor Slab BC23 once subjected to a 120-min standard fire (mm)

Models	Direction	Node 1	Node 2	Node 3	Node 4
Before	x	-0.087	-0.208	-0.192	-0.071
	y	-7.797	-7.821	-7.941	-7.922
After	x	-0.090	-0.210	-0.190	-0.070
	y	-7.795	-7.823	-7.943	-7.921
Difference	x	-0.003	-0.002	0.002	0.001
	y	0.002	-0.002	-0.002	0.001

Next, the principal tensile and compressive stresses in the S11 and S22 directions on the bottom surface of the CLT Floor Slab BC23 at the top of Storey 15 before and after removing the fire-damaged CLT Floor Slab BC23 at the top of Storey 16 are analysed. The contours of the principal stress S11 on the bottom floor surface at the top of Storey 15 subjected to the 120-min two-side fire are illustrated in Figures 3(a) and (b), with the corresponding contours of the principal stress S22 shown in Figures 3(c) and (d). The positions of node points chosen for further analysis are shown in Figure 4.

The values of the principal compressive stress S11 for the two building models with and without the selected fire-damaged CLT floor slab at the top of Storey 16 are fully based on the average stress values at node points 1, 2, 3, 4, 5 and 6, while the values of the principal tensile stress S11 are only based on those at node point 7. The values of the corresponding principal compressive stress S22 for the two building models with and without the

selected fire-damaged CLT floor Slab BC23 at the top of Storey 16 are fully based on the average stress values at node points 8, 9, 10, 11, 12 and 13, while the values of the principal tensile stress S22 are also only based on those at node point 7. The detailed values are listed in Table 2.

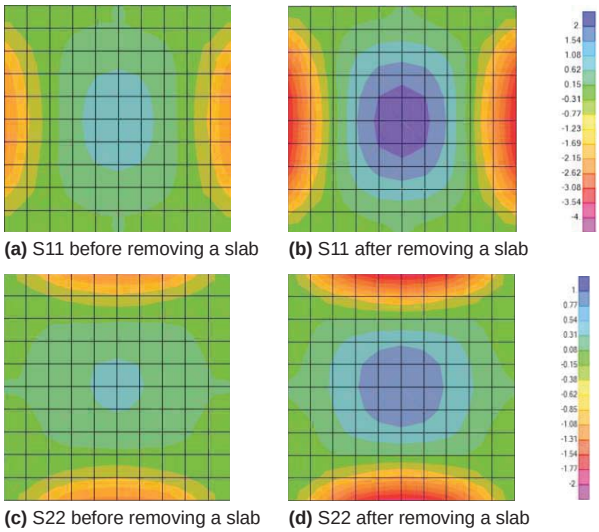

(a) S11 before removing a slab **(b)** S11 after removing a slab

(c) S22 before removing a slab **(d)** S22 after removing a slab

Figure 3. Contours of the principal stresses on the bottom surface of the selected CLT floor slab at the top of Storey 15 before and after removing CLT Floor Slab BC23 from the building model once subjected to a 120-min two-side standard fire.

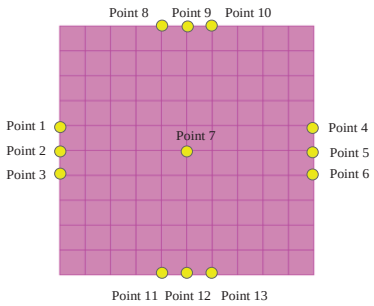

Figure 4. Thirteen selected node points on the CLT floor Slab BC23 for further analysis.

Table 2. Principal stresses on the bottom floor surface at the top of Storey 15 before and after removing CLT Floor Slab BC23 above once subjected a 120-min standard fire (N/mm^2)

Models	Compressive stresses	Tension stresses
S11 before	-2.699	1.339
S11 after	-5.311	2.810
Stress ratio	1.968	2.099
S22 before	-3.367	1.237
S22 after	-6.793	2.609
Stress ratio	2.018	2.109

The analysis on the principal stresses on the bottom surface of the selected CLT floor Slab BC23 at the top of Storey 15 indicates that there is no other significant effect on these stresses after removing a main CLT floor slab at the top of Storey 16 after sustaining a 120-min standard fire except the approximately doubled stresses on the selected floor slab due to the doubled floor loading by removing the CLT floor slab above.

Besides the stresses on the fire damaged CLT floor slab, the deformation at the centre of the same CLT floor Slab BC23 at the top of Storey 15 also need to be analysed. The relative deformation of the indicated slab is utilised for analysis and obtained by subtracting the average deformation of those at four corner node points from the deformation at the floor centre node point. Before removing the CLT floor slab, the maximum deformation at the floor centre node point is 2.161 mm. After removing the CLT floor slab, the maximum deformation increases to 4.885 mm. The deformation at the top of Storey 15 after removing the fire damaged floor slab increases by 2.724 mm or 126.1%, indicating that the raised deformation due to removing the indicated fire damaged floor slab is within the engineering expectation.

Besides the principal stress developments and the floor centre deformation, the loading conditions on the wall elements also need to be examined. Because the complete building model for the tall CLT building does not lose any loadings, it is expected that the stresses on the CLT walls in Storey 15 should not sustain big changes before and after removing the CLT Floor Slab BC23 at the top of Storey 16 once subjected the 120-min standard fire. The selected CLT wall for further analysis after the removal of the CLT Floor Slab BC23 after the 120-min standard fire on both sides is Wall B23, i.e. the wall on Axis B and between Axes 2 and 3 in Storey 15, see Figure 2. The contours of the horizontal principal stress S11 on the fire-facing surface of the selected Wall B23 in Storey 15 are illustrated in Figures 5(a) and (b), with the corresponding contours of the vertical principal stress S22 shown in Figures 5(c) and (d). It can be seen that the stress contours for S11 and S22 before and after removing the CLT floor Slab BC23 at the top of Storey 16 are very similar in shapes, patterns and even values. The locations of 22 selected node points for further analysis are shown in Figure 6.

The values of the principal compressive stress S11 for Wall B23 in Storey 15 with and without the selected fire-damaged CLT floor slab at the top of Storey 16 are fully based on the average stress values at node points 1, 2, 20 and 21, while the values of the principal tensile stress S11 are based on those at node points 10, 11 and 12. The values of the vertical principal compressive stress S22 for the Wall B23 in Storey 15 with and without the selected fire-damaged CLT Floor Slab BC23 at the top of Storey 16 are fully based on the average stress values at node points 7, 8, 14 and 15, while the values of the principal tensile stress S22 are based on those at node points 10 and 12. All the results are listed in Table 3.

It can be seen that the horizontal principal compressive and tensile stresses on the selected CLT Wall B23 in Storey 15 in the S11 direction and

the corresponding vertical principal tensile stresses in the S22 direction are not very large and do not vary significantly after removing the floor slab at the top of Storey 16 and adding the floor loading originally applied on the removed slab above onto the floor slab in Storey 15. Also, the ratio of the crucial vertical compressive stresses before to after removing a CLT floor slab is only 1.02, almost no change.

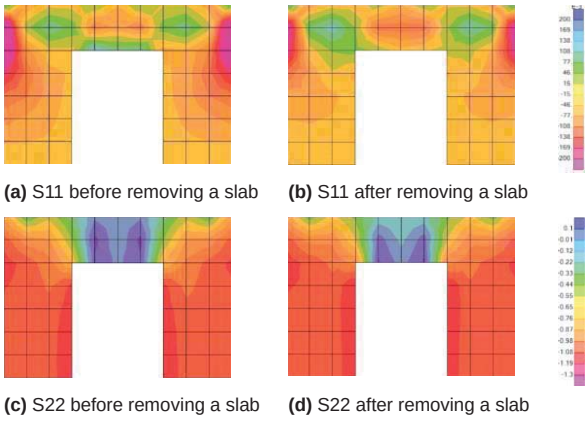

(a) S11 before removing a slab **(b)** S11 after removing a slab

(c) S22 before removing a slab **(d)** S22 after removing a slab

Figure 5. Contours of the principal stresses on the fire-facing surface of the selected Wall B23 in Storey 15 before and after removing the CLT floor Slab BC23 at the top of Storey 16 from the building model once subjected to the 120-min standard fire.

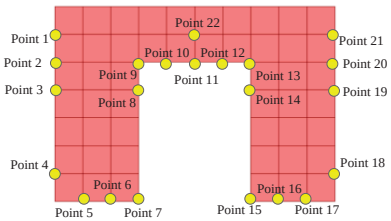

Figure 6 Twenty-two selected node points on the CLT Wall 2 for analysis

Table 3. Principal stresses on the fire-facing surface of the selected Wall B23 in Storey 15 before and after removing CLT Floor Slab BC23 at the top of Storey 16 once subjected the 120-min standard fire (N/mm^2)

Models	Compressive stresses	Tensile stresses
S11 before	-0.718	0.251
S11 after	-0.535	0.033
Stress ratio	0.745	0.131
S22 before	-2.034	0.145
S22 after	-2.075	0.202
Stress ratio	1.020	1.393

4. CONCLUSIONS

In this research, a 105 m high 30-storey tall CLT building has been numerically simulated under fire conditions using commercial finite element software SAP2000 and the results have been analysed, including the developments of the floor centre displacement and principal stresses of various adjacent CLT members due to disproportionate collapses after the failure and removal of a seriously fire damaged CLT floor slab from this building.

The above numerical analyses on the horizontal displacements at the node points at the corners of the selected floor slab and the principal stresses on the selected CLT floor slab and wall indicate that the failure and removal of a fire-damaged CLT floor slab will not cause huge effects on the global structural safety, stiffness and stability of the tall CLT Building.

Also, the crucial compressive stresses on the selected wall do not vary significantly when removing a CLT floor slab in the storey above, which means that the original design of the selected wall should be safe under the current fire situations.

Acknowledgement

This project is supported by the School of Computing, Engineering and Built Environment at Glasgow Caledonian University, Scotland, UK.

References

British Standards Institution (BSI), 2002a. BS EN 1991-1-1:2002 Eurocode 1: Actions on Structures – Part 1-1: General Actions – Densities, Self-weight, Imposed Loads for Buildings. London, UK.

British Standards Institution (BSI), 2002b. NA to BS EN 1991-1-1:2002 UK National Annex to Eurocode 1: Actions on Structures – Part 1-1: General Actions – Densities, Self-weight, Imposed Loads for Buildings. London, UK.

British Standards Institution (BSI), 2016. BS EN 338: Structural Timber – Strength Class. London, UK.

Computers and Structures, Inc. (CSI), 2016. SAP2000 Version 18.2. Berkeley, CA, USA.

Espinoza, O., Rodriguez Trujillo, V., Laguarda Mallo, M.F. and Buehlmann, U., 2016. Cross-laminated timber: status and research needs in Europe. BioResources, 11(1), 281-295.

Gagnon, S. and Pirvu, C., 2011. CLT Handbook: Cross-Laminated Timber, Canadian Edition, FPInnovations, Québec, Canada.

Laguarda Mallo, M.F. and Espinoza, O., 2014. Outlook for cross-laminated timber in the United States. BioResources, 9(4), 7427-7443.

Mestek, P. and Winter, S., 2008. Design of cross laminated timber (CLT). Proceedings of The 10th World Conference on Timber Engineering, Miyazaki, Japan.

Sato, M., Kawai, N., Miyake, T., Yasumura, M., Isoda, H., Koshihara, M., Nakajima, S., Araki, Y. and Nakagawa, T., 2016. Structural design of five-storey and three-story specimen of the shaking table test, Proceedings of the 2016 World Conference on Timber Engineering, Vienna, Austria.

Yasumura, M., Kobayashi, K., Okabe, M., Miyake, T. and Matsumoto, K., 2016. Full-scale tests and numerical analysis of low-rise CLT structures under lateral loading, Journal of Structural Engineering, 142(4).

Young Researchers' Forum V
Innovation in Construction Materials
22nd April 2021

Pathological manifestations on concrete bridges in North-eastern Brazil

De Paula, Bruno J. G.
Civil Engineering, Federal University of Minas Gerais, Brazil

Almeida, Fernando C.R.
Department of Materials Engineering and Construction, Federal University of Minas Gerais, Brazil

ABSTRACT

Several factors can cause concrete degradation in bridges and flyovers. Their functional and structural capacities can be jeopardized, resulting in the onset of pathological manifestations throughout their lifespan. The aim of this paper is to identify and evaluate the main pathological manifestations on concrete bridges in roads from North-eastern Brazil. A survey of actual conditions of 126 bridges, located in the top-five most populous and richest states of that region, was carried out. For this, 10 major categories of pathological manifestations, failures and frequently observed defects in those structures were selected. A total of 580 defects or failures were quantified within the bridges sampling group, with an average of 4.60 ± 1.19 defects for each bridge. The main occurrences, found in more than half of the structures analysed, are related to: missing and/or damaged expansion joints (96%); concrete spalling/delamination (82%); reinforcement corrosion (81%); water infiltration (77%); and leaching/efflorescence (52%). Thus, these outcomes can guide public policies for maintenance programmes to increase lifespan of concrete bridges in developing countries.
Keywords: Bridges and flyovers, concrete, pathological manifestations, inspections

1. INTRODUCTION

Bridges and flyovers are road structures that facilitate urban development and improve traffic conditions by shortening distances and connecting poorly accessible regions. However, concrete structures are subjected to aging by chemical and physical deteriorations, which negatively affects their durability and lifespan (Abdul-Ameer, Alhefeiti, 2016; Gjorv 2011). Several factors can cause deterioration of functional and structural capacities, such as environmental actions, excessive usage, structural design errors, overloading, inadequate execution conditions and deleterious materials used for construction (Michel *et al*., 2016; Hüthwohl *et al*., 2019).

In consequence of these factors, additionally to lack of periodic maintenance services, concrete is susceptible to appearance of pathological manifestations (e.g., cracks). In general, many of the defects can be easily detected, recognized and identified by visual inspections (Xie *et al*., 2018).

Inspection services consist in a set of technical procedures, which generate important data and relevant information on structure stability (diagnosis of its functional, structural, and conservation conditions) (Bertolini *et al.* 2013). Overall, a periodic maintenance program provides database for prevention and correction of individual structures subjected to specific situations in field. When carried out according to standard procedures and techniques, necessary information for eventual preventive maintenance repairs are obtained. Moreover, periodic analysis of the structures helps the functional management, ensuring the design performance for the whole lifespan and beyond (Berenguer *et al*., 2016).

Owing to the considerable importance and the high costs involved, maintenance and repairs services have to be effectively planned. In the USA, for example, an estimated amount of over US$ 500 billion has been spent in the maintenance of bridges and highways, in which most of the manifestations occurs due to corrosion of reinforced concrete (Almeida *et al*., 2019).

Thus, the first step for a successful structure maintenance program is to identify the defects and failures in order to guide governmental strategies for decision making. Given these circumstances, this paper aims to identify and evaluate the main pathological manifestations in selected concrete bridges and flyovers, located in roads from Northeast region of Brazil. A total of 126 structures were analysed through standard inspection procedures, considering the 10 main pathological manifestations, flaws and defects recurrently observed in those concrete structures.

Although this study particularly shows inspection analysis of a limited number of concrete bridges and flyovers in a specific region of Brazil, they can raise awareness to the actual conditions of said structures in developing countries.

2. Methodology

A total of 126 bridges and flyovers structures were selected on federal roads located in the five main states of the North and Northeast regions of Brazil: Bahia (BA), Pernambuco (PE), Ceará (CE), Pará (PA), and Maranhão (MA). They were chosen due to their economic relevance in terms of the Gross Domestic Product (GDP) (IBGE, 2018) and estimated population (IBGE, 2020). In other words, they are the richest and most populous states in that region (Table 1).

Table 1. Characteristics of selected Brazilian states

State	Code	GDP (Bi R$)	Population (Million)	Total area (x10³ km²)	Nr. bridges analysed
Bahia	BA	268.7	14.8	564.7	16
Ceará	CE	147.9	9.6	148.9	27
Maranhão	MA	89.5	9.1	331.9	14
Pará	PA	155.2	8.6	1247.9	27
Pernambuco	PE	181.6	7.1	98.3	42
	Total	-	-	-	126

This sampling covers structures located on the following Brazilian Federal Highways: BR-010, BR-020, BR-101, BR-104, BR-135, BR-222, BR-226, BR-316, BR-424.

The survey was made by an extensive photographic documentation analysis, according to the main Brazilian standards and inspection manuals of bridges and flyovers (DNIT, 2004a; DNIT, 2004b; ABNT 2016).

All structures were analysed considering the 10 main concrete related pathological manifestations (PM), including defects, flaws and non-conformities (Table 1, showing each PM identification code). Each PM were identified and quantified (frequency of occurrence).

Table 2. List of the main pathological manifestations (bridges defects) and their respective identification codes

Code	Defect	Code	Defect
PM 01	concrete spalling/delamination	PM 06	leaching / efflorescence
PM 02	reinforcement corrosion	PM 07	cracking
PM 03	concrete erosion	PM 08	concrete biodeterioration
PM 04	concrete segregation	PM 09	missing and/or damaged expansion joints
PM 05	water infiltration	PM 10	fire stains

Finally, a statistical analysis was carried out to evaluate the panorama of the current conservation conditions of the concrete structures in that Brazilian region.

3. Results and discussions

Each observed pathological manifestations (PM) was related to a respective bridge under analysis. In other words, a given bridge may contain one or more PM's in its structure. Thus, a total of 580 pathological manifestations (defect or anomaly or failures) were identified within the sampling group of 126 bridges analysed. The number of each occurrence, by type of pathological manifestation, is shown in Figure 1.

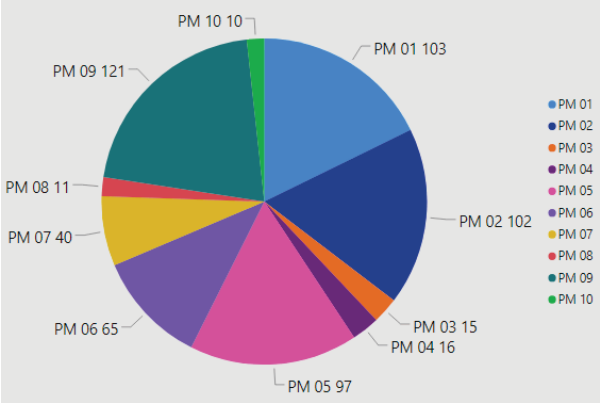

Figure 1. Frequency of occurrence of pathological manifestations in the analysed bridges (total of 580 PM occurrences)

The PM code and the number of occurrences is given on each label in Figure 1. For example, PM01 (concrete spalling/delamination) was observed in 103 bridges, while MP05 (water infiltration) was observed in 97 structures.

It is important to highlight that the level and degree of severity of each failure or defect was not analysed in this study. Among the observed occurrences, it is clear there are structures with more or less severe cases, which depends on the conditions of conservation, propagation and development of the pathological problem. A relatively high number of pathological manifestations observed in a bridge structure does not necessarily means a high degree of degradation. On the contrary, there might be a bridge with a few occurrences of PM, but in a critical state of degradation by reinforced corrosion, for example. Nevertheless, all of those structures demand some type of maintenance or repair services.

Figure 2 shows the percentage of defects calculated in relation to 126 bridges analysed, based on the frequency of occurrence of each PM. The main pathological manifestations found in more than half of the overall analysed structures (i.e., occurrences in above 50% of the bridges) were: missing and/or damaged expansion joints (PM09), with an incidence of 96%; spalling/delamination concrete (PM01), identified in 82% of the structures; reinforcement corrosion (PM02), in 81% of the samples; infiltration (PM05),

in 77% of the structures; and leaching/ efflorescence (PM06), with an incidence of 52%.

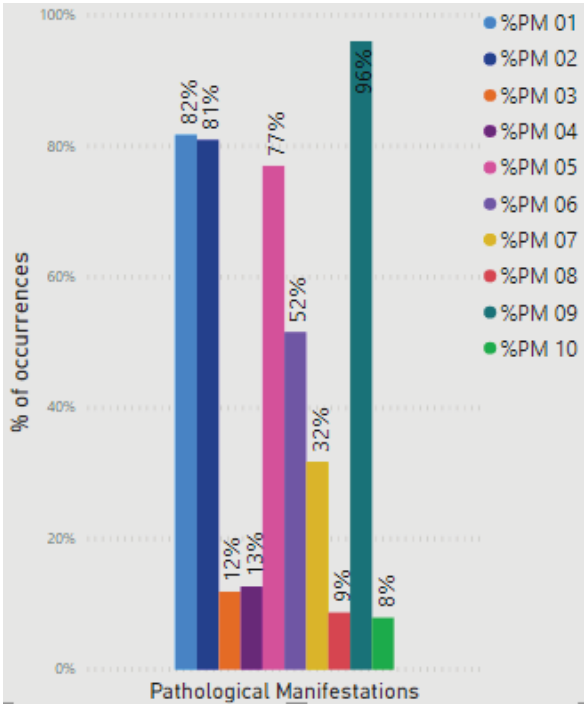

Figure 2. Percentage of occurrence of each pathological manifestation in relation to the total of analysed bridges

By comparing Figures 1 and 2, the sum of frequencies from the top-five PM's (PM09, PM01, PM02, PM05 and PM06) totalized 488 occurrences (out of 580 cases). Thus, it is possible to infer that the five main pathological manifestations represent together almost 85% of all problems related to concrete structures in bridges and flyovers.

Table 3 shows the obtained data for each Brazilian state. By the number of analysed bridges and amount of pathological manifestation (PM) per state, the average, standard deviation and coefficient of variation were calculated. Thus, it was possible to compare these values between different states and relate them to economic, social and territorial issues (Table 1).

Table 3. Analysed data per Brazilian state

State	Quantity of Bridges	Quantity of PM	Average	Standard Deviation	Coefficient of Variation
BA	16	81	5.06	1.56	31%
CE	27	132	4.89	1.16	24%
MA	14	61	4.35	1.41	32%
PA	27	132	4.89	0.82	17%
PE	42	174	4.14	0.98	24%
Total	126	580	4.60	1.19	26%

Overall, the results showed an average of 4.60 pathological manifestations per inspected bridge in the Northeast region of Brazil. The standard deviation was 1.19 and resulting coefficient of variation was 26%, indicating the quantitative dispersion of the analysed data. The last value reflects the conservation condition discrepancy of the analysed bridges, given a variation range between structures with distinct amount of PM occurrences.

It was possible to notice that Bahia (BA), Ceará (CE) and Pará (PA) have the highest average of occurrences, as a result of the greatest amount of pathological manifestations per concrete structures.

The highest coefficient of variation was observed in bridges from Maranhão (MA) state, i.e., there are bigger discrepancies between structures in a very good and very bad conditions (regarding the amount of PM). On the contrary, the lowest coefficient of variation was for Pará state, indicating the most of structures have similar conservation conditions.

Considering economic factors, Maranhão (MA) state, with the lowest GDP, had the second lowest average number of PM per structure analysed (4.35 ± 1.41). On the other hand, the state with the highest GDP (Bahia, BA) showed the highest average of occurrences per inspected bridge (5.06 ± 1.56). In addition, its high coefficient of variation (31%) indicates that state's financial inequality may reflect on the difference of structure conservation levels.

Thus, only analysing economic conditions itself does not suggest the actual conditions of bridges conservation. This is because the richest state should be expected with the highest investments for their repair and maintenance programmes, hence having structures in better conditions.

However, there is a complex net of factors and variables that may affect public investments, in which governments (especially those from developing countries) should considerate to plan specific and effective programmes for special concrete structures.

For example, Bahia (BA) is the wealthiest, most populous and the second most extensive state in the Northeast region, but with high coefficient of variation (Table 3) and the highest average of occurrences. Thus, it seems that public governmental investments to keep bridges and flyovers in adequate conditions are not equally distributed in that territory. As a consequence, some structures located closer to the capital (city of Salvador and surroundings, where is the wealthiest area) may have some advantages over those structures located in the countryside of state.

Furthermore, the state of Pernambuco (PE) has the second highest GDP and the smallest territorial extension. It had the lowest occurrence rates (4.14 ± 0.98) and a relatively low coefficient of variation, indicating better financial management for maintenance services.

Figure 3 shows the same overall pattern of identified defects, regardless the Brazilian state under analysis.

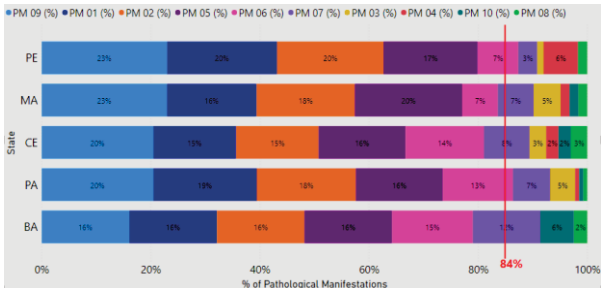

Figure 3. Frequency of pathological manifestations occurrence per Brazilian state.

The main pathological manifestations, responsible for approximately 85% of concrete structures (red line), are related to: missing and/or damaged expansion joints (PM09), concrete spalling/delamination (PM01), reinforcement corrosion (PM02), water infiltration (PM05), and leaching/efflorescence (PM06). Some of the main pathological manifestations are shown in Figure 4.

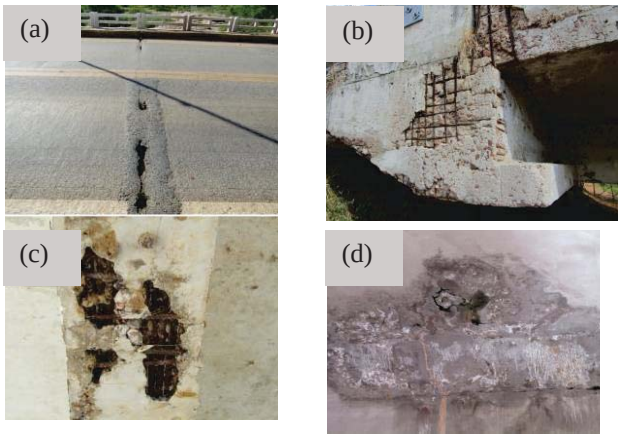

Figure 4. Examples of the main pathological manifestations found: (a) missing and/or damaged expansion joints (PM09); (b) concrete spalling/delamination (PM01); (c) reinforcement corrosion (PM02); (d) water infiltration (MP05) (Strata Eng.)

Although geographical, political, social and economic difficulties inherent to each Brazilian state, there is a consensus on the main problems associated to concrete structures of bridges and flyovers.
Thus, regardless of severity degree of each PM, these results suggest a possible strategic direction for public policies towards the elaboration of structure maintenance and repair programmes. This, specifically applied for the Northeast region of Brazil, can also be extended to other developing countries.

4. Final Considerations

The main pathological manifestations were analysed in concrete bridges on roads located in five Northeastern Brazilian states. An average of 4.60 ± 1.19 occurrences per inspected bridge were found. Variations for each individual state may be related to socioeconomic factors, political interests, territorial extension, and adequate maintenance planning.

The main pathological manifestations in concrete structures, regardless the state where they are located, were: missing and/or damaged expansion joints, concrete spalling/delamination, reinforcement corrosion, water infiltration, and leaching/efflorescence. The occurrence of these issues represents around 85% of the total pathological manifestations observed in the inspected structures.
Thus, these outcomes can guide public policies for maintenance programmes to increase lifespan of concrete bridges in developing countries.

Acknowledgments

The authors acknowledge Strata Engenharia for availability of photographic collection, and Pró-Reitoria de Pesquisa da UFMG.

References

Abdul-Ameer, A.; Alhefeiti, K. (2016) Statistical analyzis of reinforced concrete bridge defects for optimum maintenance planning and budgeting. MATEC Web of Conferences 83, 06001.
ABNT (Brazilian Association of Technical Standards). NBR 9452. Inspeção de pontes, viadutos e passarelas de concreto – Procedimento, 2016. (in Portuguese)
Almeida, F.C.R. *et al.* (2019) Use of sugarcane bagasse ash sand (SBAS) as corrosion retardant for reinforced Portland slag cement concrete. Constr. Build. Mater., 226, 72-82.
Bertolini *et al.* (2013) Corrosion of Steel in Concrete: Prevention, Diagnosis, Repair, 2ed. Wiley-VCH.
Berenguer, R.A. *et al*. (2016) Inspection of the pathological manifestations on Janga Bridge. Electron. J. Geotech. Eng., 21.12, 4583-4594.
DNIT (National Department of Transport Infrastructure). Manual 010/2004 – PRO. Inspeção em pontes e viadutos de concreto armado e protendido, 2004. (in Portuguese)
DNIT (National Department of Transport Infrastructure). Manual 709. Inspeção de pontes rodoviárias, 2004. (in Portuguese)
Gorj, O.E. (2011) Durability of concrete structures. Arab J Sci Eng., 36, 151–172.
Hüthwohl, P. *et al.* (2019) Multi-classifier for reinforced concrete bridge defects. Automat. Constr., 105, 102824.
IBGE (Brazilian Institute of Geography and Statistics). Produto Interno Bruto – PIB (2019).
IBGE (Brazilian Institute of Geography and Statistics). Projeção da população do Brasil e das Unidades da Federação.
Michel, A. *et al.* (2016) Propagation of steel corrosion in concrete: Experimental and numerical investigations, Cem. Concr. Compos., 70, 171–182.
Xie, R. *et al.*, 2018. Automatic multi-image stitching for concrete bridge inspection by combining point and line features. Automat. Constr., 90, 265–280.

Young Researchers' Forum V
Innovation in Construction Materials
22 April 2021

Assessment of Surface Roughness of Ni and Ni-Si_3N_4 nano-composite coatings fabricated by Pulse Electrodeposition

M.Sajjadnejad[a*], H. Karimi Abadeh[b] and R.Rostami[c] S. Karkon[a]

[a*]Department of Materials Engineering, School of Engineering, Yasouj University, Yasouj, Iran
[b] Department of Material Science and Engineering, School of Engineering, Shiraz University, Shiraz, Iran
[c] School of Computing, Engineering and Built Environment, Glasgow Caledonian University, UK
[1]. Corresponding author, email: m.sajjadnejad@yu.ac.ir; m.sajjadnejad@yahoo.com

ABSTRACT

Pulse electrodeposition technique was used to fabricate pure Ni and nano-composite Ni-Si_3N_4 coatings at baseline conditions of current density= 4 $A.dm^{-2}$, duty cycle=50% and pulse frequency= 10 Hz. Atomic force microscopy was used to assess the surface of each coating. To get a clearer understanding each parameter was risen once and the compared with baseline specimen. Observations indicate that the average and root square mean average roughness of nano-composite nickel coatings are higher than pure Ni counterparts. Mean spacing and waviness numerical results have indicated that where ever the preferential nucleation sites are present on the surface, both parameters have increased.

1. INTRODUCTION

Co-deposition of nano-side particles in a metallic matrix is one of the most efficient methods of improving the properties of metallic coatings. Among these coatings, Ni based coatings attracted a great deal of attention as a result of their excellent protective nature (Low, Wills et al. 2006, Sajjadnejad, Omidvar et al. 2017). Moreover, different particles such as SiC, Al_2O_3, graphene and carbon nano-tubes in different size and shapes have been successfully incorporated into Ni based coatings (Algul, Tokur et al. 2015, Sajjadnejad, Omidvar et al. 2017, Ghazanlou, Farhood et al. 2019). These additions have improved corrosion and wear behavior of such coatings to a high extent.

Electrodeposition parameters affects the properties of the fabricated coatings to a high extent. As a result of that, a huge number of papers have been and are being published which are aimed at understanding the effect of parameter alterations on coatings to get to an optimum in coating behavior. One of the most important factors in electrodeposition process is the applied current density. The applied current supplements the required force to detach ions form anode surface, move them and then deposit them on the surface of the cathode. Direct current is the first type of current that has been used to achieve this aim. However, it was realized that addition of several other parameters related to applied current (i_p) will give us a greater control on the process, thus pulsed applied current was taken under consideration and literature now is agreed that by using this method, coatings with improved properties can be fabricated.

Pulse electrodeposition introduce two additional parameters into the process, duty cycle (γ) and pulse frequency (f). Duty cycle is the representation of percentage of the time total on-time of a cycle, as seen in equation 1.

$$\gamma = \frac{T_{ON}}{T_{ON}+T_{OFF}} = T_{ON}.f \quad (1)$$

In this equation, T_{ON} is length of applied current and T_{OFF} is usually called relaxation time. f is the pulse frequency of applied current defined as the reciprocal of the cycle time (T):

$$f = \frac{1}{T_{ON}+T_{OFF}} = \frac{1}{T} \quad (2)$$

Altering these two parameters have proven to change the properties of coatings by changing the applied overvoltage on the surface of the coatings, thus changing the incorporation rate of particles and morphology of coatings which directly change the corrosion and tribological behavior of the samples.

Among particles, as a result of its amazing properties such as outstanding fracture toughness and hardness, thermal shock capacity and low density, silicon nitride (Si_3N_4) is a logical choice to be incorporated into such coatings. Incorporation of silicon nitride into Ni matric by Mohan Reddy et al. have produced a coating with reduced crystallite size, microstructure refinement and corrosion behavior of the coatings.

The aim of the following paper is to analyze the topography of Ni and nano-composite Ni-Si_3N_4 coatings that have been fabricated using pulse current technique, and compare the effect of different electrodeposition parameter alteration on the topography of the coatings.

2. EXPERIMENTAL

Pure Ni and nano-composite coatings were electroplated using pulsed current applied current in the solution reported in Table 1. Copper was used as a substrate (cathode) and a pure nickel sheet of 7 times the dimension was chosen as the anode. The surface of the cathode was abraded by emery paper, washed with water and cleared with ethanol. HCl 15% was used to activate the surface of the cathode. After this steps samples were washed again and placed in the electrodeposition chamber. The temperature was fixed at 50° C and to ensure a homogenous environment stirring was done at 250 rpm. The pH was also fixed at 4. H_3BO_3 was added as a buffer to control the pH of the environment. Sodium dodecyl sulfate (SDS) was added to the solution of nano-composite plating environment to act as a anionic surfactant and improve their wettability and suspension in the solution. Aldrich silicon nitride powder of under 100 nm diameter size were chosen, cleaned by ethanol ultrasonic bath for 30 minutes, dried on a carbon layer and then added to the solution.

After electrodeposition process, surface of the samples were analysed using atomic force microscopy (AFM), Gwyddion was used to analyse the data. Background tilt was removed by polynomial background method and then roughness, waviness, mean spacing was calculated based on a line that will pass through all the highest peak of the sample.

Table 1. Electrochemical parameters and chemical composition of the bath.

Species and Variables	Concentration and Range
$NiSO_4.6H_2O$	300 (g/L)
H_3BO_3	40 (g/L)
$NiCl_2.6H_2O$	40 (g/L)
Current Density	4, 10 ($A.dm^{-2}$)
Pulse Frequency	10, 100 (Hz)
Duty Cycle	50, 75 (%)
$CH_3(CH_2)_{11}SO_4Na$ (SDS)	0.3

3. RESULTS AND DISCUSSION

The topographic 2D surface of the pure Ni samples and texture, waviness and roughness graphs are presented in Figure 1 and the related data are reported in Table 2. It should be noted that the baseline sample was fabricated at i_p = 4 $A.dm^{-2}$, γ= 50% and f= 100 Hz; then each parameter was raised to understand the effect of that parameter.

Concerning Figure 1 and the topography of pure Ni coatings; it's clear that baseline sample (Figure 1.a).

possess the highest amount of roughness and waviness. Waviness is an indication of more remotely spaces irregularities on the surface texture. It is more strictly defined to account into the irregularities that the sampling length cannot take into account.

Table 2. Obtained amount of average roughness (R_a), square root roughness (R_s), Waviness, mean spacing (S_m) and wavelength (λ).

Sample	R_a (nm)	R_s (nm)	Waviness (nm)	S_m (nm)	λ
Pure Ni Baseline	51.034	61.642	92.567	4.085	3.955
i_p= 10 $A.dm^{-2}$	27.912	36.248	37.424	3.801	4.018
γ= 50%	34.348	47.641	94.545	4.960	4.497
f= 100 Hz	38.241	63.354	80.362	3.816	4.020
Ni-Si_3N_4 Baseline	55.054	73.617	341.650	4.438	4.298
i_p= 10 $A.dm^{-2}$	66.626	90.255	360.134	5.447	5.152
γ= 50%	36.341	48.183	82.756	3.529	3.820
f= 100 Hz	30.106	37.947	82.585	3.242	3.466

Increasing the current density to 10 $A.dm^{-2}$ (Figure 1.b) decreases the roughness of the surface. This is expected since increasing current density will increase the nucleation rate on the surface and as a result a more homogenous surface is expected (Li, Gu et al. 2015). However, it seems that some hotspots for growth is seen on the surface of this sample. When current density is heightened in an electroplating environment, more ions are ready to be adsorbed on the surface and if a preferential nucleation site exist on the surface, all ions will deposit in a single area and ions deficit areas will form around it, this trend is clearly seen in Figure 1.b (the glowing areas are peaks while ion deficit areas are darker and around it). The mean spacing between peaks has also been marginally lowered. This is also the result of a heightened crystal nucleation on the surface and mitigation of growth.

The same trend can also be seen for the sample with a higher duty cycle of 75% (Figure 1.c). Raising the duty cycle of the system, will also increase the over-potential at the surface of the sample. Thus more nucleation sites, inhibition of growth and as a result a more homogenous surface (Sajjadnejad, Ghorbani et al. 2015).

Increasing the pulse frequencies of the process will also increase the over-potential of the surface. Although the surface is smoot compared to the baseline sample, an increased amount of growth hotspots can be observed in the topographic map of the surface (Figure 1.d). This is the reason why R_s experienced an increase since this parameter is more sensitive to surface irregularities. All other parameters have experienced a drop since except for the growth hot spots, this sample possess a smoother surface compared the baseline sample.

The topographic maps of the surface of the nano-composite Ni-Si_3N_4 sample are illustrated in Figure 2 and the numerical calculated data are reported in Table 2. It can be clearly deduced that particle incorporation has risen the roughness of the coatings. Several factors might contribute to this behaviour. First, when particles are incorporated into a coating, nucleation sites are increased. The existence of these preferential nucleation sites will create growth hot spots that will ultimately increase

the roughness of the surface. The waviness and R_s of the baseline sample has also increased at least threefold. As these two parameters are more sensitive to surface irregularities, these indicate the existence of growth hotspots on the surface which can also be clearly seen on the topographic maps of the sample in Figure 2.a. Moreover, ion deficit areas are also apparent around these growth hot spots.

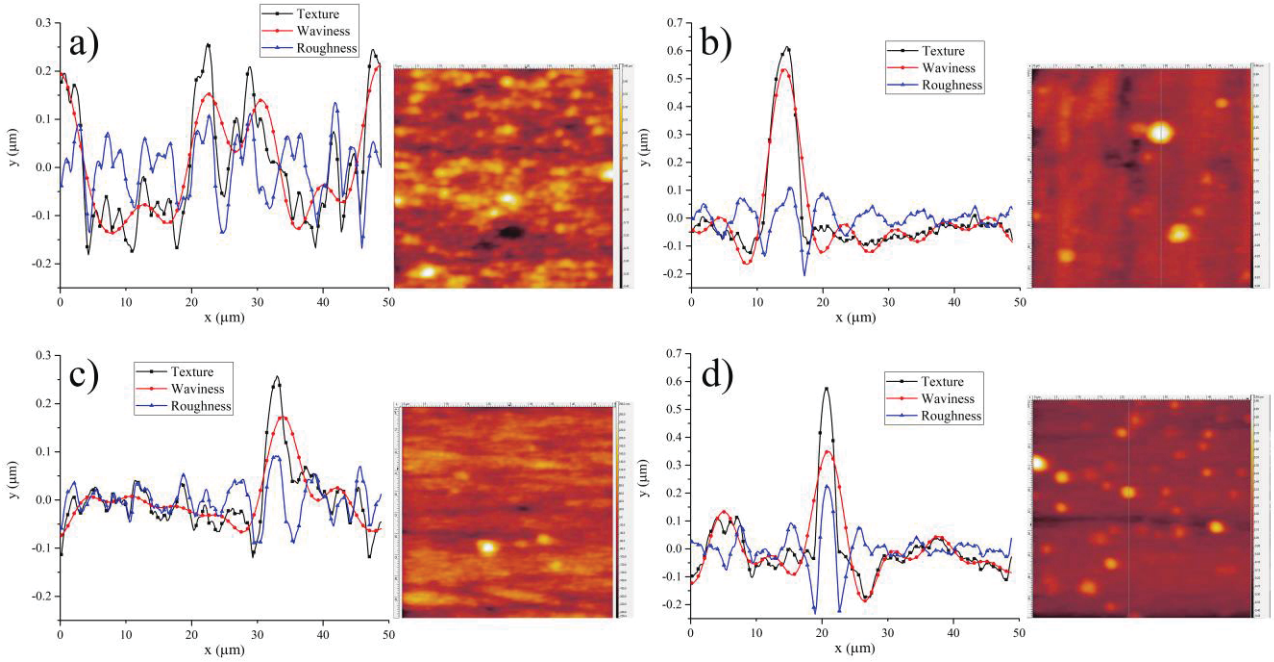

Figure 1. Topographic and texture, waviness and roughness maps of pure Ni samples.

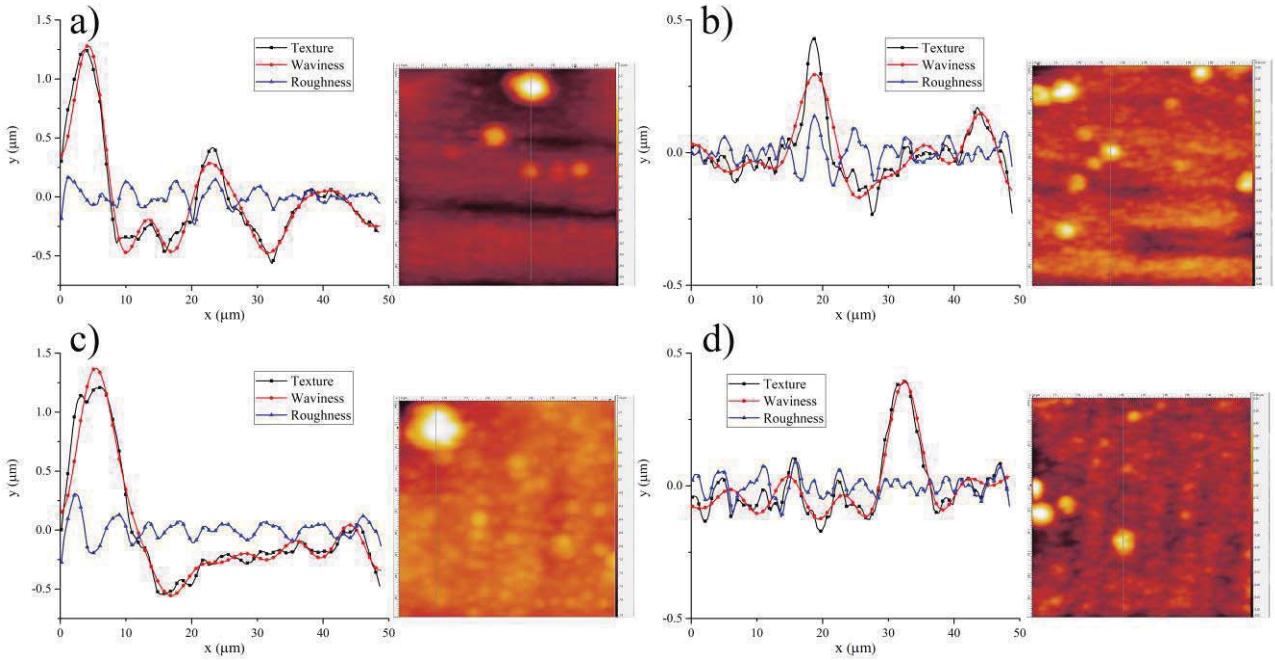

Figure 2. Topographic and texture, waviness and roughness maps of nano-composite Ni-Si_3N_4 samples.

Increasing the current density (Figure 2.b) in the nano-composite samples have also increased the roughness of the samples for the same reasons as of pure Ni coatings. Furthermore, it appears that more growth hot spots are present on the surface of this sample. A high increase in the amount of R_s and waviness can be attributed to this fact. Based on Guglielmi (Guglielmi 1972) model of partice incorporation into the metallic matrixes, heightening the current density increases the speed of particles to reach the cathode surface, thus more growth hot spots can form as a result of higher amount of preferential nucleation sites.

As it appears in Figure 2. c&d, increasing current density and pulse frequency have created a smoother surface. All surface parameters have experienced a drop and are comparable with pure Ni samples as growth is more homogenous in the surface. Furthermore, although growth hotspots

are seen on the surface, they are much rarer in their appearance.

4.Conclusion

1-Incorporation of particles into the coatings has increased the roughness of the surface of nano-composite Ni-Si_3N_4 coatings.

2-Increasign the current density has also increased the roughness of Ni-Si_3N_4 coatings by creating more growth hot spots and ion deficit sites during the growth of the coatings.

3-Increasing duty cycle and pulse frequency smoothened the surface on both Ni and Ni-Si_3N_4 coatings.

References

Algul, H., M. Tokur, S. Ozcan, M. Uysal, T. Cetinkaya, H. Akbulut and A. Alp (2015). "The effect of graphene content and sliding speed on the wear mechanism of nickel–graphene nanocomposites." Applied Surface Science **359**: 340-348.

Ghazanlou, S. I., A. Farhood, S. Ahmadiyeh, E. Ziyaei, A. Rasooli and S. Hosseinpour (2019). "Characterization of Pulse and Direct Current Methods for Electrodeposition of Ni-Co Composite Coatings Reinforced with Nano and Micro ZnO Particles." Metallurgical and Materials Transactions A **50**(4): 1922-1935.

Guglielmi, N. (1972). "Kinetics of the deposition of inert particles from electrolytic baths." Journal of the Electrochemical Society **119**(8): 1009-1012.

Li, X., Y. Gu, T. Shi, D. Peng, M. Tang, Q. Zhang and X. Huang (2015). "Preparation of the multi-walled carbon nanotubes/nickel composite coating with superior wear and corrosion resistance." Journal of Materials Engineering and Performance **24**(12): 4656-4663.

Low, C., R. Wills and F. Walsh (2006). "Electrodeposition of composite coatings containing nanoparticles in a metal deposit." Surface and Coatings Technology **201**(1-2): 371-383.

Sajjadnejad, M., M. Ghorbani and A. Afshar (2015). "Microstructure-corrosion resistance relationship of direct and pulse current electrodeposited Zn-TiO2 nanocomposite coatings." Ceramics International **41**(1): 217-224.

Sajjadnejad, M., H. Omidvar and M. Javanbakht (2017). "Influence of pulse operational parameters on electrodeposition, morphology and microstructure of Ni/nanodiamond composite coatings." Int. J. Electrochem. Sci **12**(5): 3635-3651.

Sajjadnejad, M., H. Omidvar, M. Javanbakht and A. Mozafari (2017). "Textural and structural evolution of pulse electrodeposited Ni/diamond nanocomposite coatings." Journal of Alloys and Compounds **704**: 809-817.

Young Researchers' Forum V
Innovation in Construction Materials
22nd April 2021

Evaluation of chloride penetration in cementitious composites with sugarcane bagasse ash sand

Almeida, Fernando C.R.
Department of Materials Engineering and Construction, Federal University of Minas Gerais, Brazil

Sales, Almir
Department of Civil Engineering, Federal University of São Carlos, Brazil

Moretti, Juliana P.
Sea Institute, Federal University of São Paulo, Brazil

Mendes, Paulo C.D.
São Carlos Institute of Chemistry, University of São Paulo, Brazil

Quarcioni, Valdecir A.
Institute for Technological Research of the State of São Paulo, Brazil

ABSTRACT

Corrosion of steel reinforcement is a major problem of concrete structures, which is aggravated in the presence of chloride ions. Sugarcane bagasse ash sand (SBAS), the main agro-industrial waste in sugar and ethanol production, has the potential to enhance concrete durability. Thus, this paper aims to evaluate the effect of SBAS as fine aggregate in the chloride penetration depth of cementitious matrices. Concrete and mortars samples were produced with SBAS, in replacement of natural sand, in three different contents: 0% (reference), 30%, and 50%. Tests for determining compressive strength, void index, electrolytic conductivity and chloride penetration depth were carried out. The results showed that finer particles of SBAS and secondary C-S-H phases formed from hydration of blended cement with blast-furnace slag (activated by SBAS) lead to increased mechanical strength and increased chloride resistance. The physical effect of SBAS is more significant than chemical influence, especially in concrete samples. Chloride penetration depth is reduced up to 15% and 30%, respectively for mortars and concrete with SBAS.

Keywords: Sugarcane bagasse ash sand (SBAS), durability, chloride attack, Portland composite cement

1. INTRODUCTION

Deterioration of concrete structures has emerged as one of the most severe and demanding challenges facing the construction industry. In this context, corrosion of embedded steel represents the major issue related to loss of durability and long-term performance (Gjørv 2011).
Chloride ions are the principal aggressive agents responsible for corrosion induction. A localized breakdown of the passive layer occurs when a sufficient amount of chlorides reaches reinforcing bars, and then corrosion process is initiated. Chlorides in concrete can be either dissolved in pore solution (free chlorides) or chemically and physically bound to cement hydrates and their surfaces (bound chlorides). However, only the free chlorides are responsible for initiating the process of corrosion (Bertolini *et al.* 2013; Poursaee 2016).
These ions' ingress can be through the use of chloride-contaminated components (e.g., $CaCl_2$ as accelerators) or diffusion into the concrete from the outside environment, especially in coast regions.
Construction industry is continuously searching for innovations and sustainable solutions to improve environmental, technical and cost requirements. In an attempt to explore new recycling opportunities, the field of construction materials and technologies has been challenged to prove the feasibility of advantageously incorporating industrial by-products (Moriconi, 2016). Supplementary cementitious materials and alternative aggregates are suitable solutions for replacing raw materials in production of concrete and mortars (Lothenbach *et al.* 2011*;* Shafigh *et al.* 2014; Scrivener *et al.* 2018; Juenger *et al*. 2019). However, incorporation of waste materials may influence the effectiveness of concrete in promoting a protecting medium for reinforcing steel bars, due to changes in

microstructure, alkalinity, chemical compositions and permeability.

Sugarcane bagasse ash sand (SBAS), a by-product from sugar and ethanol production, is a potential substitute for natural sand in cementitious composites (Almeida *et al*. 2015; Almeida *et al*. 2019). Brazil is the world's largest sugarcane producer and exporter with an estimated SBAS generation of 4 million ton/year (Moretti *et al*. 2018). However, the influence of SBAS incorporation in durability of reinforced concrete structures is still unclear and deficient.

Therefore, the aim of this paper is to evaluate the effect of SBAS as a fine aggregate in the chloride penetration depth of cementitious composites.

2. Methodology

Concrete and mortars samples were produced with sugarcane bagasse ash sand (SBAS), in replacement of natural sand, in three different contents (in mass): 0% (reference), 30%, and 50%. Portland composite cement with 34% (in mass) of blast-furnace slag was used: CPII-E32 (ABNT, 2018]) similar to CEM II/B-S (BSI, 2011).

Particularly for concrete samples, basalt gravel was used as coarse aggregate, with maximum dimension of 19 mm.

For conventional fine aggregate, natural quartz sand had particle sizes below 6.3 mm, with fineness modulus of 2.32.

SBAS samples were homogenised by sieving (#4.8 mm sieve) and grinding (for 3 min) processes. SBAS had a predominantly crystalline structure of SiO_2 α-quartz (above 80%). It had particle sizes below 1.18 mm, with fineness modulus of 1.15 (Figure 1). Notably SBAS was much finer than natural sand.

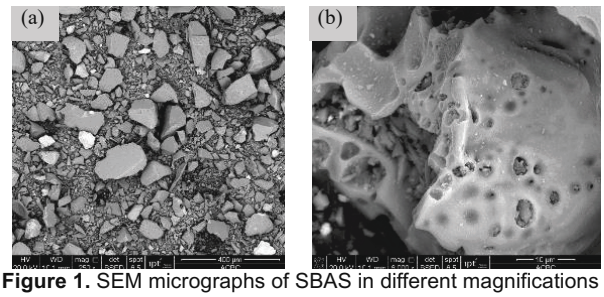

Figure 1. SEM micrographs of SBAS in different magnifications

Table 1 shows mix proportions of the cementitious composites. Water/cement (w/c) ratio was adjusted to keep the same consistency of the respective reference sample: mortars with 255 ± 5 mm (by flow test, BSI 2006) and concrete with 90 ± 5 mm (by slump test, BSI 2009). SBAS demanded more water due to its fineness and porous microstructure (Figure 1b).

Tests of compressive strength (ABNT, 2007) and index void (ABNT, 1987) were carried out at 28 days (samples cured in humid chamber, T = 21 ± 2 °C and RH = 95 ± 5%). Electrolytic conductivity was analysed for the pore solution extracted from finely macerated concrete samples (Shi, 2004).

Table 1. Mix proportions of mortar and concrete samples

Sample	SBAS (%)	Cement	Sand	SBAS	Gravel	w/c ratio
RM	0	1.00	2.00	-	-	0.42
30M	30	1.00	1.40	0.60	-	0.44
50M	50	1.00	1.00	1.00	-	0.47
RC	0	1.00	2.00	-	2.86	0.52
30R	30	1.00	1.40	0.60	2.86	0.53
50R	50	1.00	1.00	1.00	2.86	0.54

Chloride penetration depth was evaluated by the colorimetric method (AASHTO, 2002) by sprinkling 0.1 M of $AgNO_3$ solution and fluorescein alcoholic solution on the broken surface (Figure 2).

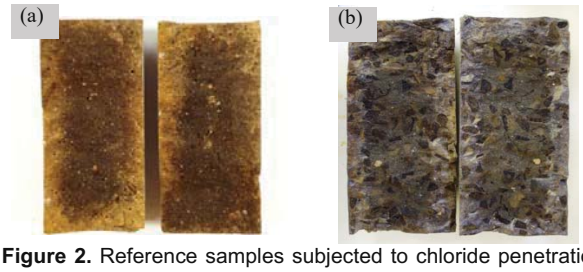

Figure 2. Reference samples subjected to chloride penetration test: (a) mortar and (b) concrete without SBAS

The specimens were kept immersed in saline solution (3.5% NaCl) for 12 weeks (for mortars) and 24 weeks (for concrete).

3. Results and discussions

Figure 3 shows results of compressive strength and void index of mortars samples.

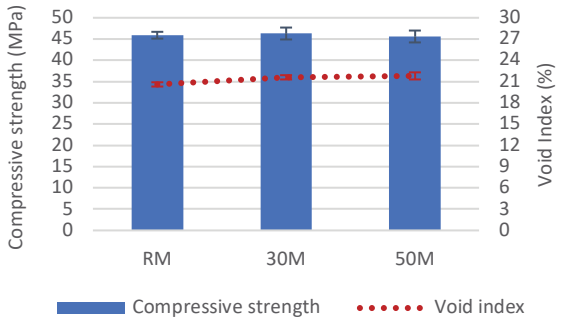

Figure 3. Results of compressive strength and void index of mortars with (and without) SBAS

A slight increase of void index was observed in SBAS mortars due to increased amount of water in the mix. However, mechanical properties were not affected by incorporation of SBAS. The compressive strength averages of RM, 30M and 50M were statistically equivalent at a significance level of 5% (ANOVA).

On the other hand, an improved effect on mechanical properties and no significant influence on void index were observed in concrete samples (Figure 4). Incorporation of SBAS increased the compressive strength by around 10% for both SBAS composites, even with higher w/c ratios.

This increment can be attributed to packing effect where the fine SBAS particles are able to fill pores in size ranges of 60-80 μm and 100-300 μm (Almeida *et al*. 2015), resulting in a denser microstructure. Moreover, the increased compressive strength can also be related to the activation of blast-furnace slag by SBAS due to its higher pH (compared to natural sand) (Castaldelli *et al*. 2013).

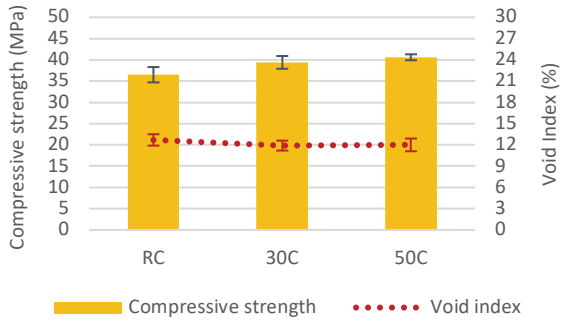

Figure 4. Results of compressive strength and void index of concrete with (and without) SBAS

Usually, C-S-H formed in PC-slag blends has lower Ca/Si ratio and a higher Al/Si ratio than pure Portland cement (PC) (Lothenbach *et al*. 2011). Introducing alumina into the C-S-H phase, to form C-A-S-H, markedly increases its alkali-binding capacity and, hence, reduces alkalinity of the pore solution (Hong & Glasser 2012). However, higher pH of SBAS was able to mitigate this reduction in alkalinity, as evidenced by the results of electrolytic conductivity of the aqueous pore solution (Table 2).

Table 2. Results of conductivity of the aqueous solution

	RC	30C	50C
Electrolytic conductivity (mS/cm)	7.28	8.33	8.97

The higher SBAS content, the higher OH^- concentration, since hydroxide ions are the most conductive ions found in concrete pore solutions (Hewlett, 2003). Thus, secondary C-S-H phases formed from hydration of SBAS-PC-slag system result in concretes with higher strength and lower permeability.

As a consequence, durability of composites made with sugarcane bagasse ash sand can be enhanced, as indicated by the results of chloride penetration test (Figure 5). This qualitative method indicates the presence of free chloride ions which indeed represent a risk for eventual reinforcement corrosion.

By ANOVA and Student's t-test analysis, all averages were statistically different (at a significance level of 5%), i.e., incorporation of SBAS considerable reduced chloride penetration depths. This reduction was lower for mortars (up to 15%) due to equivalent compressive strengths and lower period to chloride exposure. However, reduction in Cl^- penetration reached up to 30% in concrete samples with 50% of substitution. The higher chloride resistance is attributed to chemical and physical effects of SBAS.

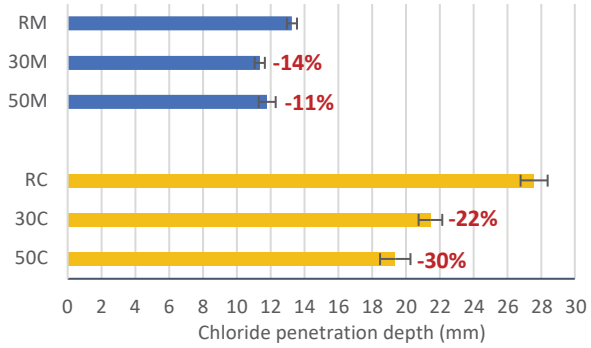

Figure 5. Results of chloride penetration depth of mortars and concrete with (and without) SBAS.

The chemical effect can be related to slag activation by SBAS. The higher pH of SBAS (compared to natural sand) contributes to activate hydration of Portland-slag cement, resulting in formation of secondary C-S-H. This leads to refinement of the cementitious microstructure and, hence, reduced permeability in SBAS composites. Moreover, chlorides can bind to aluminate phases or are adsorbed on C-S-H.

The physical effect, in turn, is attributed to the filling of micropores with SBAS particles and the reduction of capillary interconnectivity by adding a finer material in the mix. Moreover, ionic diffusion can be considered as the main transport mechanism of chloride ions in concrete with SBAS. The presence of diverse ions in the pore solution (e.g., Na^+, K^+, Ca^{2+}, and OH^-) slows down the rate of Cl^- ingress via mechanisms of repulsion or attraction among the electrical charges (Loser *et al*. 2010). Thus, incorporation of finer particles of SBAS affects the transport mechanisms and thus acts as a barrier against chloride ion penetration.

Considering the difference of microstructure between concrete and mortars specimens, the effect of SBAS were more notable in concrete specimens (Figure 6).

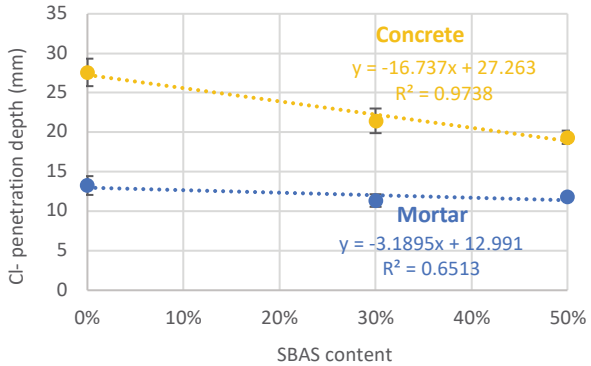

Figure 6. Correlations between SBAS content and chloride penetration depth in concrete and mortars specimens

This can be related to the higher w/c ratios and presence of gravels, which increased porosity of the paste. Thus, the physical effect of SBAS showed to be more prominent in filling the

micropores and considerable reducing ions migration.
Migration of chloride ions in cementitious composites can be approximated by a partial differential equation (Eq. 1) of a non-steady-state diffusion (Gjørv, 2017).

$$\frac{\partial C}{\partial t} = -D_{ns}\frac{\partial^2 C}{\partial x^2} \quad (1)$$

Where ∂C is the variation of chloride concentration in function of *x* (position) and *t* (time), and D_{ns} is the non-steady-state chloride diffusion coefficient.
Thus, incorporation of SBAS leads to decreased diffusion coefficients *(D_{ns})* and, consequently, to higher resistance to chloride penetration. By regression analysis, the physical effect of SBAS is more significant than chemical influence, especially in concrete samples.

4. Final Considerations

Concrete and mortars produced with sugarcane bagasse ash sand (SBAS) were evaluated in terms of chloride penetration depths. From the experimental results, it was noted that SBAS does not affect mechanical properties of mortars but increases up to 10% of compressive strength of concrete at 28 days.
Primarily, finer SBAS particles, as well as secondary C-S-H phases formed from hydration of Portland composite cement with blast-furnace slag (activated by SBAS) are responsible for composites with higher strength and lower permeability. Consequently, this leads to increased chloride resistance. Chloride penetration depth is reduced up to 15% and 30%, respectively for mortars and concrete with SBAS.
Thus, incorporation of SBAS leads to more durable concrete structures, with lower susceptibility to corrosion of steel reinforcement.

Acknowledgments
The authors acknowledge CAPES 001 and MCTI/CNPq (grant #309892/2013-9) for financial support, and Pró-Reitoria de Pesquisa da Universidade Federal de Minas Gerais.

References

AASHTO, T 259 (2002)- Standard method of test for resistance of concrete to chloride ion penetration.
ABNT, NBR 16697 (2018) Portland cement - Requirements (in Portuguese).
ABNT, NBR 5739 (2007) Concrete - Compressive strength test of cylindric specimens - Method of test (in Portuguese).
ABNT, NBR 9778 (1987) Hardened cement mortar and concrete –-Determination of water absorption by immersion, void index and bulk density - Method of test (in Portuguese).
Almeida *et al.* (2015) Sugarcane bagasse ash sand (SBAS): Brazilian agroindustrial by-product for use in mortar. Const Build Mat 82, 31-38.
Almeida *et al.* (2019) Use of sugarcane bagasse ash sand (SBAS) as corrosion retardant for reinforced Portland slag cement concrete. Const Build Mat 226, 72-82.
Bertolini *et al.* (2013) Corrosion of Steel in Concrete: Prevention, Diagnosis, Repair, 2ed. Wiley-VCH.
BSI, BS EN 1015-3 (2006). Methods of test for mortar for masonry — Part 3: Determination of consistence of fresh mortar (by flow table).
BSI, BS EN 12350-2 (2009). Testing fresh concrete. Slump-test.
BSI, BS EN 197-1 (2011) Cement. Part 1: Composition, specifications and conformity criteria for common cements.
Castaldelli *et al. (*2013) Use of slag/sugar cane bagasse ash (SCBA) blends in the production of alkali-activated materials, Materials (Basel) 6, 3108-3127.
Gjørv, O.E. (2011) Durability of concrete structures. Arab J Sci Eng., 36, 151-172.
Gjørv, O.E. (2017) Durability Design of Concrete Structures in Severe Environments, 2ed, CRC Press.
Hewlett P. (Ed.), Lea's Chemistry of Cement and Concrete, 4ed, Elsevier, London, 2003.
Hong & Glasser (2002) Alkali sorption by C-S-H and C-A-S-H gels: Part II. Role of alumina, Cem. Conc. Res. 32, 1101-1111.
Juenger *et al.* (2019) Supplementary cementitious materials: New sources, characterization, and performance insights. Cem Concr Res 122, 257-273.
Loser *et al.* (2010) Chloride resistance of concrete and its binding capacity - comparison between experimental results and thermodynamic modeling, Cem. Conc. Compos. 32, 34-42.
Lothenbach *et al.* (2011) Supplementary cementitious materials. Cem Conc Res 41, 1244-1256.
Moretti *et al* (2018) Self-compacting concrete incorporating sugarcane bagasse ash. Const Build Mat 172, 635-649.
Moriconi, G. (2016) Effect of using recycled materials in concrete on the corrosion of the steel bars. In: Corrosion of Steel in Concrete Structures. 1 ed. Elsevier. 149-166.
Poursaee, A. (2016) Corrosion of Steel in Concrete Structures. 1 ed. Elsevier.
Scrivener *et al.* (2018) Eco-efficient cements: Potential economically viable solutions for a low-CO_2 cement-based materials industry. Cem Conc Res 114, 2-26.
Shafigh *et al*. (2014) Agricultural wastes as aggregate in concrete mixtures – A review. Const. Build. Mat. 53, 110-117.
Shi, C. (2004) Effect of mixing proportions of concrete on its electrical conductivity and the rapid chloride permeability test results, Cem. Conc. Res. 34, 537-545.

Young Researchers' Forum V
Innovation in Construction Materials
22 April 2021

Crushing Process Impact on the Characteristics of Fine Recycled Aggregates

Silva Neto, Gilberto A., Santos, White J. and Gumieri, Adriana G.
Department of Materials Engineering and Construction, Federal University of Minas Gerais, Brazil

Montenegro, Luiz C.M.
Department of Mining Engineering, Federal University of Minas Gerais, Brazil

Nascimento, Aline C.K.
Department of Civil Construction, Federal University of Technology - Paraná (UTFPR), Brazil

ABSTRACT

Crushing process of construction and demolition waste is an important step of the production of recycled aggregates, once it has a fundamental role on the determination of the physical characteristics of these materials. This paper evaluates the differences between two fine recycled aggregates (FRAs), originated from coating mortar waste, and produced by two different crushing processes: jaw crusher only; and jaw crusher plus roller mill. The evaluated characteristics of the FRAs were: particle size distribution; fineness modulus; fines content; grain shape, specific gravity; and water absorption. It was noticed out that when the crushing process changes, the physical characteristics of the FRAs also changes. The FRA produced using jaw crusher plus roller mill, compared with the other one, presented a higher fines content, more spherical and porous grains, which made the water absorption capacity of it higher. On the other hand, both produced FRAs have a continuous particle size distribution.

1. INTRODUCTION

The growing concern with environmental preservation and sustainable development has led to the development of recycling methods of construction and demolition waste (CDW). The production and use of recycled aggregates are common practices in the construction industries of several countries (Ismail and Ramli, 2013). The Annual Review 2018-2019 of the European Aggregates Association (UEPG, 2020) reported that the generated recycled aggregates in that period were approximately 12% of the total aggregate production in the European Union (EU).

The processing of CDW consists of collection, transportation, separation, crushing, sieving, storage and subsequent use of the generated aggregates. Such procedures are very similar to those performed in the production process of natural aggregates, including the used equipment (Leite, 2001). According to Lima (1999), the CDW can be crushed one or more times, reducing the dimensions of the particles and providing greater control of the particle size distribution of the obtained recycled aggregates.

The content of impurities, particle size distribution, shape and strength of the grains are some of the main characteristics of the recycled aggregates affected by the procedures and equipment adopted in the processing of the CDW (Lima, 1999; Matias et al., 2013).

Several types of crushers are used to process the CDW, including:

- Impact crushers: the crushing occurs by the shock of massive hammers fixed to a rotor with fixed impact plates, in an impact chamber. Such crushers promote a high reduction in the dimensions of the crushed particles (generating a good percentage of fines and often re-crushing is unnecessary). In addition, they generate grains in a cubic form (Lima, 1999). The FRA processed by this type of crusher tends to have a higher unit weight compared to the FRA processed by jaw crushers, due to the greater production of sand with a dimension smaller than 4.8 mm (Souza et al., 2016);

- Jaw crushers: the material is crushed in the crushing chamber with high noise emission, generating a large amount of coarse aggregates, since they do not reduce the size of the particles much. Therefore, it is sometimes necessary to re-crush using hammer mills, smaller jaw crushers, among others (Lima, 1999). As stated by Souza et al. (2016), this type of crusher has difficulty in producing sand, whose dimension is smaller than 4.8 mm. In addition to this information, Marinho et al. (2016) pointed out in

their studies that FRAs processed by jaw crushers have thicker curves than those processed by impact ones.

- Hammer mills: this equipment has a small entrance mouth and produces a large number of fine particles, in addition they have a removable grid in the exit mouth, preventing the exit of coarse grains (Lima, 1999);

As reported by Souza et al. (2016), the nature of the CDW has a greater influence on the shape index, specific gravity and unit weight, water absorption, Los Angeles abrasion, and mortar adherence in FRA grains, than the type of crusher adopted in the processing of the recycled aggregate. On the other hand, Oksri-Nelfia et al. (2016) warn that the comminution process contributes to the particle size distribution and shape of aggregate grains.

This paper aims to evaluate the influence of the comminution process by analyzing the physical characteristics of the fine recycled aggregates originated by two different methods: primary crushing (jaw crusher) and primary plus secondary crushing (jaw crusher and roller mill).

2. Materials and Methods

It was decided to use in this research, exclusively, the residue of mixed mortar (made of cement and lime) for the production of the recycled fine aggregates, since this waste is found in great volume in the construction sites.

In relation to the equipment used in the comminution process of the waste, the jaw crusher (Figure 1a) and the roller mill (Figure 1b) were used. Of the two recycled fine aggregates (FRAs) produced and analyzed in this research, one was originated from the jaw crusher followed by sieving in the 2.4 mm aperture mesh (FRA-1) and the other one was generated by the jaw crusher followed by the roller mill and interspersed by passing through the sieve with the same mesh aperture (FRA-2).

Figure 1. Crushing equipment (a) jaw crusher (b) roller mill.

The Figure 2 presents the scheme of the crushing process adopted in this research for the production of the two fine recycled aggregates.

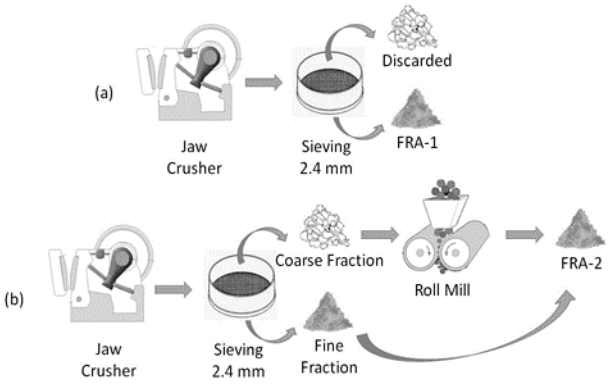

Figure 2. Crushing process schemes of (a) FRA-1 (b) FRA-2.

The generated FRAs were physically characterized based on Brazilian standards regarding: sieve analysis (ABNT, 2003a) equivalent to ASTM C136; content of materials finer than 75-μm (ABNT, 2003b) equivalent to ASTM C117; water absorption (ABNT, 2001) and specific gravity (ABNT, 2009a) both equivalent to ASTM C128; and unit weight (ABNT, 2006) equivalent to ASTM C29. These tests were performed for purposes of comparison between the two fine recycled aggregates.

In addition to these procedures, images were taken with a digital microscope of magnification capacity of up to 1000 times, to analyze the shape of the grains as well as their surface.

3. Results and Discussion

After the physical characterization of the produced FRAs, it was found that both aggregates presented a continuous particle size distribution curve (Figure 3), which is quite valid for improving the compactness of cementitious composites that come to use these recycled fine aggregates, due to the better packing of the materials.

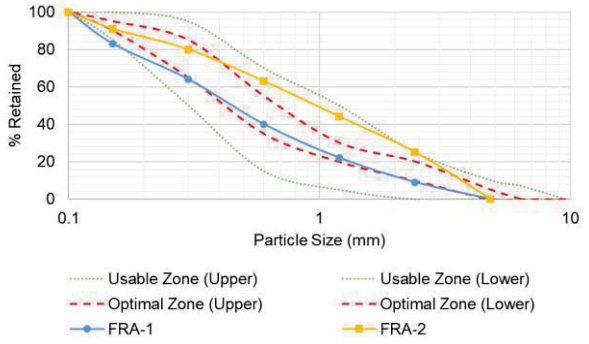

Figure 3. Particle size distribution curve.

Comparing them to the limit curves of the Brazilian standard for specifying aggregates for concrete NBR 7211 (ABNT, 2009b), it can also be seen in Figure 3 that FRA-1 is in closer to the lower optimal

zone, while FRA-2 is closer to the upper usable zone. Therefore, both FRAs are suitable for concrete and mortar. However, it is worth noting that an aggregate with a granulometric curve in the optimum zone tends to improve the packing of the mixture.

In addition, it can be seen in Table 1 that FRA-2 has a high content of fines, being higher than that of FRA-1 (16.8% against 7.9%), mainly because this waste is subjected to more wear and crushing steps. In the roller mill, the friction between the waste particles and between these particles and the rollers is more intense, resulting in smaller particles than those obtained from the jaw crusher.

Table 1. Physical properties of the fine recycled aggregates

Properties	Aggregates	
	FRA-1	FRA-2
Fineness Modulus	2.17	3.03
Fines Content (< 75 µm) (%)	7.9	16.8
Specific Gravity (g/cm³)	2.48	1.94
Unit Weight (g/cm³)	1.40	1.00
Water Absorption (%)	7.2	14.2

This high content of fines (< 75 µm) of both aggregates is also directly related to the low resistance of the waste that originated them, making wear easier. However, the fines present in the aggregates help to improve the cohesion of mixtures of concrete and mortar, as, according to Haddad et al. (2016) and Silva Neto and Leite (2018), the fines fill the voids of the cementitious composite matrix.

Regarding to the shape of the generated recycled aggregate particles, it was observed that FRA-2 (Figure 4), due to its crushing process with more steps, caused more intense surface wear, presented more spherical particles, while in FRA-1 it was noticed more angular particles with an irregular surface. As FRA-1 was produced in a previous study, it was not possible to collect microscope images of this aggregate for comparison with FRA-2.

Similar behavior was observed in the studies of Matias et al. (2013). According to these authors, the rounding of particles indirectly benefits the quality of the concrete, since angular particles need more cement paste to fill the voids between them. This benefit is generally related to the fresh state (workability), mainly because particles that are more angular generate greater friction between them, thus compromising the fluidity of the cement mix.

Analyzing the fineness modulus (FM) of the samples, it was noticed that FRA-2 has a higher FM compared to FRA-1 (3.03 versus 2.17), indicating the greater presence of larger grains in FRA-2, evidenced due to its proximity to the upper usable zone curve. According to Haddad et al. (2016), the higher the FM, the smaller the specific surface area of the particles and consequently the lower the water demand of the mixture.

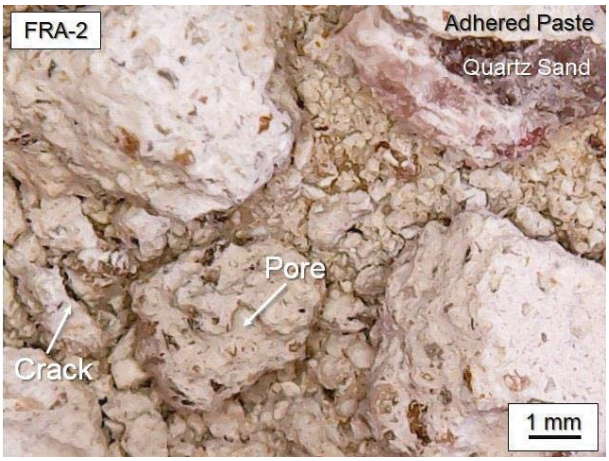

Figure 4. Microscope image of FRA-2.

The fineness modulus also influences other properties of the aggregate, such as its unit weight. As reported by Souza et al. (2016) the greater the amount of smaller particles of sand (lower FM), the better the filling of the unit weight measurement container, and the higher the value of this property. Therefore, as FRA-2 had more larger particles in its composition than in FRA-1, the lower unit weight (1.00 g/cm³) of this aggregate is justified even with its high content of fines (16.8%), showing that these fines were not enough to fill the existing voids between the grains.

Comparing the water absorption capacity of the FRAs, it was noticed that this parameter of FRA-2 is higher and almost doubled the value of FRA-1 (14.2% against 7.2%). This shows a greater porosity of FRA-2, which is confirmed by the lower values of the specific gravity (1.94 g/cm³) and unit weight (1.00 g/cm³) of this aggregate.

The porosity of these aggregates does not refer only to the porosity of the material itself, of the cement paste adhered to the natural quartz sand, resulted from the evaporation of the mixing water during the hardening of the mortar that originated the waste. This also refers to the cracks generated in the FRA particles during the comminution process. In this case, as FRA-2 suffered more impacts during comminution, it presents more cracks, corroborating for a greater number of voids in this aggregate compared to FRA-1.

Souza et al. (2016) state that the water absorption is more influenced by the nature of the aggregate than by the crusher used in the crushing process. In this research, for example, the mortar itself is already quite absorbent, for this reason these aggregates also have a high water absorption capacity.

4. Conclusion

Based on the results of laboratory tests, the following conclusions can be drawn:

- Both generated recycled aggregates have a continuous particle size distribution curve, a characteristic of important influence on the quality of the concretes.

- The fines content of the aggregates is high in both groups. However, in FRA-2 this value is higher due to the crushing process having more steps and having a greater impact on the waste.

- The shape of the FRA-1 aggregate is more angular, while the FRA-2 aggregate has a more spherical shape, the product of a greater wear during the crushing process.

- The FRA-2 aggregate has a water absorption of almost double the value of FRA-1, because in addition to the porosity of the paste adhered to natural sand; there are cracks in the recycled aggregate particles originated from the more complex crushing process.

The characteristics of the two aggregates are different although they are products of the same material. This proves that the crushing process is an important influencer on the evaluated physical characteristics.

References

Brazilian Association of Technical Standards (ABNT), 2001. NBR NM 30: Fine aggregate - Test method for water absorption. Rio de Janeiro.

Brazilian Association of Technical Standards (ABNT), 2003a. NBR NM 248: Aggregates - Sieve analysis of fine and coarse aggregates. Rio de Janeiro.

Brazilian Association of Technical Standards (ABNT), 2003b. NBR NM 46: Aggregates - Determination of material finer than 75 um sieve by washing. Rio de Janeiro.

Brazilian Association of Technical Standards (ABNT), 2006. NBR NM 45: Aggregates - Determination of the unit weight and air-void contents. Rio de Janeiro.

Brazilian Association of Technical Standards (ABNT), 2009a. NBR NM 52: Fine aggregate - Determination of the bulk specific gravity and apparent specific gravity. Rio de Janeiro.

Brazilian Association of Technical Standards (ABNT), 2009b. NBR 7211: Aggregates for concrete - Specification. Rio de Janeiro.

European Aggregates Association (UEPG), 2020. Annual Review 2018-2019. Brussels. Available in:<http://www.uepg.eu/publications/annual-reviews>. Accessed in 07 May 2020.

Haddad, L.D. et al., 2016. Analysis of influence of the fine aggregate particle size in the mechanical properties and durability of coating mortar (in Portuguese). Ciência & Engenharia (Science & Engineering Journal), 25 (1), 07-16.

Ismail, S.; Ramli, M., 2013. Engineering properties of treated recycled concrete aggregate (RCA) for structural applications. Construction and Building Materials, 44 (1), 464-476.

Leite, M.B., 2001. Evaluation of mechanical properties of concrete produced with recycled aggregates from construction and demolition waste (in Portuguese). PhD Thesis (Federal University of Rio Grande do Sul).

Lima, J.A.R., 1999. Proposal of guidelines for the production and standardization of recycled construction waste and its applications in mortar and concrete (in Portuguese). MsC Thesis (University of São Paulo).

Marinho, G. et al., 2016. Evaluation of the physical properties of recycled fine aggregates produced in jaw and impact crushers (in Portuguese). In: XVI National Meeting of Technology for the Built Environment (ENTAC). São Paulo, 4221-4232.

Matias, D. et al., 2013. Mechanical properties of concrete produced with recycled coarse aggregates – Influence of the use of superplasticizers. Construction and Building Materials, 44 (1): 101-109.

Oksri-Nelfia, L. et al., 2015. Reuse of recycled crushed concrete fines as mineral addition in cementitious materials. Materials and Structures, 49(8): 3239-3251.

Silva Neto, G.A; Leite, M.B. Study of the influence of the mortar fine recycled aggregate ratio and the mixing sequence on the behavior of new mortars. Ambiente Construído, 18 (2): 53-69.

Souza, E. et al., 2016. Evaluation of the influence of the type of crusher on the properties of coarse recycled aggregates (in Portuguese). In: XVI National Meeting of Technology for the Built Environment (ENTAC). São Paulo, 4346-4357.

Young Researchers' Forum V
Innovation in Construction Materials
22 April 2021

Influence of Sucrose on the Morphology of Calcium Hydroxide Crystals

C. Pesce and G.L. Pesce
Department of Architecture and Built Environment, Northumbria University Newcastle (UK)

A. Richardson
Department of Mechanical and Construction Engineering, Northumbria University Newcastle (UK)

ABSTRACT

While Portland cement is the most common binder used in constructions, the use of air lime in the modern construction industry can still prove to be advantageous for certain applications, if some limitations – mostly related to the carbonation reaction – are overcome. Morphology and size of calcium hydroxide (CH) have an important effect on its reaction kinetics and can be modified using organic additives. This study investigates the effects of sucrose on the morphology of calcium hydroxide. Sucrose is added to the lime, both before and after the slaking. Scanning electron microscopy and X-ray diffraction were used to investigate the crystals size and morphology in modified and control samples, while microchemical analyses were carried out to investigate the composition of pore solutions. Results suggest that sucrose, especially if added before the slaking process, affects the characteristics of CH crystals (habit and size) as well as the chemistry of the pore solution, with possible implications on the reactivity and properties of sucrose-modified lime putty and, in turn, of lime-based construction materials.

1. INTRODUCTION

The use of lime (i.e. calcium hydroxide, CH hereafter) in construction was dominant in the past centuries but is currently limited to small-scale applications due to its replacement by the stronger and faster-setting Portland cement (Cultrone, Sebastián and Huertas, 2005; Carran *et al.*, 2012). However, use of lime can still prove to be advantageous in some applications thanks to its high breathability and workability (Cultrone, Sebastián and Huertas, 2005). Among the reasons for the disuse of lime is the slow hardening process and the high sensitivity to environmental conditions, both related to the carbonation reaction (Cizer *et al.*, 2008). Among the various methods used to increase the carbonation rate in lime-based materials (Rodriguez-Navarro *et al.*, 2019), in recent years the use of organic additives has seen the favour of various researchers. In fact, according to various studies, the numerous types of organic additions (including oils, plant extracts, sticky rice) found in formulations of historic lime mortars are responsible for the improved properties and extraordinary durability of these materials, by affecting their pore structure, modifying the crystallisation path of both CH and $CaCO_3$ and as overall result accelerating their setting process (El-Turki *et al.*, 2005; Yang, Fuwei, Bingjian Zhang, 2010; Ventolà *et al.*, 2011; Rodriguez-Navarro *et al.*, 2017). Among the traditionally used additives, sugar is documented in historic mortars of different countries and cultures (Cowper, 1927; Ravi, Rajesh and Thirumalini, 2018; Thirumalini, Ravi and Rajesh, 2018). Despite the extensive use and the recognised superior quality of these mortars, few insights are provided on the mechanism through which sucrose interacts with CH. Most of the related knowledge comes from cement-related research, as sucrose has been used since almost a century as set retarder for its ability of poisoning CSH nucleation (Cheung *et al.*, 2011). So far, only few studies have been focused on pure CH systems and the role of sucrose on the nucleation and crystal growth of CH has not been completely elucidated yet (Young, Berger and Lawrence, 1973; Rodriguez-Navarro *et al.*, 2017; Martínez-Ramírez *et al.*, 2019). In this study, we aim at providing some insight on the effect of sucrose on the size and shape of CH crystals as they are linked to the rheological properties and reactivity of a lime putty (Elert *et al.*, 2013).

2. Materials and Methods

A total of 3 lime putties were prepared and analysed in this research: a control putty (referred to as 'C' hereafter), prepared by slaking CaO in water at 1:3 mass ratio; a sucrose-modified putty (S-1), prepared by slaking CaO in a 5% aqueous solution of sucrose at 1:3 mass ratio; and a sucrose-modified putty (S-2), prepared by adding immediately after the slaking process a quota of sucrose (5% w/v of water as for the previous batch) to a putty obtained like the control. 'Calbux Granular 15' CaO (CL90 type (British Standards Institution, 2015)) with nominal particle size <15

mm was supplied by Tarmac Buxton Lime (UK). Microstructural and mineralogical characteristics of this lime are reported in (Pesce and Pesce, 2019). Sucrose (≥99.0%) from Sigma-Aldrich and ethanol >99.8% from Fisher Scientific were used in the experiments. All putties and the related supernatant solutions were characterised with various analytical techniques when fresh and after 6 months of ageing (i.e. storage under water). Prior to each analysis a sample of each putty was collected from the core of the batch and quenched in ethanol. For microstructural analysis a quote of each quenched putty was transferred onto a metal stab, vacuum-dried for 1 hour at 50°C, Pt-coated, and observed with a Tescan Mira3 Scanning Electron Microscope (SEM) in high-vacuum mode. Image processing was performed with software ImageJ (v1.52i). For mineralogical analysis samples were prepared as described in (Rodriguez-Navarro, Hansen and Ginell, 1998) and analysed with a Rigaku SmartLab X-ray diffractometer (XRD), with Cu-Kα radiation, parallel beam geometry, 10°-90° 2θ scan range, 0.5° scan step, at 50kV and 40mA. Estimation of CH platelets abundance was calculated as in (Rodriguez-Navarro, Hansen and Ginell, 1998). The mean crystallite size was estimated from the XRD data using the Halder-Wagner method (Halder and Wagner, 1966) implemented in the Rigaku SmartLab Studio II software package. The particle size distribution (PSD) of the putties was measured via laser diffraction using a Mastersizer 3000 (Malvern Panalytical). Agglomeration was limited through sonication and by using ethanol as dispersant. The total Ca concentration in the supernatant solutions was estimated with a Perkin Elmer Optima 8000 Inductively Coupled Plasma - Optical Emission Spectrometer (ICP-OES). For this analysis a sample of each solution was filtered through a 0.1 µm PTFE syringe filter and diluted (x100 or x1000) in a 2% H2NO3 solution.

3. Results and discussion

Selected SEM images of the putties are reported in Figure 1. In the fresh control putty (Figure 1a), CH crystals display various habits, including short rod-like prism, hexagonal platelet and bipyramidal up to 1 µm size, embedded in a matrix of nanogranular crystals. In the aged control the nanogranular crystals seem more abundant. These characteristics are typical of CH crystals formed upon lime slaking in water and the increase of nanogranular crystals with ageing has been previously observed in aged lime putty (Rodriguez-Navarro, Hansen and Ginell, 1998; Mascolo *et al.*, 2010; Navrátilová *et al.*, 2017). In S-1 (Figure 1b), the observed microstructure is composed of agglomerated nanogranular crystals (max 200 nm) without a discernible geometry, both in the fresh and aged putty. Such irregular shape has been also reported by Martinez-Ramirez *et al.* in CH crystals precipitated in sucrose solution and is attributed to the ability of sucrose of complexing Ca^{2+} ions (Martínez-Ramírez *et al.*, 2019). In S-2 (Figure 2c) crystals display a rod-like habit also found in the control while very few nanogranular crystals are visible. In the aged S-2 more nanogranular crystals as well as stepping of basal faces and lamellar structures in µm-sized crystals are visible.

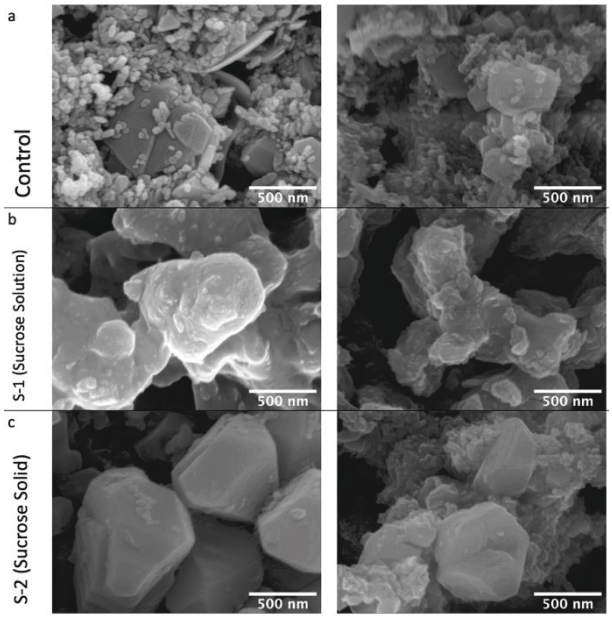

Figure 1. SEM images of the putties: (a) control; (b) S-1 putty slaked in sucrose solution; (c) S-2 putty with addition of solid sucrose. The left and right column show fresh and aged samples, respectively.

The quantitative phase analysis of the putties showed that CH was expectedly the main phase in all putties. Some traces (<5%) of calcite were detected in fresh S-1, likely formed upon carbonation in air during sample preparation. The CH platelets abundance (A001) and mean crystallite size of the putties are shown in Table 1. A001 increases with ageing in all samples, however values of S-2 are significantly higher than the control. The observed increase of A001 with ageing is supported by the literature that describes the morphological evolution from prism to platelet habit of CH crystals upon ageing (Rodriguez-Navarro, Hansen and Ginell, 1998; Cazalla *et al.*, 2000; Mascolo *et al.*, 2010). The results also show that the crystallite size of both sucrose-modified putties are lower than the control, especially sample S-1. This suggests that crystal growth was strongly inhibited, probably due to the same mechanism by which sucrose acts as set retarder in cement hydration, i.e. nuclei poisoning by adsorption on CSH nuclei (Cheung *et al.*, 2011). As A001, also the mean crystallite size increases with ageing. To this regard, our results do not support previous work where reduced crystallite size in aged putty has been reported (Rodriguez-Navarro, Hansen and Ginell, 1998; Cazalla *et al.*, 2000; Atzeni *et al.*, 2004; Mascolo *et al.*, 2010; Ruiz-Agudo and Rodriguez-Navarro, 2010), whereas are in agreement with the Ostwald's ripening

mechanism, which models the increase of big particles overtime at the expense of the smaller (Ostwald, 1897).

Table 1. Calculations from XRD data of mineralogical characteristics of the putties.

Parameter	Fresh			Aged		
	C	S-1	S-2	C	S-1	S-2
A_{001}	0.70	0.74	0.96	0.88	0.83	1.31
Crystallite Size (nm)	35	13	29	36	14	32

The total Ca concentration in the supernatant solutions are reported in Table 2. Results show that in the S-1 and S-2 samples the concentration is 3 to 5 times higher than the control, both in the fresh and aged samples. This suggests that sucrose has increased Ca solubility by forming stable complexes, as observed in previous works (Pannetier, Khoukh and François, 2001; Martínez-Ramírez *et al.*, 2019). The ability of sucrose of complexing Ca ions and keeping them in solution seems comparable between S-1 and S-2. However, because of the microstructural and mineralogical differences observed between S-1 and S-2 with the putty characterisation techniques, we should assume that complex formation must not be the only factor determining the characteristics of CH crystals. Arguably, the thermal treatment to which sucrose is subject when it is added before slaking (i.e. S-1 sample) could also play a role. In fact, the high temperature reached during slaking (>200°C) should favour the oxidation and hydrolysis of sucrose with consequent formation of reducing sugars as degradation products, which are known to affect CH crystal nucleation and growth, and their presence in solution might account for the observed differences between S-1 and S-2 (Lu, Thomas and Schmidt, 2017; Rodriguez-Navarro *et al.*, 2017).

	Fresh			Aged		
	C	S-1	S-2	C	S-1	S-2
[Ca] (mg/L)	938	5090	2845	797	3727	4785

4. Conclusions

The slaking of lime in sucrose solution produced visible changes in the morphology of CH crystals, which exhibit a peculiar irregular shape with no discernible geometry and a significantly smaller crystallite size than in plain lime putties. Conversely, the CH crystals in a putty slaked in water with late addition of solid sucrose displayed habits commonly found in lime putties and their crystallite size is closer to that found in pure lime putties. While the ability of sucrose of complexing Ca ions and affecting $Ca(OH)_2$ nucleation and crystal growth is well known, the effects observed in our study cannot be attributed solely to complex formation. In fact, our results show that the solutions in equilibrium with the sucrose-modified putties have similar Ca concentrations with each other – both are much higher than the theoretical saturation value. To explain such discrepancy, we speculate that the degradation products (i.e. reducing sugars) formed upon thermal treatment when sucrose is introduced before slaking plays a crucial role in determining the mineralogical and microstructural characteristics of portlandite crystals. Further modelling or molecular analytical techniques that provide a complete speciation of the pore solutions should contribute to verify our hypothesis.

Acknowledgements

We kindly acknowledge Tarmac Buxton Lime for providing the quicklime used in our experiments.

References

Atzeni, C., Farci, A., Floris, D., Meloni, P., 2004. Effect of aging on rheological properties of lime putty. Journal of the American Ceramic Society, 87(9):1764–1766.

British Standards Institution, 2015. Building lime. Definitions, specifications and conformity criteria. BS EN 459-1:2015.

Carran, D., Hughes, J., Leslie, A., Kennedy, C., 2012. A short history of the use of lime as a building material beyond Europe and North America. International Journal of Architectural Heritage, 6(2):117–146.

Cazalla, O., Rodriguez-Navarro, C., Sebastian, E., Cultrone, G., 2000. Effects on Traditional Lime Mortar Carbonation. Journal of the American Ceramic Society, 83(5):1070–1076.

Cheung, J., Jeknavorian, A., Roberts, L., Silva, D., 2011. Impact of admixtures on the hydration kinetics of Portland cement. Cement and Concrete Research, 41(12):1289–1309.

Cizer, O., Van Balen, K., Van Gemert, D., 2008. Blended lime-cement mortars for conservation purposes: Microstructure and strength development. Structural Analysis of Historic Construction: Preserving Safety and Significance - Proceedings of the 6th International Conference on Structural Analysis of Historic Construction, SAHC08:965–972.

Cowper, A. D., 1927. Lime and Lime Mortars. London: Building Research Station.

Cultrone, G., Sebastián, E., Huertas, M. O., 2005. Forced and natural carbonation of lime-based mortars with and without additives: Mineralogical and textural changes. Cement and Concrete Research, 35(12):2278–2289.

El-Turki, A., Ball, R., Wang, C.F, Allen, G.C., 2005. A study of novel lime based mortars consisting of lime, oyster shell lime, clay, sugar, sand and rice using Focused Ion Beam microscopy, Raman spectroscopy and mechanical testing. 10th Euroseminar on Microscopy Applied to Building Materials. Paisley, UK.

Elert, K., Rodriguez-Navarro, C., Pardo, E. S. 2013. Studies in Conservation Lime Mortars for the Conservation of Historic Buildings, 3630.
Halder, N. C. and Wagner, C. N. J. 1966. Separation of particle size and lattice strain in integral breadth measurements. Acta Crystallographica. International Union of Crystallography 20(2):312–313.
Lu, Y., Thomas, L., Schmidt, S., 2017. Differences in the thermal behavior of beet and cane sucrose sources. Journal of Food Engineering, 201:57–70.
Martínez-Ramírez, S., Higueruela, L.R., Cascales, I., Martin-Garrido, M., Blanco-Varela, M.T., 2019. New approach to nanolime synthesis at ambient temperature. SN Applied Sciences, 1(1):1–8
Mascolo, G., Mascolo, M.C., Vitale, A., Marino., O., 2010. Microstructure evolution of lime putty upon aging. Journal of Crystal Growth, 312(16–17):2363–2368.
Navrátilová, E., Tihlarikova, E., Nedela, V., Rovnanikova, P., Pavlik, J., 2017. Effect of the preparation of lime putties on their properties. Scientific Reports, 7(1):1–9.
Ostwald, W., 1897. Studien über die Bildung und Umwandlung fester Körper. Zeitschrift für Physikalische Chemie, 22:289–330.
Pannetier, N., Khoukh, A., François, J., 2001. Physico-chemical study of sucrose and calcium ions interactions in alkaline aqueous solutions', Macromolecular Symposia, 166:203–208.
Pesce, C., Pesce, G., 2019. Effects of Steam Slaking on the Characteristics of Portlandite Crystals. Proceedings of the 39th Cement and Concrete Science Conference, 58–61.
Ravi, R., Rajesh, M. Thirumalini, S., 2018. Mechanical and physical properties of natural additive dispersed lime. Journal of Building Engineering. 15(July 2017):70–77.
Rodriguez-Navarro, C., Ruiz-Agudo, E., Burgos-Cara, A., Elert, K., Hansen, E.F. 2017. Crystallization and Colloidal Stabilization of $Ca(OH)_2$ in the Presence of Nopal Juice (Opuntia ficus indica): Implications in Architectural Heritage Conservation. Langmuir, 33(41):10936–10950.
Rodriguez-Navarro, C., Cizer., O, Kudlacz, K., Ibanez-Velasco, A., Ruiz-Agudo, C., Elert, K., Burgos-Cara, A., Ruiz-Agudo, E., 2019. The multiple roles of carbonic anhydrase in calcium carbonate mineralization. CrystEngComm, 21(48):7407–7423.
Rodriguez-Navarro, C., Hansen, E. Ginell, W. S., 1998. Calcium Hydroxide Crystal Evolution upon Aging of Lime Putty. Journal of American Ceramic Society, 81(11):3032–3034.
Ruiz-Agudo, E., Rodriguez-Navarro, C., 2010. Microstructure and rheology of lime putty. Langmuir, 26(6):3868–3877.
Thirumalini, S., Ravi, R. Rajesh, M., 2018. Experimental investigation on physical and mechanical properties of lime mortar: Effect of organic addition. Journal of Cultural Heritage, 31:97–104.
Ventolà, L., Vendrell, M., Giraldez, P., Merino, L., 2011. Traditional organic additives improve lime mortars: New old materials for restoration and building natural stone fabrics. Construction and Building Materials, 25(8):3313–3318.
Yang, F., Bingjian Z., Qinglin, M., 2010. Study of Sticky Rice - Lime Mortar Technology. Accounts of chemical research, 43(6):936-944.
Young, J. F., Berger, R. L., Lawrence, F. V., 1973. Studies on the hydration of tricalcium silicate pastes III. Influence of admixtures on hydration and strength development. Cement and Concrete Research, 3(6):689–700.

Young Researchers' Forum V

INNOVATION IN CONSTRUCTION MATERIAL

GLASGOW CALEDONIAN UNIVERSITY

22nd April 2021